FABRICATION AND PROPERTIES OF JOSEPHSON JUNCTIONS WITH A SEMICONDUCTOR BARRIER

A THESIS

SUBMITTED TO THE BOARD OF STUDIES IN ELECTRONICS

AND THE GRADUATE SCHOOL

OF THE CHINESE UNIVERSITY OF HONG KONG

IN PARTIAL FULFILLMENT OF THE REQUIREMENTS

FOR THE DEGREE OF

MASTER OF PHILOSOPHY

By Mr. Hing-hung Anthony CHAN

with supervisor Dr. Chu-cheng CHANG

May 1977

ABSTRACT

We have investigated d.c. and a.c. properties of Josephson junctions with semiconducting barrier.

For the commonly used semiconductor barrier thickness range, Pb-GeTe-Pb junctions exhibit normal tunneling or superconductive tunneling according to whether the GeTe barrier is amorphous or crystalline.

Laser pulse irradiation is employed for GeTe recrystallisation to reduce junction area and to minimize diffusion.

Small junction is obtained which has high critical current density and high $I_J R_{NN}$ figure of merit.

Large constant voltage current steps are obtained under μ wave radiation, showing strong response to the e.m. wave.

A C K N O W L E D G E M E N T S

I would like to express my sincerely gratitude to my supervisor Dr. C. C. Chang, who has guided me in both academic and nonacademic mathers. I appreciate very much his keen research altitude even when budget has not been promising locally, and I feel proud of having developed my research interests through the co-operative work with him.

Thanks are also due to Mr. J. S. Dahele for advice and use of microwave instruments, and to Dr. P. W. Chan and Dr. Y. W. Chan for the handling of laser facilities.

In preparing the present manuscript, a lot of technical assistance were received from my friends S. Y. Luk, L. K. Sin, W. H. So and Y. H. Lau as well as my colleagues S. K. Kwok and C. S. Poon. Their patience to so much clerical work is to be acknowledged.

H. H. A. Chan

1977

CONTENTS

I. Introduction

There has been active research interest in the applications of Josephson junctions. While the S-I-S (superconductor -- insulator -- superconductor) oxide junction characteristics are difficult to control in the fabrication procedure, the S-S'-S (superconductor -- semiconductor -- superconductor) junctions offer various advantages over the oxide junctions.

The lower potential barrier allows the use of thicker barrier ($\gtrsim$ 10 nm) than the very thin insulating oxide barrier ($\sim$ 1 nm), and hence allows the characteristics more reproducible and controllable.

For superconducting memory unit and logic circuit switching elements, self-resonances limit the usable switching time of S-I-S junctions. S-S'-S junctions do not have these internal resonances because of their higher damping in the barrier and hence lower Q-factor.

S-S'-S junctions also provide more effective damping of Plasma oscillations and will therefore have shorter switching time [1].

The high frequency applications include detection, monochromatic generation, mixing and parametric amplification for practically any frequency up to infra-red. Use in the microwave frequency range is convenienced with MIC (microwave integrated circuit) technology. With thicker barrier, the lower capacitance S-S'-S junctions are expected to give improved high frequency coupling [2].

However, both the d.c. and a.c. properties of S-S'-S junctions have not been well established with the previous experimental studies. There were also technological difficulties with the previous investigations [2].

GeTe film on the conventional substrates can be completely recrystallized by thermal means and the crystallized GeTe has high conductivity [6]. We have also obtained metal induced recrystallisation for GeTe on Pb film. GeTe is also a superconductor with lower T_c [7]. Josephson tunneling data for S-GeTe-S junctions would allow quantitative comparison of the proximity effect and the T_c value for GeTe, but work on such junctions has not been reported by other workers. In an earlier communication, we had mentioned about quasi-particle tunneling in S-GeTe-S junctions [8]. Here, we report on our investigations with these junctions.

For S-S'-S Josephson junctions, although the theoretical advantage of using the semiconducting barrier in a.c. Josephson is well known, the microwave properties of such sandwich-type junctions have not been reported. It is also one of our objectives to investigate the microwave response of our S-GeTe-S junctions using resonator coupling with MIC.

For Ge barrier, the previous results were seemingly different. Quasi-particle tunneling [3], Josephson tunneling with anormously high current density [4], and Josephson tunneling with characteristics similar to oxide junctions [5] were reported. We

have investigated Ge barrier, taking into account the thickness, the doping level, and the crystallisation of the Germanium, as well as the characteristics of imperfect junctions. We found that Ge is not suitable as a semiconducting barrier for Josephson tunneling. Technological limitations include the degree of crystallisation and the solid solubility of dopant to lower the resistivity and the barrier height. These will be discussed elsewhere (Appendix IV).

II. BACKGROUND

Josephson junctions can have the form of a tunneling junction or many other weak-link junctions, but we shall concentrate our investigations on tunneling junctions. The tunneling barrier can be an insulator, semiconductor or normal metal, and such sandwiches are commonly denoted as S-I-S, S-S'-S and S-N-S respectively.

In the macroscopic quantum mechanical approach, Josephson tunneling is regarded as coherent transition between two quantum levels of a system described by a macrowave. The situation is analogous to that of a laser.

In the phenomenological approach, a Josephson junction consists of two superconductors weakly coupled together and the relations are semiclassical but verified by experiments.

We shall mainly use the phenomenological relations, bearing in mind that they have support from the macroscopic quantum mechanical approach, which in turn has been justified. A review of these formal derivations has been given by Rogovin and Scully [9].

2.1 Background dc Josephson effect relations

The total current density for a Josephson junction consists of the following three terms:

$$j = j_J \sin \phi + \left[\sigma_o(V) + \sigma_1(V) \right] V$$

pair term; quaiparticle term; interference term

where $\sigma_1(V)$, which arises from quasiparticle-pair interference effect [10, 11], is negative.

The present models have included only the first two terms, which will be discussed below. It will be more convenient to discuss in terms of current.

Superconductive tunneling cooper pairs through a thin barrier or weak link gives rise to zero voltage pair current i_p [10]

$$I = i_p = I_J \sin \phi$$

where I_J : critical current

ϕ : macroscopic phase difference across the barrier

for current $I < I_J$

With finite voltage aross the barrier, there is also a quasi-particle tunneling current i_q

$$I = i_p + i_q$$

The normal tunneling can be represented by the following approximate relation [12]

$$\frac{i_q}{i_{qo}} = \left(\frac{\langle V\rangle}{\langle V\rangle_g}\right)^n$$

where $\langle V\rangle$ is the d.c. voltage

$\langle V\rangle_g = \frac{2\Delta(T)}{e}$ is the gap voltage

$2\Delta(T)$ is the energy gap of the superconducting electrodes

i_{qo} is a constant for a given characteristic

The switching at current bias between zero and non-zero voltage can be hysteretic or non-hysteretic, characterised by the hysteresis parameter

$$a_m \equiv \frac{I_R}{I_J}$$

where I_R is the reverse switching current.

This is related to Stewart's damping factor, which is defined by [12]

$$k_n \equiv \left(\frac{i_{qo}}{I_J}\right)^{2/n} \frac{\bar{\Phi}_o I_J}{2\pi C \langle V\rangle_g^2}$$

where C ; Junction capacitance

$\bar{\Phi}_o \equiv \frac{h}{2e}$ is the flux quantum

2e: charge of a Cooper pair

For n= 1, this is related to McCumber's parameter [13] by

$$\beta_c = \frac{1}{k_1}$$

Hysteresis, i.e. $a_m < 1$, can be caused by junction capacitance although self-heating effects [14] can also be the cause, with $\beta(a_m)$ curve differing only slightly from $\beta_c(a_m)$ for n = 1.

McDonald et al. [15] introduced a similar damping factor

$$\frac{\tau_g}{\tau}$$

where $\tau = R_{NN}C$

R_{NN}: Normal tunneling resistance

and τ_g is given by

$$\frac{h}{\tau_g} \equiv 2e\Delta$$

Starting from the Werthamer tunneling theory [16] for small junction at T = 0 K, they calculated the I - $\langle V \rangle$ characteristics numerically. With increasing damping, hysteresis decreases ($a_m \longrightarrow 1$) with more i_p current component below $\langle V \rangle_g$, and the Riedel peak [17], i.e. enhancement of i_p near 2Δ, becomes more pronounced.

With a model to include the superconducting electrodes, they showed that both odd and even subharmonic energy gap structures with cusplike and steplike appearances respectively are exhibited due to self-detection of a.c. Josephson effect.

Another aspect of tunneling measurement is that $\frac{dI}{dV}$ for normal tunneling gives a measure of the density of states; $\frac{d^2I}{dV^2}$ measurements are used to investigate fine structures.

Ambegokar and Baratoff [18] showed from microscopic theory the theoretical value of $I_J(T)$ for S-I-S junction with identical weak-

coupling superconductors

$$I_J(T) = \frac{\pi \Delta(T)}{2 e R_{NN}} \tanh \frac{\Delta(T)}{2kT}$$

Fulton and McCumber [19] showed a reduction factor is needed with strong-coupling superconductors.

$I_J(H)$ diffraction pattern

For rectangular junction with H applied in the plane of the barrier and normal to one of the rectangular edge, $I_J(H)$ possesses the Fraunhofer interference pattern [20].

$$I_J(H) = I_{JM} \left| \frac{\sin \pi x}{\pi x} \right|$$

where I_{JM} is the maximum $I_J(H)$ value

$$x \equiv \frac{\Phi}{\Phi_o}$$

Φ is the magnetic flux enclosed in the junction

This holds only for small junction, for which $\lambda_J < W$

$$\lambda_J \equiv \left(\frac{\hbar}{2 e \mu_o J_J d} \right)^{1/2}$$: Josephson penetration depth

W : junction width

For higher I_J junctions, the self-field [21, 22] due to the Josephson current itself causes the diffraction pattern to be tilted.

For wide junction, which has $\lambda_J > W$, the transverse variation of ϕ becomes significant so that the overall $I_J(H)$ pattern has a number of the first periods averaged out to give a smoothed triangular shape there.

Imperfect junctions have microshort(s). With only a single short or one dominating short, I_J is practically insensitive to H due to too small a magnetic flux enclosed by the very tiny area of the short.

With multiple microshorts, the imperfect junction are effectively Josephson junctions in parallel and the $I_J(H)$ exhibits the Mercereau effect [23], also known as SLUG [24] behaviour.

2.2 Background a.c. Josephson effect relations

At non-zero voltage, the junction radiates at a frequency of [10]

$$\nu = \frac{2 e V}{h}$$

The most convenient frequency range at the present technology is the microwave frequency range.

Under an externally applied microwave radiation of frequency ν_o, the junction's radiation can become phase-locked to ν_o or its harmonics

$$\nu = n \nu_o$$

so that the static I-V characteristic has microwave induced steps [25] at

$$V_n = n \frac{h \nu_o}{2 e}$$

The current step heights depend on I_J.

It can also exhibit Fiske mode [26] of self induced current steps at internal cavity resonance when

$$L = n \frac{\lambda}{2}$$

where L : length of barrier

$$\lambda = \lambda_o \left[\frac{d}{\epsilon_r (d + 2\lambda_L)} \right]^{1/2}$$ [27]

$\lambda_o = \frac{c}{\nu}$ is the wavelength in free space

ϵ_r : relative permitivity of barrier

d : thickness of barrier

λ_L : London penetration depth

Coupling of microwave radiation to the junction can be improved by means of an external cavity or by using the resoncance frequency of the internal cavity itself.

III. REVIEW AND INTERPRETATION OF PREVIOUS WORK

3.1 Oxide barrier junctions : Present state of art

The work up to 1971 had been reviewed in Solymer's book [28].

In short, the experimental results of oxide junctions agree with the theoretical relations in the preceding section. In this section, we shall discuss other additional aspects and we shall concentrate on Pb-based tunnel junctions, which can be measured at the convenient temperature of 4.2 K with liquid Helium. Nb, although having even higher T_c and 2Δ, suffers from complex oxode formation of several forms and is difficult to give uniform barrier and more ideal I-V characteristic.

The oxide thickness for S-I-S Josephson junctions is only ~2 nm. Being only ~10 atomic layers thick, the barrier can deteriorate unless the junction is stored at 77 K.

Pb-PbO_x-Pb junctions are especially unstable above cryogenic temperatures or against thermal cycles. This could be due to the instability of the oxide and the diffusion of oxygen away from the barrier. Pb also has very high atomic diffussivity and forms hillocks [29] by recrystallization mechanism even at room temperature, resulting in shorted junctions.

Today, various fabrication techniques have been tried out in various laboratories to aim at more thermally stable, rugged and reproducible junctions with good yield for possible widespread use.

They are not always reproducible among different laboratories and the mechanism has not been fully understood.

At NBS, they use relatively thin Pb film of $\lesssim 200$ nm thickness and oxidise the Pb in O_2 atmosphere at 60°C [30]. Apparently, the mass transfer for hillock formation is less energetically favoured with this Pb film thickness. If exposed to air for oxidation, adsorption of N_2 on Pb surface and grain boundaries will inhibit oxidation and cause shorts.

With dilute Pb-In alloy film as base electrode, In concentrates on the surface and can suppress hillock formation [29]. In also forms stable oxide In_2O_3. Lahiri added Au to the alloy and further improves the stability of the junctions [31]. Au seggregates out at grain boundaries to inhibit hillock formation.

Due to the high potential barrier of insulating oxide, the maximum Josephson current density, J_J, depends strongly on barrier thickness d; for Pb-PbO_x-Pb junctions [32]

$$J_J(d) \fallingdotseq 15 \times 10^6 \exp\left(-\frac{d}{0.15}\right) \text{ A mm}^{-2}$$

where d is in nm.

The difficulty to fabricate junctions with reproducible characteristic is anticipated.

In_2O_3 has a higher conductance. Niemeyer and Kose [33, 34] obtained very high J_J for small junction using Pb–In alloy as base electrode. Oxide thickness was controlled by varying the oxidation temperature. This in turn varies J_J and hence the damping factor $\frac{\tau_c}{\tau}$.

Their results agree with the calculations of McDonald et al.[35] .

The investigations of a.c. properties of Josephson junctions had been hindered by coupling problems and were mostly limited to point-contact or other weak-link junctions.

The application of MIC technology to thin-film Josephson junctions [35] has speeded up these broad areas of experimental work for tunnel junctions at microwave frequencies.

The high frequency coupling to tunnel junctions can also be improved with either internal or external resonator coupling.

The high frequency properties of thin-film tunnel junctions and junction arrays are being extensively studied. Frequency mixing, coherent generation and emission, and $\frac{2e}{h}$ standard applications are of current interest.

It was realized that the MIC technology can join with the internal resonator coupling technique [36]. However, the geometrical restrictions imposed on the self-resonant junctions for the desired frequency range may sometimes be inconvenient. The internal resonance frequency is also temperature dependent.

To overcome these problems, the use of the more controllable external microstrip resonator in MIC is being developed [37] . In such cases, small junctions are used so that the resonance frequency of each junction lies far above the working frequency range.

In contrast to S-N-S junctions, oxide junctions have higher resistances for practical junction areas. This provides a more convenient output voltage for small current bias, and makes the oxide junctions suitable for $\frac{2e}{h}$ voltage standard . Microwave induced steps for Pb-PbO_x-Pb junctions at voltages approaching 10 mV have been achieved to maintain the voltage standard at NBS [37,38] .

The current step voltage for a single junction is limited by the $I_J R_{NN}$ limit, which can well be approached in oxide junctions. A compromise between noise, which inreases with R_{NN}, and Joule heating $\frac{V^2}{R_{NN}}$, has to be made.

Another trend of current interest are the Josephson logic and memory devices, ultilizing the hysteretic characteristic. The work up to 1976 has been reviewed by Zapple [39].

Here tunnel junction is preferred to weak-link junctions because of its high resistance below $\langle V \rangle_g$. Various logic devices and memory cells ultilizing oxide junctions were achieved. They have the much faster operational time of $\sim 10^2$ ps than any other type of computer elements at present.

The switching time of an oxide junction depends on RC and is therefore limited by junction capacitance. The concept of Quantum interference has been applied to the Josephson memory cell [40].

In the interferometer version, faster speed will be possible by reducing the size of the junctions.

Single flux-quantum memory cells have been achieved [41, 42]. Theory also shows that the Quantum interference Josephson logic devices are capable of more flexible operations.

Today, the technology is being explored for the potential large scale ultra-fast computing system.

Most of these work ultilize oxide tunnel junctions. Our present understanding and technology of the semiconductor barrier counterpart are lagging behind.

3.2 Semiconductor-barrier junctions — Review and systematic interpretation of previous results

In this section, we shall first exhaust the common features of S-S'-S junctions including a short review of spurious currents and the anomalous features. We shall then review the previous results with a systematic model for interpretation.

3.2.1 Review of I-V characteristics

The following features of S-S'-S junctions have been reported:

1. Superconductive cooper pair tunneling
   The d.c. Josephson effect may not be observable unless the tunneling probability is sufficiently large to be unaffected by thermal fluctuations.
2. Quasiparticle tunneling across the barrier
   The current has a jump at V_g given by [43]

$$I_{jump}R = \frac{\pi}{4}V_g \qquad \text{for } T = 0 \text{ K.}$$

   Quasiparticle tunneling is otherwise independent of temperature except for

$$V_g(T) \equiv \frac{2\Delta(T)}{e}$$

   It is commonly observed with a wide class of barriers and is most clearly observed with thin barriers of high barrier height and resistivity so that other spurious conduction processes have less contributions. Typically, $d \sim 10$ nm.

Most deposited S' materials do not form continuous layers and oxidation of pinholes [64] is required. However,

Carbon is reported to be able to form a continuous film for $d \gtrsim 9$ nm and can also fill pinholes of other barriers [45].

Photosensitive quasiparticle tunneling has only been reported for CdS [64], CdSe [46], PbS [65], Te and Se [47] barriers. It is observable only for those photoconductors which exhibit conductivity storage [48, 65] characterised by an exceedingly long photoexcited carrier lifetime [49].

3. Subharmonic structures at $\frac{V_g}{n}$ for both odd and even n (see also Appendix I).

4. Longitudinal optical phonon structures of the barrier due to interaction of tunneling electrons with LO phonons. The structures are more pronounced in S-I-S'-S junctions. They have been observed for barrier materials of Ge, PbS, ZnS, CdS [65], CdS_xSe_{1-x} with $x = 0 \rightarrow 1$ [52] and Te [75]. However, tunneling electron-magnon interactions have not yet been reported.

5. Current due to thermally excited carriers, which increases with increasing temperature and decreasing barrier height, ϕ_b.

6. Schottky tunneling [50] current which increases rapidly at $eV \gtrsim \phi_b$. It has been reported for C barrier junction with the low ϕ_b of 25 meV [45].

7. Excess current peak near sum of half-energy gaps voltage, $\frac{\Delta_1 + \Delta_2}{e}$, of electrodes.

8. Zero bias anomaly (ZBA).

9. Two step tunneling via superconducting particles embedded in the barrier. This is especially prominent in nonstoichiometrically deposited barrier such as CdS [51,65] , and the effect has been convencingly illustrated using Al-CdS-Cd-CdS-Al junctions [51].

Spurious currents and anomalies

5 and 6, together with the following 2 tunneling relations for N-S'-N junctions retangular barrier, are used to partly account for spurious currents for $V < V_g$:

The low voltage conductance decreases exponentially as $\phi_b^{1/2}\, d$ [50]

$$G_q \propto \exp\left[-2\frac{(2m^*)^{1/2}}{\hbar}\phi_b^{1/2}\, d\right]$$

where m*: effective mass of the tunnel electron.

The tunnel current depends also on V [53]

$$i_q \propto \sinh\left[\frac{1}{2}x\frac{(2m^*)^{1/2}}{\hbar}x\frac{eVd}{\phi_b^{1/2}}\right]$$

so that the non-linearity of the I-V curve is evident for $\phi_b < eV_g$. There have been good agreement for the low ϕ_b materials CdS [64] and CdSe [54] when the electrodes are superconducting.

These relations are primarily N-S'-N relations with rectangular barriers and should only have restricted validity here.

The last three features are observed for some junctions only. The $\frac{\Delta_1 + \Delta_2}{e}$ current peak has been reported for Ge, InSb [63], CdSe [46] and oxide junctions with Nb electrode, and is therefore not related to the barrier material. It is most characteristic with Nb electrode but is also found in Pb-Zn-Oxide-Pb junctions [55]. The latter was explained by induced gaplessness on the electrode surface.

Investigations of the oxide junctions suggest that this excess current is caused by tunneling through intermediate impurity states that are due to adsorbed O_2 [56].

We believe this same mechanism is applicable to semiconductor-barrier junctions because O_2 can always be adsorbed on the amorphous semiconductor surface especially during the oxidation process required to oxidize pinholes. For Ge, this is consistent with the fact that evaporated Ge has been shown to possess a porous structure and the uptake of O_2 is significant even at an ordinary high vacuum pressure of 10^{-7} mm Hg [57].

ZBA has many possible forms and causes. It can be caused by paramagnetic impurities of the barrier [58]. It can also be due to two step tunneling process for non-stoichiometric barrier containing superconducting particles. The latter has been observed with CdS barrier [51].

3.2.2 Review and systematic interpretation of previous results

Here, we present an unprecedentedly simple interpretation of previous results. We aim at a simple and yet physical and unambiguous presentation.

Semiconductor-barrier Josephson junctions have not been sufficiently investigated. Josephson tunneling through the S' barrier has been achieved for only a few S' materials. These are Ge, InSb, CdS, Pb Te, Te and Si. The reported investigations by different groups are not unanimous. The theory has not been well presented and different models are proposed.

We suggest that all sandwich type Josephson junctions can be well interpreted by classifying the weak coupling layer into:

(1) Tunneling barrier region of potential barrier

$$\phi_B \equiv \phi_B(\vec{r})$$

We shall also denote this region by ϕ_B unless the distinction is not clear.

(2) Normal region, N.

The actual weak coupling region behaves as one of these or their combinations.

Examples are:

(a) S-ϕ_B-S (pure tunneling junction)
(b) S-N-S (pure proximity junction)
(c) S-ϕ_B-N-S
(d) S-ϕ_B-N-ϕ_B-S
(e) S-N-ϕ_B-N-S.

We use the simple energy band diagram with a Fermi energy E_F at equilibrium, and all the usual pictures of band bending, surface states, Schottky barrier and ohmic contact etc. apply.

We have made no distinction among insulator, semiconductor and normal conductor. They only differ quantitatively. But we shall distinguish between a forbidden gap and an energy band.

At zero voltage across the sandwich, that region where E_F falls within a forbidden gap is a barrier region. When E_F falls within an energy band, it is an N region.

The distinction is intuitive. In a superconductor, the net attractive interaction potential, V, due to phonon-mediated short-range interaction between electrons results in condensation of quasi-particle electrons within an energy range $\sim\Delta$ below E_F to Cooper pairs $(\vec{k}\uparrow, -\vec{k}\downarrow)$ with $\vec{k}$ corresponding to an unperturbed Fermi state in the same energy range above E_F. Hence, there must be energy states just above the background Fermi sea for real cooper pairs to exist. This is our present difference between the Φ_B and N regions of the non-superconducting layer.

The sandwich is an inhomogeneous system. We use the spatially dependent pair potential, $\Delta(r)$, which corresponds to the above gap parameter, Δ, in the spatially invariant case of the microscopic BCS theory [59].

In accordance with de Gennes' macroscopic quantum mechanical approach [60],

$$\Delta(\vec{r}) = V(\vec{r})\, F(\vec{r})$$

where $V(\vec{r})$: interaction potential

$F(\vec{r}) = \langle \psi_\uparrow(\vec{r})\, \psi_\downarrow(\vec{r}) \rangle$ is the condensation amplitude;

$\psi(\vec{r})$: annihilation field operator.

The standard notations and physical interpretations of quantum theory for a many body system apply here. For instance, $F(\vec{r})$ is the probability amplitude of finding a Cooper pair at $\vec{r}$.

For N region, $F(\vec{r})$ decays with distance away from S region. Cooper pairs, which originally have energy $\lesssim E_F$ in the superconductor can exist as real Cooper pairs there because of the availability of energy levels there.

For ϕ_B region, the Cooper pairs can tunnel across. The tunneling matrix element T depends on the barrier height, thickness and shape. For slowly varying $\phi_B(\vec{r})$, in one dimensional case,

$$T_j \propto \exp\left[-\int \sqrt{\phi_B(x)}\, dx\right]$$
$$\simeq \exp\left[-\bar{\phi}_B\, d_B\right]$$

where $\bar{\phi}_B$: mean barrier height

d_B: barrier thickness.

We consider the dirty limit

$$l \ll \xi$$

l: electron mean free path

ξ : coherence length

in which diffusion dominates. We also use the one-frequency approximation of the linearized Ginzberg-Landau equations, following the de Gennes-Werthamer approach of proximity effect [61, 62.]

Other relevant parameters are

Diffusion coefficient

$$D = \frac{1}{3} v_F l$$

Coherence length

$$\xi = \left(\frac{\hbar D}{2\pi k_B T}\right)^{1/2}$$

The boundary conditions are

1. Diffusion current is continuous

$$D\frac{dF}{dx}\bigg|_{x=0^-} = \begin{cases} 0 \text{ at surface} \\ D\frac{dF}{dx}\Big|_{x=0^+} \text{ at interface of 2 conductors} \end{cases}$$

2. Condensation amplitude normalized against density of states

$$F^N(\vec{r}) = \frac{F(\vec{r})}{N(\vec{r})}$$

is continuous

$$F^N\Big|_{x=0^-}^{x=0^+} = 0$$

3. Tunneling across barrier from conductor 1 to conductor 2

$$T^{1 \to 2} = \frac{V_2 F_2^N}{V_1 F_1^N}$$

We apply these analysis to interpret all the previous results on S-S'-S junctions. The energy band diagram, with the corresponding F^N variation for S and N and the tunneling probability T for ϕ_B are schematically represented in Fig. 3.1 - 3.5 for five types of sandwich junctions. The representation is only qualitative since some of the above arguments are strictly for dirty limit only. Fig.3.1a refers to oxide barrier and Fig.3.2 does not correspond to any reported S-S'-S configuration. These are included for completeness.

We have classified the previous results in Table 3.1 but we only include those presented with sufficient evidence for Josephson tunneling. Table 3.1 and Fig.3.1 - 3.5 are self-explanatory but we further make the following comments:

1. Purely lowering of tunneling barrier ϕ_B in semiconductor only gives Josephson tunneling for $d \lesssim 15$ nm only (Fig.3.1). For intrinsic and amorphous semiconductors, the required d is further reduced to $\lesssim 5$ nm. The latter is used by Keller and Nordman[63] with Ge and InSb barrier. Their barrier layer has high resistivity, with $\rho \gtrsim 10^5 \Omega$mm for Ge and $\rho \gtrsim 10^3 \Omega$ mm for InSb. We believe their Ge is amorphous from their fabrication process. Recrystallisation of Ge film needs an annealing temperature $T \gtrsim 400^\circ$C, while their Ge on Nb is heated to 200°C for oxidation of pinholes. Metal induced recrystallisation of Ge on Nb at a lower temperature has not been reported. The high resistivity also suggests their Ge films are amorphous.

2. With degenerate semiconductor, due to proximity effect, Josephson tunneling is possible for semiconductor thickness up to $d \lesssim 300$ nm depending on the other material parameters.

3. The Pb-Si Schottky barrier is $\phi_s \sim 0.4$ eV for cleaved Si but $\phi_s \sim 0.79$ eV for aged Si [83]. Hence, Huang and Van Duzer [80] obtained junctions with either ϕ_B or N dominating the barrier (Fig.3.4) resulting in I_J smaller or zero.

4. CdS and In are known to form ohmic contact [84]. Upon optical illumination, the optically generated holes are captured in the very long life time trapping levels, resulting in increasing conduction electron concentration and the ϕ_B lowers until the semiconductor becomes degenerate (Fig.3.3) .

5. Cardinne et al. presented the different types of I-V characteristics and interpreted them as a trend for increasing spurious currents [82]. We suggest this is a general trend of increasing damping, the characteristic changing from hysteretic to nonhysteretic. We have calculated the damping factors for three of their reported junctions following this trend. We used the damping factor of McDonald et al [15] $\frac{\tau_g}{\tau}$ and the following relationship

$$\frac{\tau_g}{\tau} = \frac{\tau_g}{R_{NN}C} \propto \frac{d}{R_{NN}}$$

The unknown externally shunted capacitance, junction areas and current densities are not considered. Their variations among junctions are assumed small and will not upset the trend in Table 3.2. Even then, the qualitative agreement with the model and computations of McDonald et el. is striking as the latter is for small S-I-S junctions at T = 0 K only.

We expect S-I-S and S-S'-S junctions of the type S-ϕ_B-S resemble each other in many respects and that their junctions are S-N-ϕ_B-N-S junctions which essentially behaves as S-ϕ_B-S junctions with V_g reduced.

3.2.3 Applications -- Present state of art

The advantages of S-S'-S junctions over oxide barrier junctions are lower capacitance and higher damping of parasitic oscillations. Only Te junctions have up to now been reported in the following applications:

1. rf-biased superconducting quantum interference devices (SQUID) [76]
2. Memory loop with a junction switching time ~ 67 ps [85,86].
3. Logic element in latching, non-latching and self-resetting mode [86], with lower Q value than oxide junctions.

As the capacitance of a junction will short the higher frequency em waves, S-S'-S junctions are expected to provide better high frequency coupling. The emitted power is [2].

$$W_r \propto Q \times \frac{d^2 J_J}{\epsilon^2} \times \frac{W l_J}{\lambda_J^2}$$

from which a higher W_r for S-S'-S junction is obvious. Yet, the microwave response of S-S'-S junction has not been reported.

Lots of S-S'-S junctions with low J_J and $I_J R_{NN}$ were attributed to:

(1) undesired oxide layer formation on top electrode from adsorbed O_2 during pinhole oxidation process

(2) higher barrier due to surface states and oxidation of the semiconductor

(3) unpredictable interdiffusion between electrode and semiconductor. Storage in liquid N_2 is required to prevent aging.

IV. THEORY

4.1 Proximity effect

We only outline the brief theoretical basis for our measurements. The relevent analysis will be discussed with the results in section VI.

4.1.1 Proximity effect for Josephson effect

From the analysis from section III, we expect the ϕ_B region must be very narrow. Alternately, a degenerate semiconductor should be used.

For a sandwich junction, $J_J(T)$ and $J_J(d)$ can provide information for the BCS interaction parameter N(O)V of the N layer. The properties are different from the simple S-ϕ_B-S junction with oxide barrier.

For S-N-S (Fig. 3.2), de Gennes showed

$$J_{JM} \propto (1 - t)^2 \quad \text{for } t \equiv \frac{T}{T_c} \lesssim 1$$
$$\propto e^{-2q_N a} \qquad (4.1)$$

For dirty limit and $T_{CN} \ll T_{CS}$

$$\text{where} \quad \frac{1}{q_{N,S}} = \xi_{N,S}\left(1 + \frac{2}{\ln \frac{T}{T_{CN,S}}}\right)^{1/2} \qquad (4.2)$$

For S-ϕ_B-N-S (Fig.3.3)

$$J_{JM} \propto F(0^+)\, F(0^-) \qquad (4.3)$$

at the ϕ_B-N interface

Using sinusoidal variation for F near the N-S interface, Rowell and Smith [87] obtained

$$J_{JM} \propto \frac{|F_o|^2}{\left[(\cosh q_N d_N)^2 + \left\{0.376 \left[\frac{\hbar v_{FS}}{l_s k_B (T_{CS} - T)}\right]^{1/2} l_N q_N \frac{N_N}{N_S} \sinh(q_N d_N)\right\}^2\right]^{1/2}} \tag{4.4}$$

With linear approximation for F and with some approximations, Greenspoon and Smith [88] showed

For $t \lesssim 1$,

$$J_{JM} \propto (1 - t)^{3/2} \tag{4.5}$$

and for $t < 0.5$,

$$J_{JM} \propto \frac{1}{q_N} \csc q_N d_N$$

$$\propto \exp(-q_N d_N) \quad \text{for } q_N d_N \gg 1 \tag{4.6}$$

For S-ϕ_B-N-ϕ_B-S (Fig. 3.4),

Seto and Van Duzer [75] showed

$$J_{JM} \propto \left[\frac{\Delta(d_N/2)}{\cosh\left(\frac{d_N/2}{\xi_{NO}}\right)}\right]^2 \frac{i}{\xi_{NO}} \tag{4.7}$$

where $$\xi_{NO} = \left(\frac{\hbar v_{FN} l_N}{6\pi k_B T}\right)^{1/2} \left(1 + \frac{2}{\ln \frac{T}{T_{CN}}}\right)^{1/2}$$

$$= \left(\frac{\hbar^3 \mu}{6\pi k_B T\, e\, m^*}\right)^{1/2} (3\pi n)^{1/3} \left(1 + \frac{2}{\ln \frac{T}{T_{CN}}}\right)^{1/2}$$

for semiconductor (4.8)

and $\Delta(\frac{d_N}{2})$ is related to the Λ and the tunneling matrix element as considered in above section.

4.1.2 Proximity effect for junction resistance

For S-N-S at $T_{CN} < T < T_{CS}$ and with $V_N > 0$, Clarke et al. [89] used the resistance measurement R(T) to estimate $N_N(0)\,V_N$ for clean limit and $T \lesssim \frac{T_{CS}}{2}$.

We show here the relation for dirty limit. Fig.4.1 show the Andreev scattering [90] process in half of a symmetrical S-N-S junction. R(T) is reduced by a factor of $\frac{x_o(T)}{d_N/2}$

$$\frac{R(T)}{R_{NN}} = \left[1 - \frac{x_o(T)}{d_N/2}\right].$$

$x_o(T)$ is given by

$$\Delta_N(x_o(T)) = k_B T$$

$$\frac{\Delta_N(x)}{\Delta_N(0^+)} = \exp(-q_N x)$$

and the continuity condition for

$$F^N \equiv \frac{F}{N} = \frac{\Delta}{N(0)V} \quad \text{at NS interface:}$$

$$\frac{\Delta_N(0^+)}{N_N(0)V_N} = \frac{\Delta_S(0^-)}{N_S(0)V_S} \quad \text{applies here.}$$

Therefore

$$\frac{R(T)}{R_{NN}} = \left\{1 - \frac{1}{q_N d_N} \ln\left[\frac{N_N(0)V_N}{N_S(0)V_S}\,\frac{\Delta_S(0^-)}{k_B T}\right]\right\}$$

For clear limit, $\Delta_S(0^-) \simeq \frac{1}{2}\Delta_S(-\infty)$ for $T \lesssim T_{CS}$

$$\text{giving} \quad \frac{N_N(0)V_N}{N_S(0)V_S} = \frac{2\,k_B T}{\Delta_S(-\infty)} \exp\left[q_N \frac{d_N}{2}\left(1 - \frac{R(T)}{R_{NN}} \right) \right] \qquad (4.9)$$

For dirty limit,

$$\frac{F_S(0^-)}{F_S(-\infty)} = \frac{b}{\xi_{GL}}$$

$$\text{where} \qquad b = \frac{N_S(0)D_S}{N_N(0)D_N} \frac{\coth(q_N d_N/2)}{q_N}$$

therefore,

$$\frac{R(T)}{R_{NN}} = \left\{ 1 - \frac{1}{q_N d_N/2} \ln \frac{V_N D_S}{V_S D_N} \frac{\Delta_S(-\infty)}{k_B T} \frac{\coth(q_N d_N/2)}{q_N \xi_{GL}} \right\} \qquad (4.10)$$

4.2 GeTe film properties

Evaporated GeTe film is a highly-doped multi-valleyed semiconductor and satisfies the theoretical criteria of Cohen [91] as a superconducting semiconductor.

This in turn implies $N(0)V > 0$ and it will be a suitable material to test the proximity effect relations.

With $\gtrsim 2\%$ deficiency in Ge, $Ge_{1-x}Te$ $(x > 0.02)$ has $n_p \gtrsim 10^{17}$ mm^{-3} and is superconducting with $T_c \sim 10^{-1}$K, depending on n_p [92-94].

It has the following room temperature parameters [94]

$$\mu \sim 10^4 \text{ mm}^2 \text{ V}^{-1}\text{S}^{-1}$$

$$\frac{m^*}{m} \sim 1$$

$$E_g \sim 0.8 \text{ eV} \quad [95]$$

Also, with $x > 0.02$, GeTe is expected to satisfy the dirty limit.

Further the bulk electron mean free path is related to mobility :

$$l = \frac{(3\pi n)^{2/3} \hbar^2 \mu}{v_F e\, m^*}$$

$l(d)$ for film thickness d can be estimated using the method of Toxen et al. [96].

Evaporated GeTe is amorphous, but it is easily recrystallised completely [6] and will form a uniform barrier for tunneling.

As prepared, it is highly doped by nonstoichiometry, making it conveniently available in degenerate form. By proximity effect, we expect Josephson effect is possible for larger thickness d and hence lower junction capacitance and improved high frequency coupling is anticipated by using GeTe for S-S'-S Josephson junction.

V. EXPERIMENTAL

5.1 Low temperature section (Fig.5.1)

We use a 5-liter superinsulated dewar (superconducting Technology Inc.), with screening of Earth's field. Magnetic field B is applied with a superconducting solenoid wound from Nb coated wire (Imperial Metal Industries Ltd., Niomax-S). The solenoid current I_H to B conversion factor is obtained from Hall-probe magnetometer measurement at room temperature and are checked against the theoretical value from calculations to show no current leakage of the solenoid winding.

Solenoid:

$$I_H/B = 33.05\ \mu T\ mA^{-1}$$

$$L = 0.196\ H \text{ at } 300\ K$$

Samples are housed in a Cu container with openings to allow for thermal stability in He gas and for access to liquid or gaseous He. The vertical position of the sample along the cryostat can be adjusted from outside without upsetting the air tight He endosure.

Temperatures above 4.2 K are achieved with the enclosed sample adjusted to a variable height above the liquid helium level.

Temperature measurement is made with a 47 Ω carbon resistor (Oxford Instruments, Allen-Bradly) or a GaAs diode (Lake Shore Cryotronics, Inc. TG 100P/M) thermally in contact with the sample container, using constant current source (Keithley 225) and voltmeter (Hewlett Packard 3465A digital multimeter).

Temperatures below 4.2K are maintained by reducing the helium vapour pressure with rotary pump (Edwards, ES 330) and pressure regulator (Lake Shore Cryotronics, Inc., 329). The vapour pressures are also taken by a Hg manometer (home made)

to give the temperatures. The accuracy with GaAs diode and helium vapour pressure is within 0.1 K. Lowest temperature achievable is $\gtrsim$2.17 K, the liquid helium λ- point.

Arrangements for liquid helium level indication, helium gas conservation, gas flow and top plate of dewar etc. are home made, and all standard cryogenic techniques and precautions are observed.

5.2 Thin film facilities and materials

Our thin films are prepared by thermal evaporation in a vacuum coating unit (Edwards 306) at a pressure of $\lesssim 2 \times 10^{-6}$ mm Hg with diffusion pump and rotary pump. Some home made modifications enables multilayer deposition up to 4 layers at variable substrate temperatures can be carried out without exposing the substrate to air. But these full facilities were not yet set up for many of the earlier samples.

The coater has a selector of 4 position sources. An open ended glass cylinder is used and the substrate holder and masks are mounted to above (Fig.5.2). Up to 4 masks can be mounted on a rotatable mask holder (Fig.5.3). The selected mask fits to the substrate holder through alignment slots. The substrate is held up side down by screws at the 4 corners of the substrate. Inert photoresist drops are first applied to the corners and dried, so that the screw ring edges hold the substrate rigidly without causing undue strain (Fig.5.4a) Corresponding holes are made on the masks and mask holders so that the mask can pass through the screws and touch the substrate (Fig.5.4b). The substrate holder is mounted at the center of the top cover to a Cu block, which can either be cooled or heated. The block is attached to the bottom of a stainless steel cup with double wall at the upper part to provide thermal insulation from the top cover. Cooling is through conduction with ice or liquid N_2 added to the cup.

Alternately, it can be heated with filament winding, which is electrically insulated by mica sheets. (Fig.5.5) The temperature of the substrate is measured with chromel-constantan thermal couple attached to the substrate holder with GE vanish.

The wide junction masks are made by chemically etching on Mo sheet using standard photographic technique. For small junction incorporated with MIC, we used Cu-Be bimetallic mask, Ni plated in the Allied-Kelite process (Richardson CO.)

Ordinary microscope glass slides when used as substrates are found to yield films of poorer texture. Flat pyrex glass substrates of size 23 x 26 x 1.4 mm are used. But for junctions requiring microwave coupling, we use the Corning pyrex glass substrates (Corning 7059) of 25.4 x 25.4 x 0.813 mm size and within $\sim$6 nm smoothness. The dielectric constant is $\epsilon_r \simeq 5.75$ and tangent loss is $\tan\delta \simeq 0.0036$ at 7 - 8 GHz at room temperature.

Before use, the ordinary pyrex glass is washed successively with Chromic acid, mixture of Aqueous NH_3 solution, H_2O_2, H_2O (1:1:5) and mixture of HCl, H_2O_2, H_2O (1:5:2 5) at 80°C, rinsing with deionized water after each step and baked dry in oven.

Corning glass is attacked by strong chemicals and is washed with the "Micro" cleaning solution (International Products Corp.) at 60°C and with deionized water in ultrasonic cleaner.

For electrode film, we use Pb, $Pb_{0.9}In_{0.1}$ or Sn. The raw metal lumps are cut from metal ingots (Ventron, 99.999 % pure). $Pb_{0.9}In_{0.1}$ is prepared by alloying the weighed metals in clean glass tube sealed under vacuum. Pb and $Pb_{0.9}In_{0.1}$ are evaporated from Mo boat. Sn is evaporated from Ta boat with Ta wires wrapping the Sn lump to provide reduction of tin oxide formed even in high vacuum [98].

The metal films show little features (Fig.5.6a) under polarized optical microscope (Leitz Orthoplan 810753)

but irregularities begin to appear for a film thickness $\gtrsim$300 nm or when handled less skillfully (Fig.5.6b).

We use Ge or GeTe as semiconducting barrier. They are evaporated from a Al_2O_3 crucible (R.D.Mathis Co., C9 - AO), heated by W wire from outside. A metal foil radiation shield (home made) is used to prevent heating of other parts of the coater, so that pressure does not rise above 2×10^{-6} mm Hg during slow evaporation.

Doped Ge is prepared by melting weighed Ge and Al in vacuum sealed quartz tube in oven at $\sim 1100^{\circ}C$ and quenching in water to prevent segregation. GeTe is prepared similarly from Ge and Te, but commercially prepared GeTe (Materials Research Corporation) is used in the later samples. Resistivity measurements of GeTe film from both sources show the same recrystallization characteristics.

Film thickness measurements and monitoring are made with a circuit (home made) to measure the oscillation frequency change of a water cooled 6 MHz crystal (Marconi Co.Ltd. Q01670A) as the film is simultaneously deposited on it. It has been calibrated against optical interference measurements on thicker film. Direct weighing method is also used with electronic balance.

5.3 Laser induced recrystallization

Laser spot is used to recrystallize GeTe film. We use a power laser system (Laser Associates 211 Laser system) with *ruby* laser of $\sim$ 1 ms pulse time and maximum power $\sim$ 20 J, but the required power for recrystallization of GeTe is generally within 1 J, being larger for smaller film thickness. Calibrated filters are used to reduce the power.

Power measurement is by direct measurement with photocell and power meter in a calibration pulse immediately before each actual recrystallization pulse. The photocell blocks the sample in the calibration and, in cases of very low power, the filters are taken off in the calibration, to be corrected mathematically latter.

Alignment of the samples's position is made at the continuous mode of the laser.

We expect to get small recrystallized spot by focussing the laser beam, but our crude lens can only give ~1 mm diameter beam spot. We managed by using low power, increasing successively up to the threshold value, when recrystallized spots just begin to appear on the GeTe film. With care and practice, recrystallized spots of ~70μm in diameter are possible.

5.4 DC measurement

The dc measuring system is shown in the block diagram (Fig.5.7), using the following equipments:

Control box (home made)

dc supply (Farnell L30DT Dual stabilized power supply)

dc voltmeter (Keithley 155 Microvolt nulldetector or Keithley 147 Nanovolt null detector)

Sine wave generator (Farnell LFM2 Sine-square oscillator)

Reference Unit (Brookdeal 422)

Low noise amplifier (Brookdeal 450)

Coherent filter (Brookdeal 467)

Phase sensitive detector (Brookdeal 411)

X - Y recorder (Hewlett Packard 7035B)

Constant current supply (home made), with heavy capacitive damping to prevent I_H transients and oscillations.

Ammeter (Hewlett Packard 3465A digital multimeter)

Four probe measurement is used for the junction, and the junction supply can be entirely flating and operated by battery only for the lower power level operations.

The sine wave generator floating output, dc voltmeter and X - Y recorder x-axis floating input share a common potential reference with the junction voltage feedback. The battery/dc supply floating output and the control box circuit share another common reference potential. Screened floating double-line cable is used, and the screening is common to the control box case, which is grounded through the cryostat case. All the other measuring instruments are dc isolated from them. Low noise coaxial cable is used for the PSD system.

Extreme care is exercised against noise, ground loop and transients, except that the room is not screened.

5.5 AC measurement

Microwave can only be applied to the junction in our system.

Loss of microwave power in microstripline is minimized by enclosing the sample in a microstrip box (home made) (Fig. 5.8a) A thin Pb foil between the substrate and a backing Cu plate is used as a superconducting ground plane for the stripline and to provide soft backing when fixing the subtrate rigidly (Fig.5.9).

A cryogenic semi-rigid coaxial cable, which has Cu coated stainless steel outer shield, is coupled through a launcher (OSM244-16002) to a 50Ω microstripline of the MIC on the substrate. A tiny soft In

bead soldered to the stripline after coated with photoresist provides good contact to the launcher.

The upper part of the coaxial cable is enclosed in a hollow stainless steel rod. The dc lead wires to the substrate also go through the rod and the two ends of the rod is vacuum sealed with low temperature epoxy.

The rod's vertical position is adjustable by sliding through air-tight rubber O-ring at a top cover (Fig.5.10a,b)

The following microwave connectors are used depending on the required connections:

(Ommi Spectra)

OSM 21030	Jack/N adaptor
OSM 218	Plug/plug
OSM 216	Jack/plug
OSM 219	right angle jack/plug

The Jack/N adaptor is joined through flexible coaxial cable (Alpha wire 92194 RG-214/U) and standard connectors (Hewlett Packard or RS) to a microwave source (Hewlett Packard 8690B Sweep oscillator) at the 4 - 8 GHz frequency range (Hewlett Packard 8693A). Fixed attenuators (Hewlett Paclard 8492A 10dB or 30 dB) are inserted for the lower power measurements.

The applied rf power to the microstrip box launcher from the source through the composite circuit of cables and connectors is calibrated against the source output dial by measuring the power at the launcher end of the cryogenic coaxial cable. The calibration

is, however, only carried out at room temperature outside the cryostat with a power meter (Hewlett Packard 432A).

5.6 Microstrip design

The complete microstrip circuit (Fig.5.8a) consists of two independently biased junctions in series connection (Fig.5.8b), two half wavelength resonators along a 50Ω microstripline, and three low pass filters for dc leads. Each junction is coupled to an end of an external cavity. The junctions are of cross-type but in-line electrode configuration is used. Each junction, therefore, need two filters for dc connections, one filter being shared by both junctions.

The upper resonator, of a 9.4 mm length of 50Ω line and with a lowest resonance frequency of ~7.255 GHz, is formed by a cut from the vertical 50Ω line so that the microwave source is dc isolated from the junction. The lower resonator, with the upper end coupled to the junction, has the lower end coupled through a launcher to a 50Ω termination load outside the microstrip box.

The filters provide ac isolation between the junction and the dc leads. The Elliptic function low pass filter, designed using design data reference [99] give >30 dB attenuation at the resonator frequency. The prototype, microstrip realization and their performance have been given elsewhere [100] and we reproduce the figures here (Fig.5.11).

VI EXPERIMENTAL RESULTS AND DISCUSSIONS

Our results with Ge barrier will be discussed elsewhere (Appendix IV). Here, we discuss our fabrication method and results with GeTe. But, before that, we show very briefly our results with amorphous GeTe barrier and large area junctions.

6.1 With amorphous GeTe

GeTe evaporated at room temperature is amorphous and has a high resistivity of $\sim 10^3 \Omega$ mm. We had previously mentioned quasiparticle tunneling with amorphous GeTe barrier [8]. We now present the results for $Pb_{0.9}In_{0.1}$—GeTe—$Pb_{0.9}In_{0.1}$ junction of $d \simeq 20$ nm. Fig.6.1 shows the I-V characteristic and $-\frac{dV}{dI}$ vs. V. The I-V characteristic shows the quasiparticle tunneling and the energy gap. The amorphous GeTe barrier junction has a high resistance, so that $\frac{dI}{dV} \sim -\frac{dV}{dI}$.

In additional to 2Δ, there are two other conductivity maxima, due to longitudinal/transverse phonon spectrum $\alpha^2(w)F(w)$ of the strong-coupling superconductor used as electrodes. Their energies agree with the first and second spectrum peaks of Pb, but the smaller peak corresponding to impurity states of In in Pb is not resolvable. The rectifying nature is due to junction's inherent assymmetry caused by interdiffusion or oxidation. The evaporated amorphous GeTe

is ~9% less dense than the bulk simiconductor [6]. This suggests locations for O_2 absorption and adsorption causing oxidation of the upper Pb film. For oxide barrier junction, the present spectrum had been reported by a number of workers. Second derivative is also used to extract information from the tunneling characteristics and the information is used to calculate the phonon spectrum and to test the theory for strong-coupling superconductor. This has been reviewed by McMillan and Rowell. In our present case, we show that a high resistivity semiconductor such as amorphous GeTe can also serve as a tunneling barrier for the investigations.

6.2 Crystallised GeTe imperfect junction

Fig.6.2 shows the results for a recrystallised GeTe wide junction which is imperfect as indicated by a SLUG type $I_J(H)$. GeTe is crystallized with a substrate temperature of 170°C during evaporation. The junction resistance is higher than that expected from the resistivity ρ_c of crystallised GeTe and junction geometry showing possible interdiffusion at the high temperature used. There is also increased possibility of getting micro-shorts due to possible grain motion of the base electrode during and after heat treatment. The microshort behaviour is shown in Fig.6.2a, with subsequent subharmonic structures shown in Fig.6.2b. R(T) vs. T in Fig.6.2c gives the qualitatively expected decrease of R(T) for decreasing T, as discussed in section 4.1.2 for S-N-S sandwich.

6.3 Thermally crystallized GeTe

The above results show high temperature treatment is undesirable. We tried to crystallise GeTe at a lower temperature. This means we had to try heated substrate with $T_{sub} \gtrsim 130^{\circ}C$ during evaporation rather than heating the substrate to $T \gtrsim 150^{\circ}C$ after evaporation of the semiconductor film. The substrate is then immediately but smoothly cooled down to $T_{sub} \simeq 60^{\circ}C$ for pinhole oxidation.

The crystallisation of GeTe film is indicated by four probe resistance measurement of a simultaneously evaporated GeTe film. We also compare the resistances R_{+} and $R_{//}$ of parallel films of GeTe and Pb for overlapping and non-overlapping configurations (Fig. 6.3a). This crude method serves as qualitative indications for severe interdiffusion. The results show that $R_{+} > R_{//}$ by $\sim$10% as T is increased above $\sim 150^{\circ}C$.

The GeTe junctions thus prepared with GeTe completely crystallised are superconducting up to the critical temperature of the superconducting electrode films. The film turning normal is characterized by reversed voltage due to the inexact four probe resistance measuring method with normal electrode films [102]. The oxidation conditions have been checked against an oxide junction on the same substrate (Fig. 6.3b).

6.4 Junction with thermally crystallized GeTe

We reduce the effective junction area by using $T_{sub} \simeq 130^{o}C$. We tried with samples for which the resistance $R_{//}$ of the monitoring film shows no measurable crystallisation. This is however only a rough guide due to different materials of Pb and glass for the GeTe film. This is reported in Appendix III.

We expect the existence of some microscopic cystallized nuclei grains. As the resistivity of amorphous GeTe is much higher, $\frac{\rho_a}{\rho_c} \sim 10^7$, the rest of the semiconductor can be regarded as very thick insulating barrier giving no Josephson effect.

Fig. 6.3a shows the I_J (H) for such a Pb - GeTe - Pb junction. This shows evidence of Josephson tunneling but the I_J(H) is not well behaved. This is expected from the irregular geometry; the Fraunhofer diffraction pattern holds for uniform rectangular barrier only. The I_J(H) appears to have a smaller period (B_1=2,3mT) modulated heavily by a larger period (B_2=8mT).

Using $W_i(2\lambda_L + d)B_i = \Phi_o$ for one flux quantum enclosed in the junction and

λ_L = 43nm, which is an average value over some literature values [44, 97],

$2\lambda_L + d \simeq 126$nm.

The B_i's correspond to effective junction widths of

$W_1 = 7.1 \mu m$

$W_2 = 2.1 \mu m$

which agrees in order of magnitude to a nucleation nucleus.

The junction has $R_{NN} \simeq 6\ m\Omega$. A short of Pb bridge of the dimension W would give a much greater I_{JM}:

$$I_{JM}R_{NN} \lesssim 0.78 \times \frac{\pi}{2}\Delta(T)\tanh\frac{\Delta(T)}{2kT} \simeq 1.6\ meV$$

$$I_{JM} \lesssim 0.6A$$

and is therefore unlikely.

On the other hand, assuming the effective junction area A* lies in the range

$$W_2^2 < A^* < W_1^2$$

gives $0.7 \times 10^{-3} < \rho < 8 \times 10^{-3}\ \Omega mm$

which agrees with ρ_c for GeTe.

The maximum critical density is

$$J_{JM} \simeq 1.3 \times 10^2\ A\ mm^{-2} \sim 10^5 mA\ mm^{-2}\ (10^4 A\ cm^{-2})$$

where $A^* \simeq \left(\frac{W_1 + W_2}{2}\right)^2$ is used.

This is probably the highest reported for semiconductor barrier junction. For oxide junction, J_{JM} as high as $\sim 10^6 mA\ mm^{-2}$ has only been reported for very small $Pb_{.9}\ In_{.1}$ oxide junctions.

The Josephson penetration depth is

$$\lambda_J = \left[\frac{\hbar}{2e\mu_0 J_J d}\right]^{1/2}$$

$$\simeq 7\mu m$$

where $A^* \simeq \left(\frac{W_1 + W_2}{2}\right)^2$ is used.

This corresponds to a small junction, as is also seen from the $I_J(H)$, which is only slightly inclined due to small contribution from self-field.

The $I_J R_{NN}$, $\simeq 16\mu V$, is significantly lower than the theoretical value of Ambegaokar and Baratoff, but is already much larger than

most reported S-S'-S junctions [2] in the early stage of this type of work.

We have also qualitative inferred a supercurrent density distribution using the method of Dynes and Fulton [67], and using an effective rectangular geometry for the junction. This is also shown in Fig. 6.4a. The fact that J_J is more concentrated at the centre is anticipated from the geometry of a growing nucleus of crystallization.

Fig. 6.4b shows the $I_J(T)$. The spread of data is due to self-field and interference for an irregular geometry. There is insufficient data to fit to the models but there is apparently some resemblance to the $I_J(T)$ of S-$\emptyset_B$-N-S or S-$\emptyset_B$-N-$\emptyset_B$-S for certain parameters, but not S-N-S. Φ_B region can be formed by interdiffusion or surface states.

The I-V characteristic is shown in the inscription of Fig. 6.4b.

6.5 Junction with laser-crystallized GeTe.

The success of the above junction fabrication method depends on the existence of one and only one crystallisation nucleus only in the whole junction area. Otherwise, there is quasiparticle tunneling only. The $I_J(H)$ is of SLUG type due to interference between a number of junctions and is indistinguishable from microshorts. The reproducibility is certainly poor.

We develop the following method to crystalline GeTe by laser. This has a further advantage of reducing interdiffusion at the high substrate temperature required for evaporation.

6.5.1 Fabrication

The general experimental detail is given in Section V. The following describes some particular fabrication steps of a sample to be discussed here.

Pb film of $d \lesssim 200$nm and with filter section (Fig. 6.4a) and connection pads is first evaporated on a corning glass substrate. GeTe evaporation follows (Fig. 6.4b) after about 20 minutes to allow for crystal stabilization of the Pb film. The chamber is then filled with O_2 to atmospheric pressure, and the substrate heated to $T_{sub} \simeq 60^{\circ}C$ for 15 minutes. We believe this preliminary pinhole oxidation procedure will avoid oxidation inhibition due to adsorption of N_2 on Pb surface when the sample is exposed to air. The sample is unloaded from the chamber for laser induced crystallization (Appendix III) of a tiny spot. Time of exposure of the sample to air is made as short as possible. The sample is replaced into the chamber, which is then evacuated and filled up with O_2 to repeat the above pinhole oxidation procedure. The final top Pb film to be evaporated contains also the resonators (Fig. 6.4c). The sample is spinned a thin coating of photoresist as a protective layer as well as for soldering of lead wires with In directly on the film. The completed MIC sample has been shown above (Fig. 5.8).

6.5.2 dc properties

Fig.6.6a shows the $I_J(H)$. Again, the junction is not a uniform and rectangular one. The I-V characteristic (Fig.6.6b) is non-hysteretic. The I-V at B = 6.6mT shows the junction is actually a Josephson junction or at least the by far major supercurrent component is due to Josephson tunneling.

Using the same analysis as for the thermally crystallized junction, but assuming this time a circular grain of cystalline GeTe, we obtain the following parameters:

$B_{period} \simeq 0.37mT$

Effective junction diameter:

$2r^* \simeq 45\mu m$

$A^* \simeq 1.6 \times 10^3 \mu m^2$

$J_{JM} \simeq 11 \times 10^3$ mA mm^{-2}

$\sim 10^4$ mA mm^{-2} (10^3 A cm^{-2})

$R_{NN} \simeq 5.5$ mΩ

$I_J R_{NN} \simeq 97\mu V$

$\lambda_J \simeq 24\mu m$

As $\frac{2r^*}{\lambda_J} \sim 1.9$, this corresponds a little self-field effect. The junction capacitance is

$$C = \frac{\epsilon A^*}{d} \sim 1pF$$

but it is shunted by the parallel capacitance of $C \sim 10pF$ of the amorphous GeTe region.

The above values can only be regarded as order of magnitude estimates due to the uncertainty of actual junction geometry. We had not examined with optical microscope the crystalline GeTe geometry prior to evaporation of top electrode for technical problems against the requirement to avoid exposing the sample to air for longer time. We also have not examined it by first destructively etching away the Pb electrode in order to conserve the junction for future measurements.

Compared with the previous junction, this junction has larger A^*, smaller J_{JM}, but higher $I_J R_{NN}$. This may be

qualitatively explained by an increased barrier region ℓ_B. This is anticipated from the R_{NN} value which is comparatively higher than when R_{NN} is due to ρ_c of GeTe only. Hence I_J decreases but it is overcompensated by the increase in R_{NN} to get a higher $I_J R_{NN}$. The 2 S-S' interfaces are not symmetrical as can be observed in the asymmetry of the I-V characteristics (Fig. 6.6b). The increased ϕ_B might be due to the oxidation conditions. In the previous junction, pinhole oxidation is carried out after GeTe is crystallized and is roughly as compact as bulk [6]. For this junction, the preliminary pinhole oxidation can cause O_2 absorption and oxidation as the GeTe is still amorphous and probably somewhat porous.

6.5.3 ac properties

With the low R_{NN} and high J_J, we expect the junction will respond very well to applied radiation. Fig. 6.7a shows the microwave induced steps. The low order current steps are very large, but it drops off rapidly for the increasing orders.

Fig. 6.7b shows the dependence of the 0 - 2 orders current step amplitudes I_{step} on the applied e.m. wave amplitude. They are fitted to the theoretical Bessel functions of the respective orders. The spread of the data points is partly due to self-field and irregular junction geometry.

Actually our sample configuration consists of 2 coupled junctions. This will permit investigation of interactions of the 2-junction array. We expect such a high supercurrent density junction is very suitable for such investigations.

For this sample, however, the other junction barrier crystallization fails with our crude laser focusing technique.

VII. CONCLUSION

Previous works on S-S'-S junctions with other semiconductors have been reviewed with some suggestions for interpretation.

For our present junctions with GeTe, very high Josephson current density is possible when the semiconductor is crystallized as a highly self-doped p-type semiconductor. In the high-resistivity and amorphous form, GeTe will behave as an insulating barrier and the quasiparticle tunneling data give the phonon spectrum of the strong-coupling superconductor used as electrodes. GeTe crystallisation can be accomplished by thermal means or by laser irradiation. The short laser pulse time ensures minimization of interdiffusion between the semiconductor and electrode for semiconductors requiring high temperature annealing to get the crystallised form.

The use of laser induced recrystallisation is a new method to reduce junction area by focusing the laser beam. It also opens new aspects of applying laser writing techniques to the fabrication of Josephson devices of various junction geometries. It utilizes both the inherent advantages of a semiconductor barrier and laser writing technology. In particular, interference devices and arrays should be possible with semiconducting chalcogenide films. Still better resolution might be achieved with electron lithographic techniques.

For $d \gtrsim 40$nm, the I-V is non-hysteretic. We are planning to vary the semiconductor thickness to find N(O)V for

comparison with proximity effect theory, and to see whether it will be hysteretic with reduced semiconductor thickness in accordance with the model of McDonald et al [15].

The ac properties of both junctions and junction arrays of S-S'-S have not been properly investigated. With very high supercurrent density for thick barrier, which can be interpreted in terms of a proximity effect model, the present GeTe barrier junctions are, at least theoretically, very suitable for ac Josephson effect applications. We have shown that it responds sensitively to applied e.m. wave for the lower order $\frac{nh\nu}{2e}$ constant voltage steps. We expect it will also emit radiation strongly and the junctions array will exhibit stronger interactions than the oxide counterparts. We also plan for investigations in this line. Hopefully, we might be able to present those coming results elsewhere in the near future.

		d/nm	sandwiched layer	Ref.
1. S-ϕ_B-S	(a) $\phi_B \gtrsim 1$ eV	~ 2	oxide	
	(b) $\phi_B \sim 10^{1-2}$ meV	$\lesssim 5$	Ge, InSb	63
	(c) $\phi_B \sim 10^{1-2}$ meV	< 15	CdS	64 - 68
2. S-N-S		$\lesssim 700$	Normal metal ----Cu	69
		$\lesssim 300$	Semimetal -------Bi	70
			Degenerate semiconductor	
3. S-ϕ_B-N-S		< 75	CdS (Pb-CdS-In)	71 - 73
4. S-ϕ_B-N-ϕ_B-S		< 100	Degenerate Te	74 - 76
		40, 125	Degenerate Si (sandwich junction)	77 - 80
		100, 300	Degenerate Si (planar junction)	
5. S-N-ϕ_B-N-S		$10 \lesssim d \lesssim 20$	PbTe	81, 82

TABLE 3.1 Models for previous semiconductor-barrier junctions

TABLE 3.2 Calculation of damping factor of McDonald et al [15] from the data of semiconductor-barrier junctions of Cardinne et al. [82]

Type	Semiconductor thickness d/nm	Normal junction resistance R_{NN}/Ω	Damping factor $\frac{\tau}{\tau_g} \propto \frac{d}{R_{NN}}$ (arbitrary scale)
1 (most hysteretic)	10	9.62	1
2	13	0.76	17
3 (non-hysteretic)	18	0.017	1060

REFERENCES

[1] Chan H.W., Lum W.Y. and Van Duzer T.
High-speed switching and logic circuits using Josephson devices
IEEE Trans. Mag. MAG-11, 770 March 1975

[2] Cardinne P., Nordman J. and Renard M.
On the use of low barrier potential materials to improve high frequency coupling to Josephson tunnel junctions
Rev. Phys. Appl. 9, 167, January 1974

[3] Konig B.
Tunneling with Ge - barrier
Phys. Lett. 39 A, 117, April 1972

[4] Lipson S.G. and Stupel M.M.
Induced superconductivity in germanium films
Phys. Lett. 33A, 493, December 1970

[5] Keller W.H. and Nordman J.E.
Niobium thin-film Josephson junctions using a semiconductor barrier
J. Appl, Phys. 44, 4732, October 1973

[6] Chopra K.L. and Bahl S.K.
Amorphous versus crystalline GeTe films. I. Growth and structural behaviour
J. Appl. Phys. 40, 4171, Sept. 1969

[7] Hein R.A., Gibson J.W., Mazelsky R., Miller R.C. and Hulm J.K.
Superconductivity in Germanium telluride
Phys. Rev. Lett. 12, 320, March 1964

[8] Chan H.H.A. and Chang C.C.
Voltage-switching effect in evaporated weak-link junctions
J. Phys. D: Appl. Phys. 10, L33, 1977

[9] Rogovin D, and Scully M,
Superconductivity and macroscopic quantum approach
Phys. Lett. (Physics Reports) 25C, 175 June 1976

[10] Josephson B.D.
Possible new effects in superconductive tunneling
Phys. Lett. 1, 251 July 1962
Coupled superconductors
Rev. Mod. Phys. 36, 216 January 1964
Supercurrents through barriers
Adv. Phys. 14, 419 October 1965

[11] Pedersen N.F.,Finnegan T.F. and Langenberg D.N.
Evidence for the existence of the Josephson quasiparticle-pair
interference current
Low Temp. Phys. - LT 13 3, 268 (1974)

[12] Stewart W.C.
Current-voltage characteristics of superconducting tunnel junctions
J. Appl. Phys. 45, 452 January 1974

[13] McCumber D.E.
Effect of a.c. impedance on voltage-current characteristics of
superconductor weak-link junctions
J. Appl. Phys. 39, 3113 June 1968

[14] Skocpol W.J., Beasley M.R., and Tinkham M.
Self-heating hotspots in superconducting thin film microbridges
J. Appl, Phys. 45, 4054 Sept. 1974

[15] McDonald D.G., Jo on E.G. and Harris R.E.
Modeling Josephson junctions
Phys. Rev. B 13, 1028 February 1976

[16] Werthamer N.R.
Nonlinear self-coupling of Josephson radiation in superconducting tunnel junctions
Phys. Rev. 147, 255 (1966)

[17] Riedel E.
Z. Naturforsch 19A, 1634 (1964)

[18] Ambegaokar V. and Baratoff A.
Tunneling between superconductors
Phys. Rev. Lett. 10, 486 (1963)
Phys. Rev Lett. 11, 104(E) (1963)

[19] Fulton T.A and McCumber D.E.
dc Josephson effect for strong-coupling superconductors
Phys. Rev. 175, 585 November 1968

[20] Rowell J.M.

Phys. Rev. Lett. 11, 200 (1963)

[21] Anderson P.W. and Rowell J.M.

Probable observation of the Josephson superconductive tunneling effect.

Phys. Rev. Lett. 10, 230 (1963)

[22] Ferrell R.A. and Prange R.E.

Self-field limiting of Josephson tunneling of Superconducting

electron pairs

Phys. Rev. Lett. 10, 479 June 1963

[23] Jaklevic R.C., Lambe J., Mercereau J.E. and Silver A.H.

Macroscopic quantum interference in superconductors

Phys. Rev. 140, A 1628, November 1965

[24] Clarke J.

A superconducting galvanometer employing Josephson tunneling

Phil. Mag. 13, 115 (1966)

[25] Shapiro S.

Josephson currents in superconductive tunneling: The effect of microwave and other observations.

Phys. Rev Lett. 11, 80 (1963)

[26] Fiske M.D.

Temperature and magnetic field dependences of the Josephson tunneling current

Rev. Mod. Phys. 36, 221 (1964)

[27] Swihart J.C.

Field solution for a thin-film superconducting strip transmission line.

J. Appl. Phys. 32, 461 (1961)

[28] Solymar L.

Superconductive tunnelling and applications

Chapman and Hall Ltd. 1972

[29] Emmanuel A., Donaldson G.B., Band W.T. and Dew-Hughes D.

Barrier formation in Lead-based tunnel junctions studied by surface techniques

IEEE Trans. Mag. MAG - 11, 763 February 1975

[30] Private commumication

[31] Lahiri S.K.

Metallurgical considerations with respect to electrodes and interconnection lines for Josephson tunneling circuits

J. Vac. Sci. Technol. 13 - 1, 148 Jan./Feb. 1976

[32] Eldridge J.M. and Matisoo J.

Measurement of tunnel current density in a metal-oxide-metal system as a function of oxide thickness.

"Low Temperature Physics" LT -12, 427 (1970)

[33] Niemeyer J. and Lose V.

Effects in high critical current density Josephson tunnel junctions

Conference on superconducting quantum devices (W.Berlin),

October 1976

[34] Niemeyer J. and Kose V.

Observation of large dc supercurrents at nonzero voltages in Josephson tunnel junctions

Appl. Phys. Lett. 29, 380 September 1976

[35] Sirkeinen Y., Somervuo P. and Wiik T.
The stripline coupling of thin-film Josephson junctions to external circuits at microwave frequencies
Rev. Phys. Appl. 9, 131, (1974)

[36] Finnegan T.F., Wilson J. and Toots J.
Interactions in small systems of coupled Josephson junctions at microwave frequecies
Rev. Phys. Appl. 9, 199 (1974)

[37] Finnegan T.F., Holdeman L. B. and Wahlsten S.
Microwave phenomena in thin-film Josephson junctions coupled to a contiguous cicrostrip resonator
IEEE Trans. Mag. MAG - 13, 392, January 1977

[38] Dziuba R.F., Field B.F. and Finnegan T.F.
Cryogenic voltage comparator system for 2e/h measurements
IEEE Trans. Instrum. measurement IM - 23, 264, December 1975

[39] Zapple H.H.
Josephson quantum interference computer devices
IEEE Trans. Mag. MAG - 13, 41 January 1977

[40] Fulton T.A., Dunkelberger L.N. and Dynes R.C.
Quantum interference properties of double Josephson junctions
Phys. Rev. B 6, 855. (1972)

[41] Zapple H.H.
A single flux-quantum Josephson junction memory cell
Appl. Phys. Lett. 25, 424 (1974)

42 Guerer P., Mohr Th. O. and Wolf P.

Single flux-quantum memory cells

IEEE Trans. Mag. MAG - 13, 52 January 1977

43 Shapiro S., Smith P.H., Nicol J., Miles J.L. and Strong P.F.

Superconductivity and electron tunneling.

IBM J. Res. Dev. 6, 34 (1962)

44 Schwidtal K. and Finnegan R.D.

J. Appl. Phys. 40, 2123 (1969)

45 MacVicar M.L.A., Freake S.M. and Adkins C.J.

Thin semiconducting films as tunneling barriers

J. Vac. Sc. Technol. 6, 717 (1969)

46 Rissman P.

Photosensitivity in superconducting tunnel junctions with a

Cadmium senlenide barrier

J.Appl. Phys. 44, 1893 (1973)

47 Tsuboi T.

Photosensitive tunnel junctions and photosensitive granular

films with Te or Se barriers

Phys. Lett. 56A, 472 May 1976

48 Wright H.C., Downey R.J. and Canning J.R.

Conductivity storage in CdS

J. Phys. D 2, 1593 (1968)

[49] Bube R.H.

"Photoconductivity of solids", Wiley, New York, 1960

[50] Holm R.

The electric tunnel effect across thin insulator films in contacts

J. Appl. Phys. 22, 569 (1951)

[51] Josefowcz J. and Smith H.J.T.

Tunnelling in junctions with CdS barriers

J. Appl, Phys. 44, 2813 June 1973

[52] Lubberts G.

Longitudinal optical phonons in thin films of CdS, CdSe, and their mextures

Phys. Rev. B3, 1965 March 1971

[53] Duke C.B.

in " Tunneling phenomena in solids"

edited by Burstein E. and Lungvist S., Plenum, New York, 1969, chap.4

[54] Lubberts G. and Shapiro S.

Cadmium selenide films deposited at high substrate temperature as tunneling barriers between tin electrodes

J. Appl. Phys. 43, 3958 Oct. 1972

[55] Wyatt P.W., Barker R.C. and Yelon A.

Tunneling study of the superconducting proximity effect in the thin-normal limit

Phys. Rev. B6, 4169 (1972)

[56] Frommer M.H., MacVicar M.L.A. and Rose R.M.
Anomalous tunneling characteristics
Low Temp. Phys. - LT 13 3, 306 (1972)

[57] Knotek M/L.
Transport of oxygen in amorphous Ge thin films during annealing
J. Vac. Technol. 12, 117 (1975)

[58] Shen L.Y.L.
in "Proc. Conf. Superconductivity in d- and f- Band Metals"
Douglas D.H., ed. AIP. New York (1972), p.31

[59] Bardeen J., Cooper L.N., and Schrieffer J.R.
Theory of superconductivity
Phys. Rev. 108, 1175 (1957)

[60] de Gennes P.C.
Boundary effects in superconductors
Rev. Mod. Phys. 36, 225 (1964)

[61] de Gennes P.C.
"Superconductivity of Metals and Alloys"
Benjamin, New York (1969)

[62] Werthamer N.R.
Theory of the superconducting transition temperature and
energy gap function of superposed metal films
Phys. Rev. 132, 2440 (1963)

[63] Keller W.H. and Nordman J.E.
Niobium thin-film Josephson junctions using a semiconductor barrier
J. Appl. Phys. 44, 4732 October 1973

[64] Giaever I.
Photosensitve tunneling and superconducting
Phys. Rev. Lett. 20, 1286 (1968)

[65] Giaever I. and Zeller H.R.
Tunneling into and through evaporated semiconductor
J. Vac. Sc. Tech. 6, 502 (1969)

[66] Giaever I. and Zeller H.R.
Subharmonic structure in superconductive tunneling
Phys. Rev. B1, 4278 (1970)

[67] Dynes D.C. and T.A. Fulton
Supercurrent density distribution in Josephson junctions
Phys. Rev. B3, 3015 (1971)

[68] Barone A., Rissman P. and Russo M.
Effect of preparation parameters on light sensitivity in superconductive tunnel junction
Rev. Phys. Appl. 9, 73 (1974)

[69] Clarke J.
Supercurrents in lead-copper-lead sandwiches
Proc. Roy. Soc. A308, 447 (1969)

[70] Ohta H., Feldman M.J., Parrish P.T. and Chiao R.Y.
Semimetal barrier planar Josephson junction
Rev. Phys. Appl. 9, 187 (1974)

[71] Barone A. and Russo M.
Observation of light induced Josephson current through "thick" CdS barriers
Phys. Lett. 49A, 45 (1974)

[72] Barone A., Paterno G., Russo M. and Vaglio R.
Experimental results on temperature and magnetic field dependence of light induced Josephson current
"Low Temperature Physics" LT - 14 2, 88 (1975)

[73] Barone A., Paterno G., Russo M. and Vaglio R.
Light-induced transition from "small" to "large"Josephson junctions
Phys. Lett. 53A, 393 (1975)

[74] Seto J. and Van Duzer T.
Supercurrent tunneling junctions with Te barriers
Appl, Phys, Lett. 19, 488 (1971)

[75] Seto J. and Van Duzer T.
Theory and measurements on lead-tellurium-lead supercurrent junctions
"Low Temperature Physic" LT - 13 3, 328 (1972)

[76] Simmonds M.B.
Using the semiconductor junction in quantum interference devices
J. Appl, Phys. 45, 366 (1974)

[77] Huang C.L. and Van Duzer T.
Josephson tunneling through locally thinned silicon wafers
Appl. Phys. Lett. 25, 753 (1974)

[78] Huang C.L. and Van Duzer T.
Single-crystal silicon-barrier Josephson junctions
IEEE Tranc. Mag. MAG - 11, 766 (1975)

[79] Huang C.L. and Van Duzer T.
Schottky diode and other devices on thin silicon membrane
IEEE Trans. Electron Devices ED - 23, 579 (1976)

[80] Schyfter M., Maah-Sango J., Raly N., Ruby R., Ulrich B.T. and Van Duzer T.
Silicon-barrier Josephson junctions in coplanar and sandwich configuations
IEEE Trans. Mag. MAG -13, 862 (1977)

[81] Cardinne Ph., Marti M. et Renard M.
Junctions Josephson a barriere semiconductrice
Rev. Phys. Appl, 6, 547 (1971)

[82] Cardinne P. Manhes B. and Renard M.
Josephson and Giaever effects with a semiconducting barrier
Proc. Appl, Supercond. Conf., Anapolis, Maryland (1972)

[83] Turner M.J. and Rhoderick E.
Metal-silicon Schottky barriers
S.S.Electron. 11, 291 (1968)

[84] Walker W.C. and Lambert E.Y.
Ohmic and rectifying contacts to semiconducting CdS crystals
J. Appl, Phys. 28, 635 (1957)

[85] Lum W.Y. and Van Duzer T.
Switching measurements on semiconductor-barrier Josephson junctions, isolated and in memoru loop
J. Appl. Phys. 48, 1693 April 1977

[86] Lum W.Y., Chan H.W. and Van Duzer T.
Memory and logic circuits using semiconductor-barrier Josephson junctions
IEEE Trans. Mag. MAG - 13, 48 January 1977

[87] Rowell N.L. and Smith J.J.T.
Investigation of the superconducting proximity effect by Josephson tunneling
Can.J. Phys. 54, 223 (1976)

[88] Greenspoon S. and Smith H.J.T.
Study of the superconducting proximity effects by Josephson tunneling
Can. J. Phys. 49, 1350 (1971)

[89] Clarke J., Freake S.M., Rappaport M.L. and Thorp T.L.
A new experimental technique for determining the BCS interaction parameter in normal metals
Sol. State Commun. 11, 683 (1972)

[90] Andreev A.F.
The thermal conductivity of the intermediate state in superconductors.
Sov. Phys, JETP 19, 1228 (1964)

[91] Cohen M.L.
Superconductivity in many-valley semiconductors and in semimetals.
Phys. Rev. 134, A 511 (1964)

[92] Smith J.L. and Stiles P.J.
Superconducting energy gap in semiconducting GeTe
J. Low Temp. Phys. 26, 101 (1977)

[93] Hein R.A., Gibson J.W., Fralge R.L.Jr., Mazelsky R., Miller R.C. and Hulm J.K.
Superconducting properties of germanium telluride
J. Phys. Soc. Japan 21, 643 (1966)

[94] Hein R.A., Gibson J.W., Mazelsky R., Miller R.C. and Hulm J.K.
Superconductivity in germanium telluride
Phys. Rev. Lett. 12, 320 (1964)

[95] Bahl S.K. and Chopra K.L.
Amorphous versus crystalline GeTe films. III. Electrical properties and band structure
J. Appl, Phys, 41, 2196 (1970)

[96] Toxen A.M., Burns M.J. and Quinn D.J.
Superconducting and normal state properties of dilute indium-tin alloys: Bulk and thin film
Phys. Rev. 138, A 1145 (1965)

[97] Cody G.D. and Miller R.E.
Magnetic transitions of superconducting thin films and foils. II. Tin.
Phys. Rev. 173, 481 (1968)

[98] Kahan G.J., Delano R.B. Jr., Brennemanm A.E. and Tsui R.T.C.
Superconducting thin films of low residual resistivity
IBM J. Res. Dev. 4, 173 (1960)

[99] Howe H.
"Stripline Circuit Design", p. 204

[100] Chang C.C. and Holdeman L.B.
private communication

[101] McMillan W.L. and Rowell J.M.
Tunneling and strong-coupling superconducting
in "Superconductivity" edited by Parks R.D., 1, 561 (1969)

[102] Giaever I.
Metal-insulator-metal tunneling
in "Tunneling phenomena in solids" edited by Burstein E. and
Lundquist, Plenum Press, N.Y. (1969), Chapter 3

FIGURE CAPTIONS

Fig. 3.1 S-$\emptyset_B$-S model for junction with a/an
a) insulator of $\emptyset_B \sim 1$ eV
b) p-type semiconductor of $\emptyset_B \sim 10^{1-2}$ meV
c) n-type semiconductor of $\emptyset_B \sim 10^{1-2}$ meV.

Fig. 3.2 S-N-S model for proximity junction with metal or semimetal.

Fig. 3.3 S-$\emptyset_B$-N-S model for photosensitive tunnel junction with conductivity storage effect
a) in the dark
b) after illumination.

Fig. 3.4 S-$\emptyset_B$-N-$\emptyset_B$-S model for junction with degenerative semiconductor barrier
a) with N region dominating
b) with $\emptyset_B$ region dominating.

Fig. 3.5 S-N-$\emptyset_B$-N-S model for S-S'-S junction with a high electron affinity semiconductor as the barrier.

Fig. 4.1 Andrew scattering for N-S interface in half of an S-N-S junction.

Fig. 5.1 Cryogenic system.

Fig. 5.2 Mask and substrate arrangements inside the coating unit.

Fig. 5.3 Rotatable mask holder with 4 mounting positions for masks.

Fig. 5.4 Method for upside-down substrate and mask fitting and alignment.

Fig. 5.5 Temperature control and measurement for substrate. The mask mount is thermally insulated from the mask holder by Teflon slices.

Fig. 5.6 Evaporated metal film with
a) smooth surface
b) irregular surface.

Fig. 5.7 dc measuring system.

Fig. 5.8 a) Stripline box with top cover removing showing the junctions and the microstripline circuit
b) 2 cross-type junctions, each coupled to an external resonator in the MIC, but only the coupling ends of the resonators are inside the photograph.

Fig. 5.9 Stripline box cross-section viewed from the side with substrate etc. displaced outside.

Fig. 5.10 Method for microwave cable connections and dc leads with adjustable sample height.

a) Top cover and the composite rod only
b) Top cover and the composite rod fitted to dewar, showing also the external connections.

Fig. 5.11 Elliptical function low pass filter

a) Prototype
b) Realisation in microstrip form
c) filter characteristics.

Fig. 6.1 $Pb_{0.9}In_{0.1}$-GeTe-$Pb_{0.9}In_{0.1}$ junction (P14.1)
Pinhole oxidation condition:
105°C in air for 1 hour
I-V and $-\frac{dI}{dV}$ showing quasiparticle tunneling with 2Δ and phonon spectrum of the strong-coupling superconductor electrodes.

Fig. 6.2 Imperfect $Pb_{0.9}In_{0.1}$-GeTe-$Pb_{0.9}In_{0.1}$ junction (P21.1) with SLUG type $I_c(H)$

a) I-V characteristics at low power level
b) I-V and $-\frac{dV}{dI}$ at higher power level, showing subharmonic structures. The $\frac{2\Delta}{n}$ energies are also marked at the expected energies for n = 1 to 5
c) R(T) vs T at $I \simeq 0$.

Fig. 6.3 a) 4 probe resistivity measurement for crystallisation monitoring and for interdiffusion measurement
b) Cross-type junctions and dc connections.

Fig. 6.4 Pb-GeTe-Pb junction (P56.1) with a small crystallised spot for the semiconductor.

a) Critical Josephson current vs B field applied parallel to junction surface.
Inscription: Rectangular barrier supercurrent density distribution

b) $I_J(T)$ for $T \lesssim T_c$
Inscription: I-V characteristic at the indicated conditions.

Fig. 6.5 Evaporation steps for the MIC junctions

a) Base Pb electrode evaporated
b) GeTe evaporated
c) Electrode film with resonators evaporated last to improve rf coupling. Scratch is made to complete the upper resonator and to dc isolate the microwave source.

Fig. 6.6 DC properties of a Pb-GeTe-Pb junction (C6U) with GeTe crystallised by laser at a tiny spot.
(a) Critical current vs transversely applied magnetic field.
(b) I-V characteristics showing assymmetry due to potential regions at S-S' interface.
(c) I-V characteristics at an $I_J(H)$ minimum.

Fig. 6.7 AC properties of the same junction in fig. 6.6
(a) Microwave induced steps
(b) Constant voltage step amplitude vs microwave power amplitude for the 0-2 orders. They are fitted to the theoretical Bessel functions J_0, J_1, and J_2 of the respective orders.

FIG.3.1 $S-\emptyset_B-S$

FIG.3.1(a)

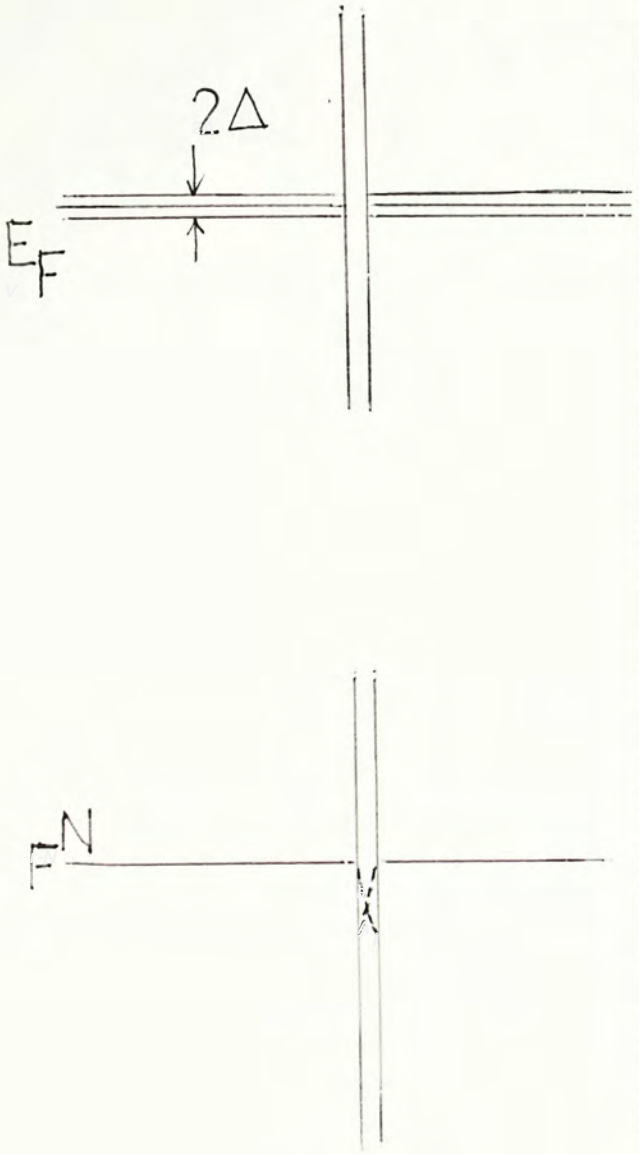

FIG.3.1(b)

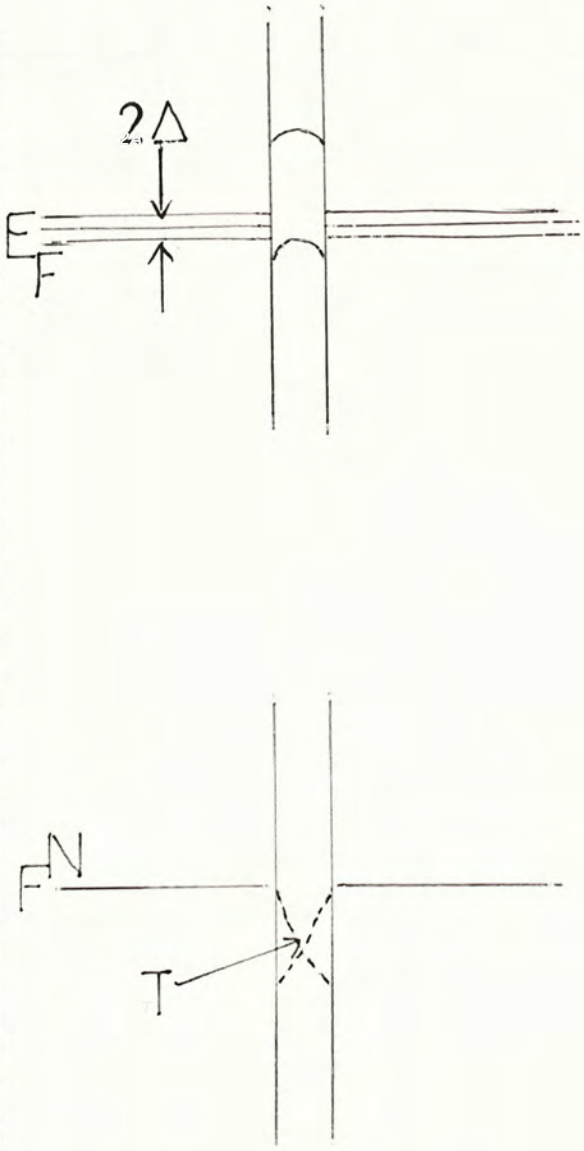

FIG.3.1(c)

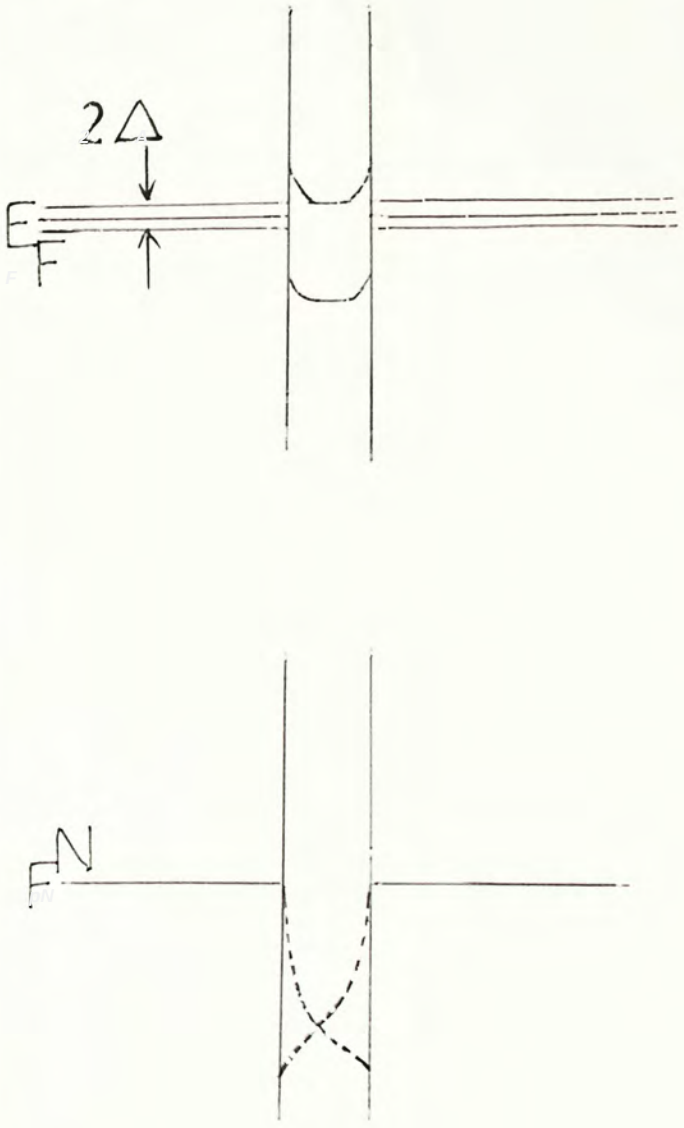

FIG. 3.2 S-N-S

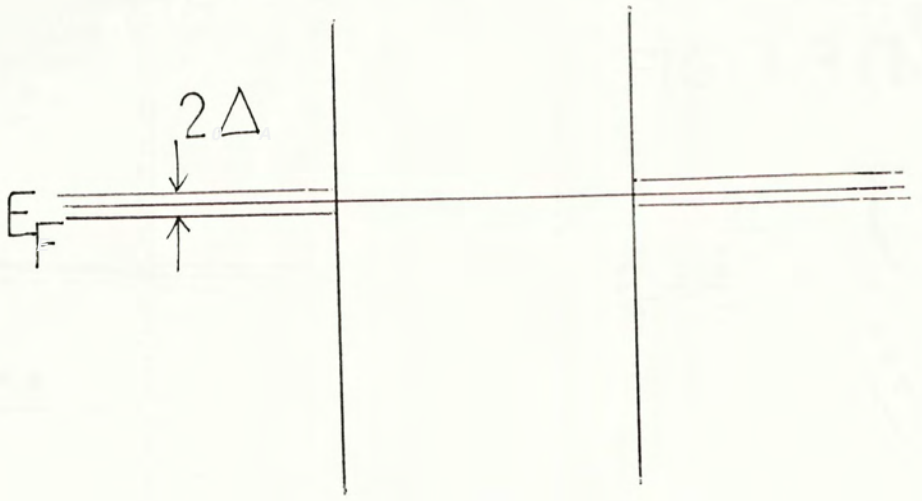

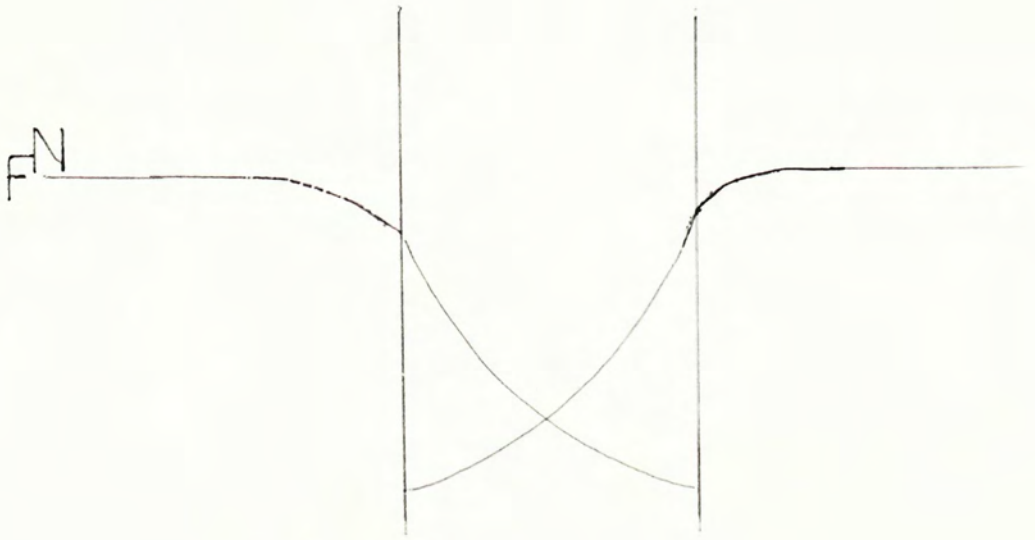

FIG.3.3 S-ϕ_B-N-S

FIG.3.3(a)

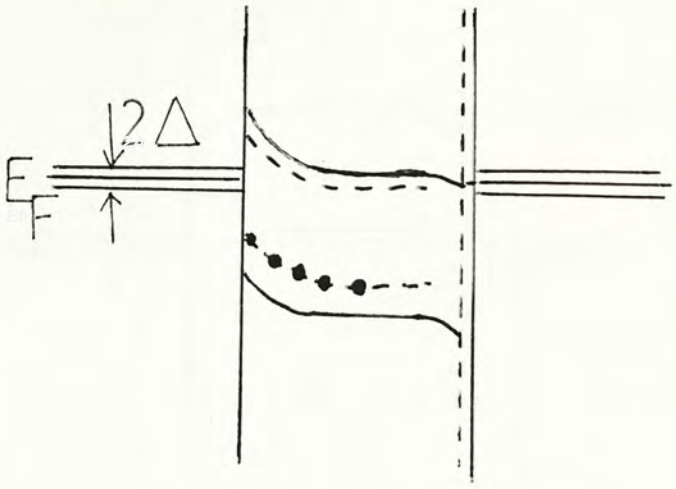

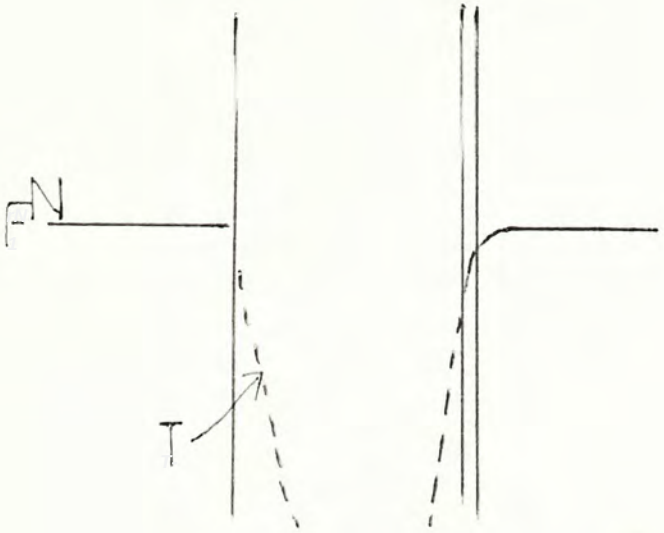

FIG. 3.3(b)

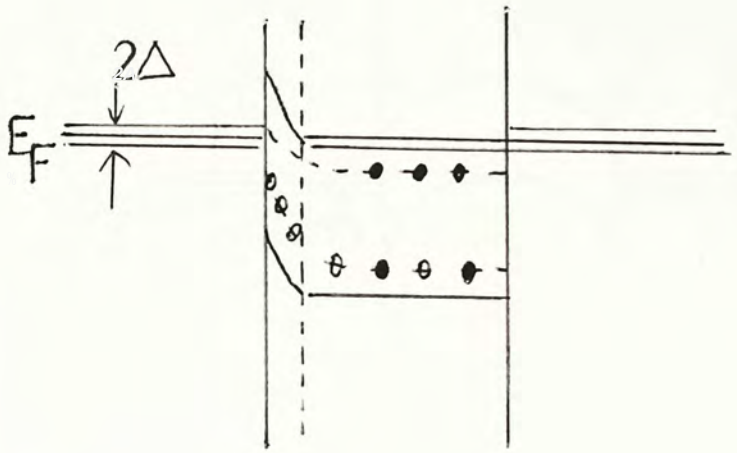

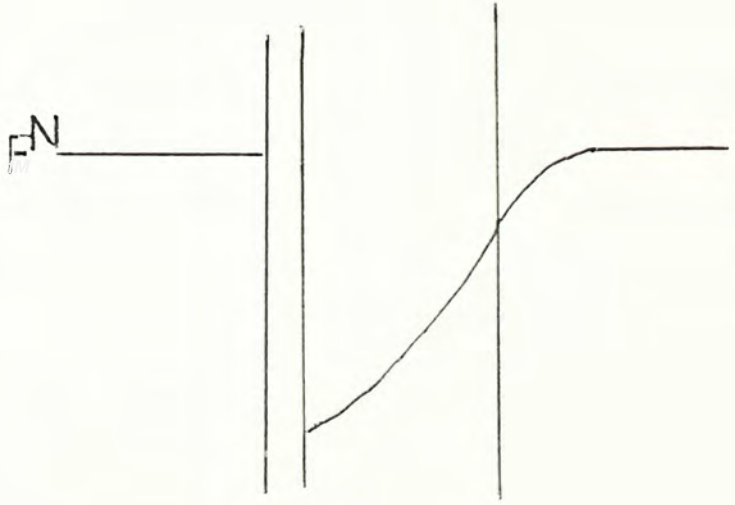

FIG. 3.4 $S-\Phi_B-N-\Phi_B-S$

FIG. 3.4 (a)

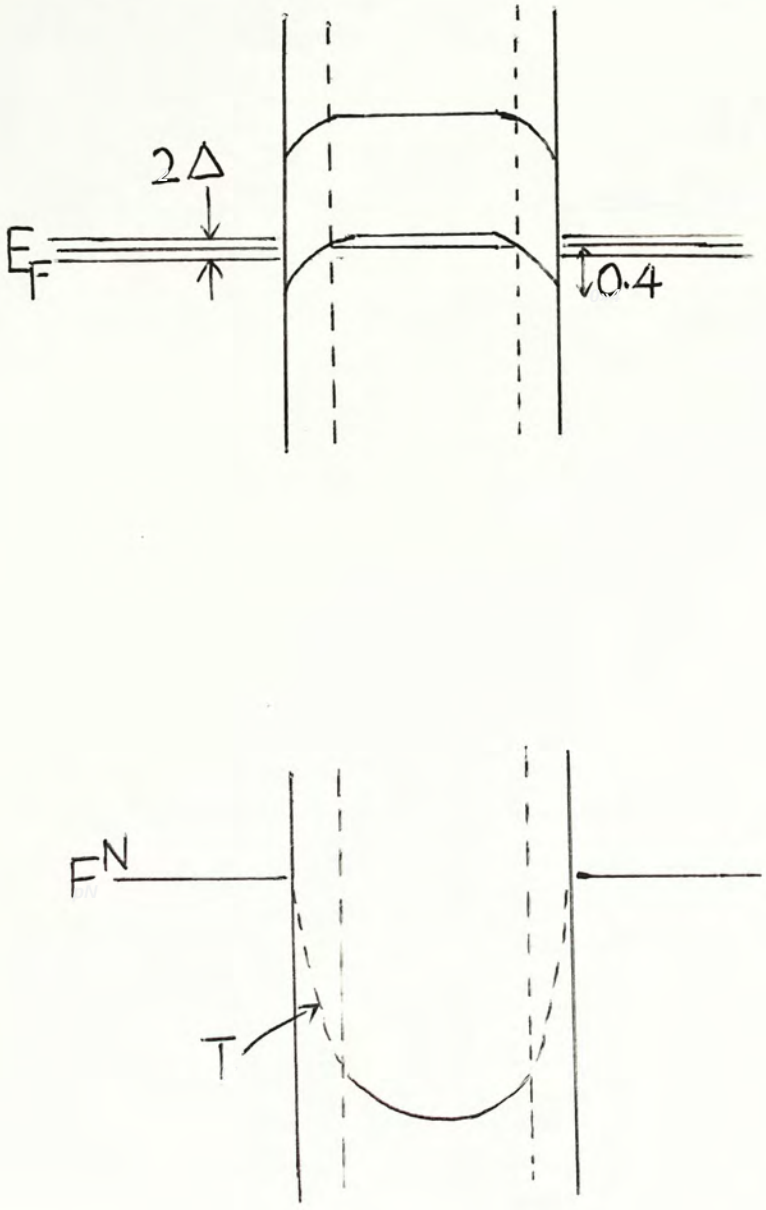

FIG. 3.4 (b)

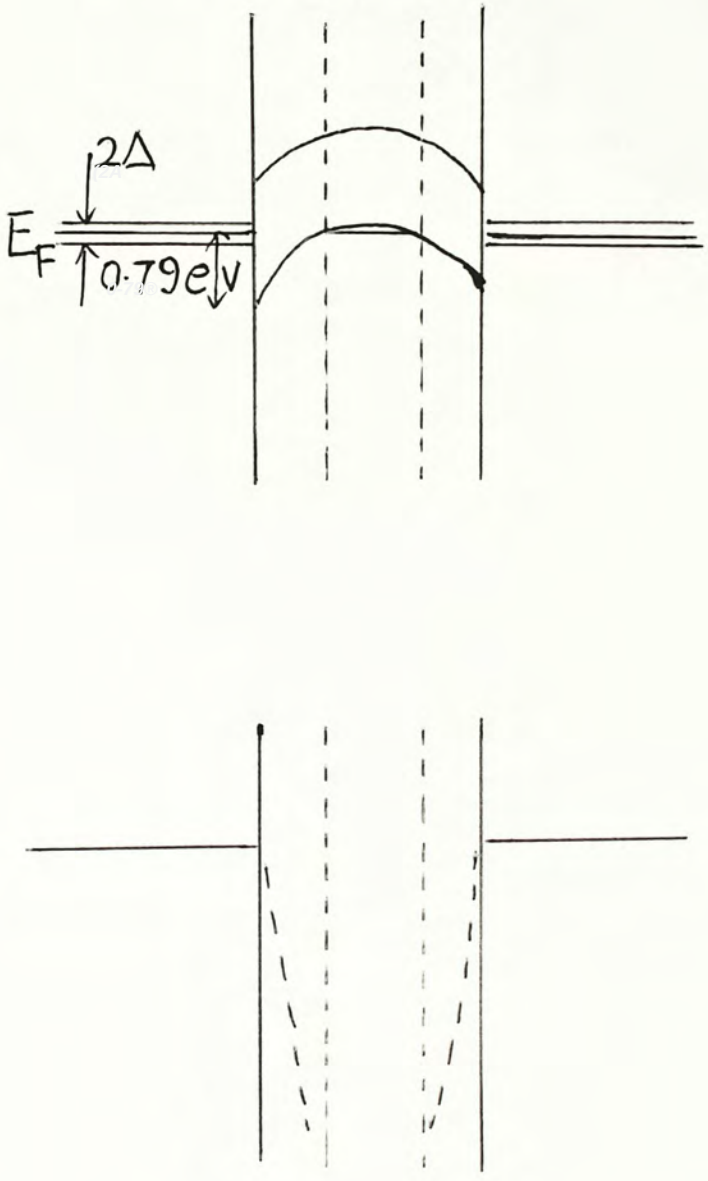

FIG. 3.5 S-N-ϕ_B-N-S

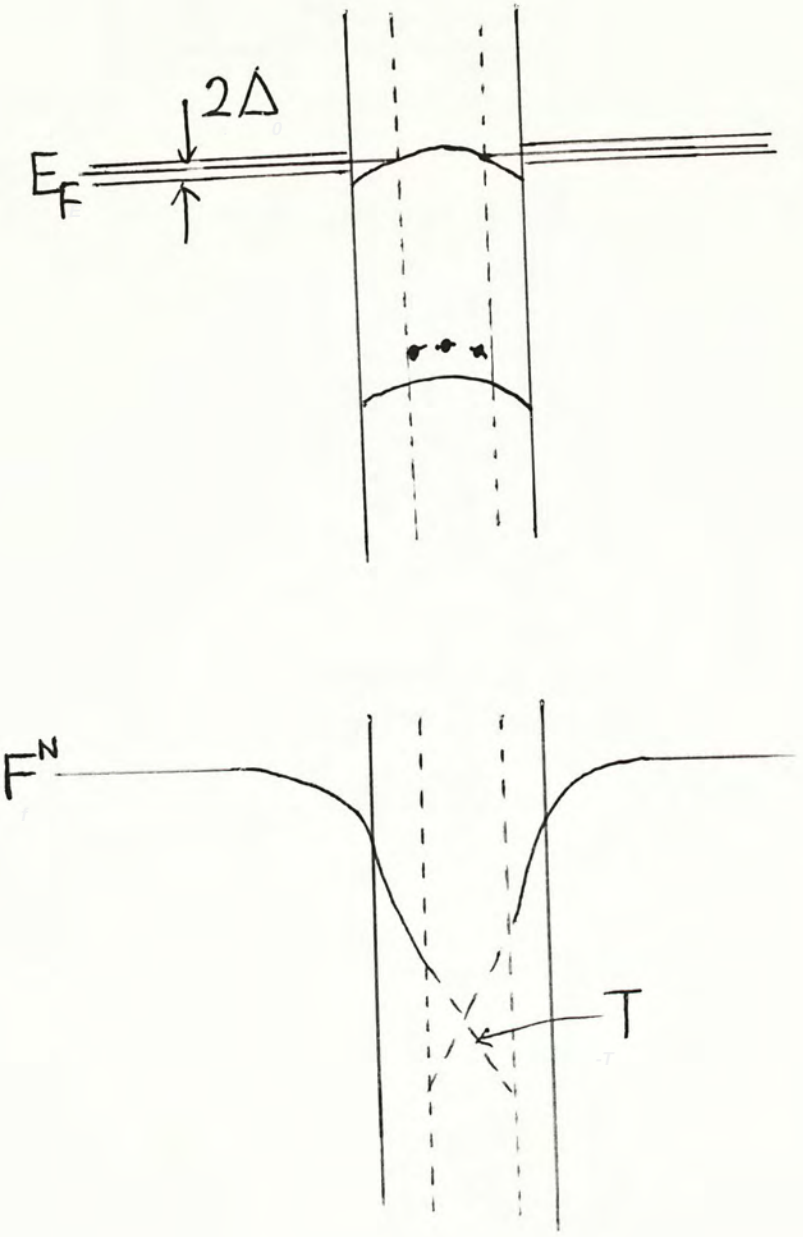

FIG. 4.1

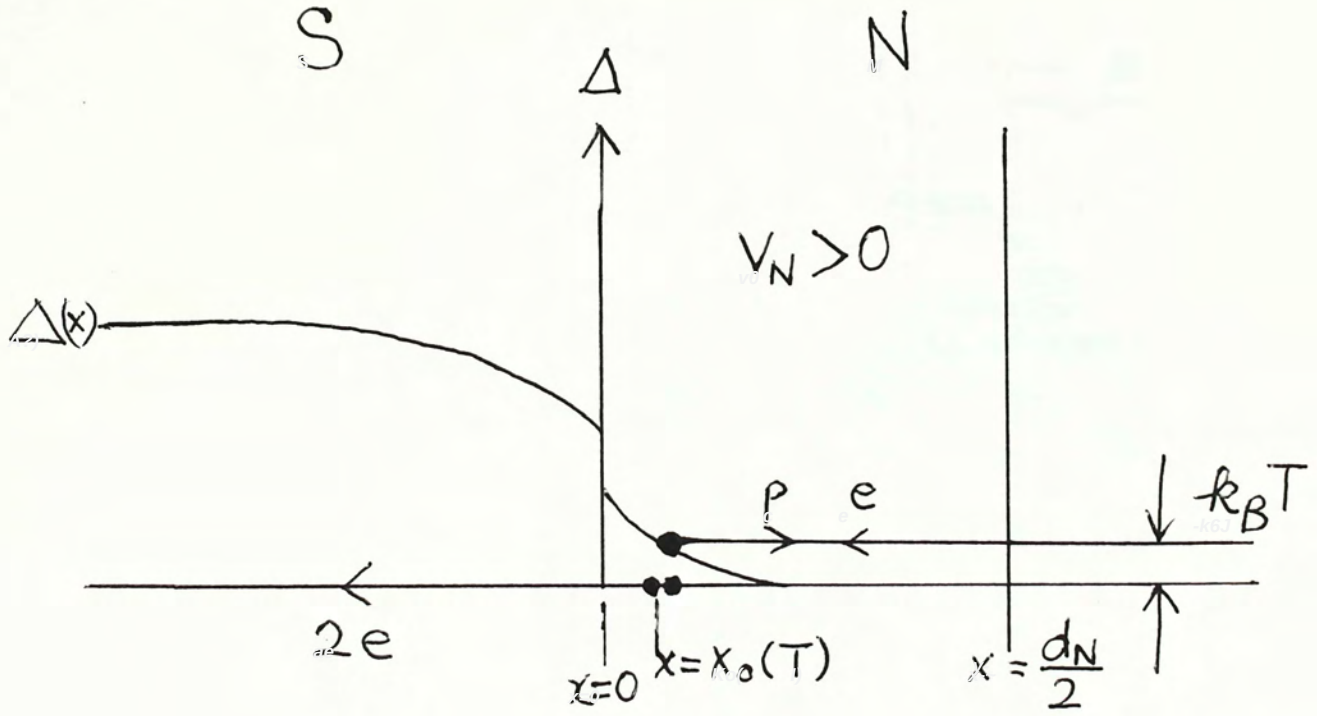

FIG. 5.1

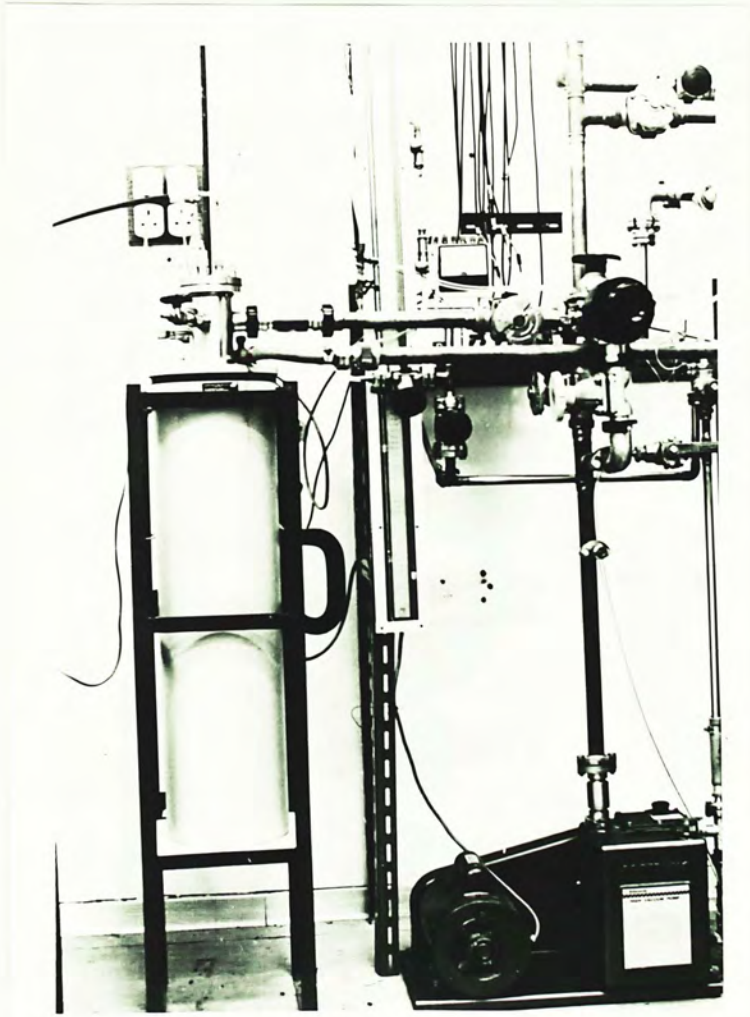

FIG. 5.2

FIG. 5.3

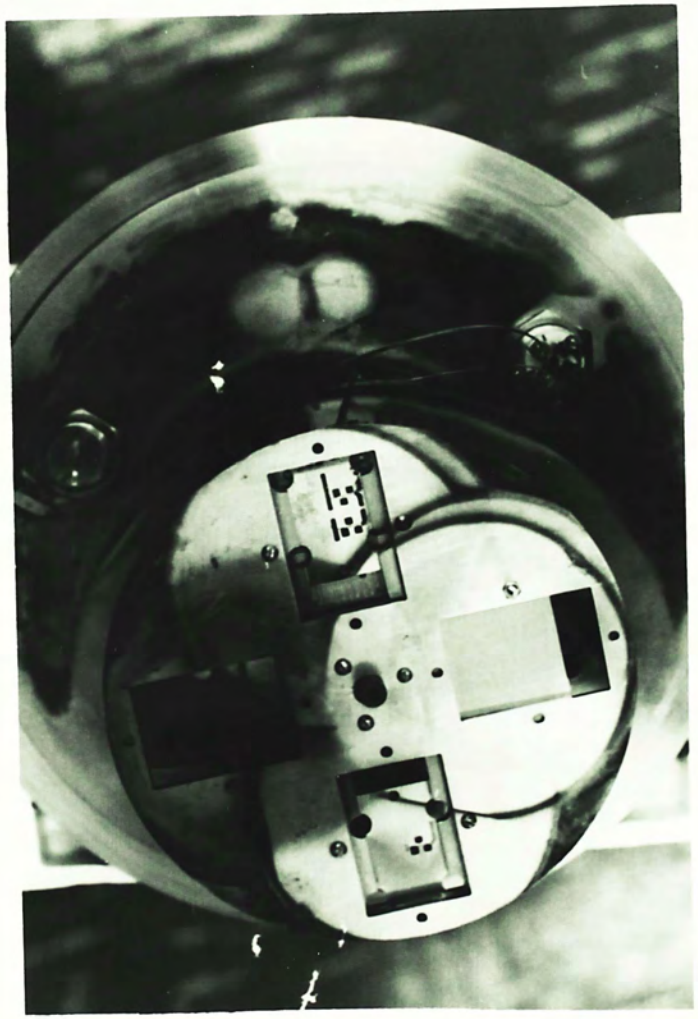

FIG. 5.4 (a)

FIG. 5.4 (b)

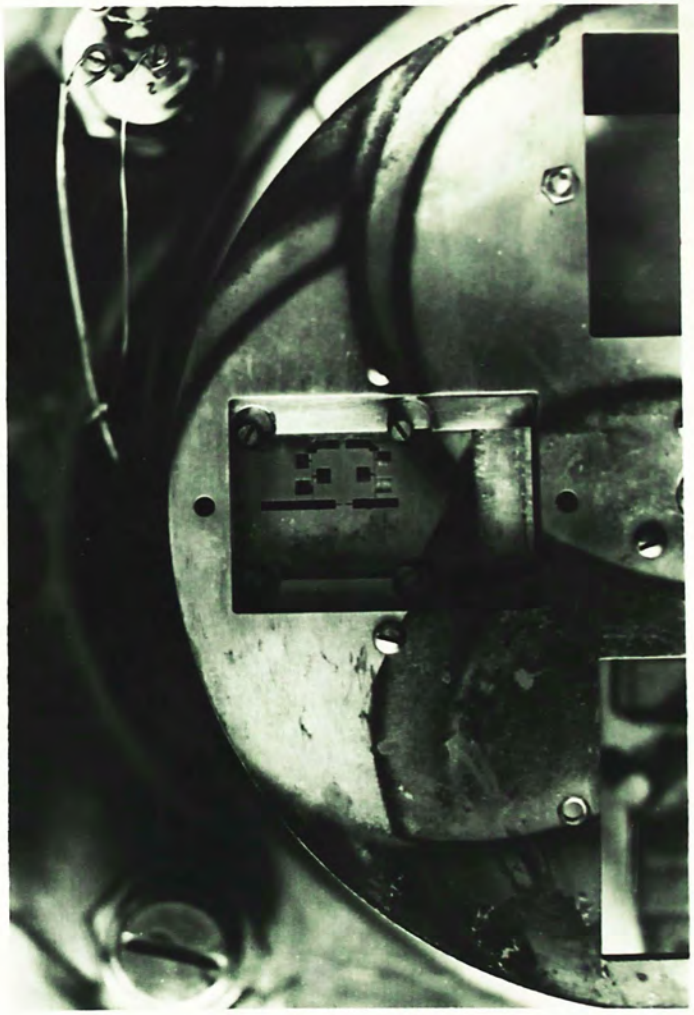

FIG. 5·5

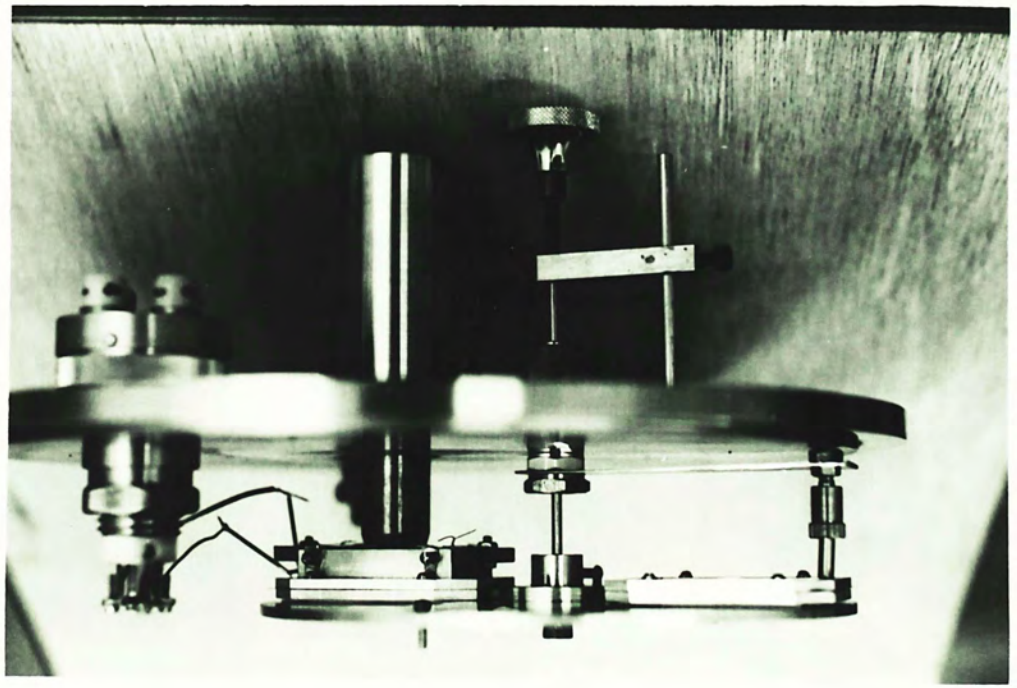

FIG. 5.6 (a)

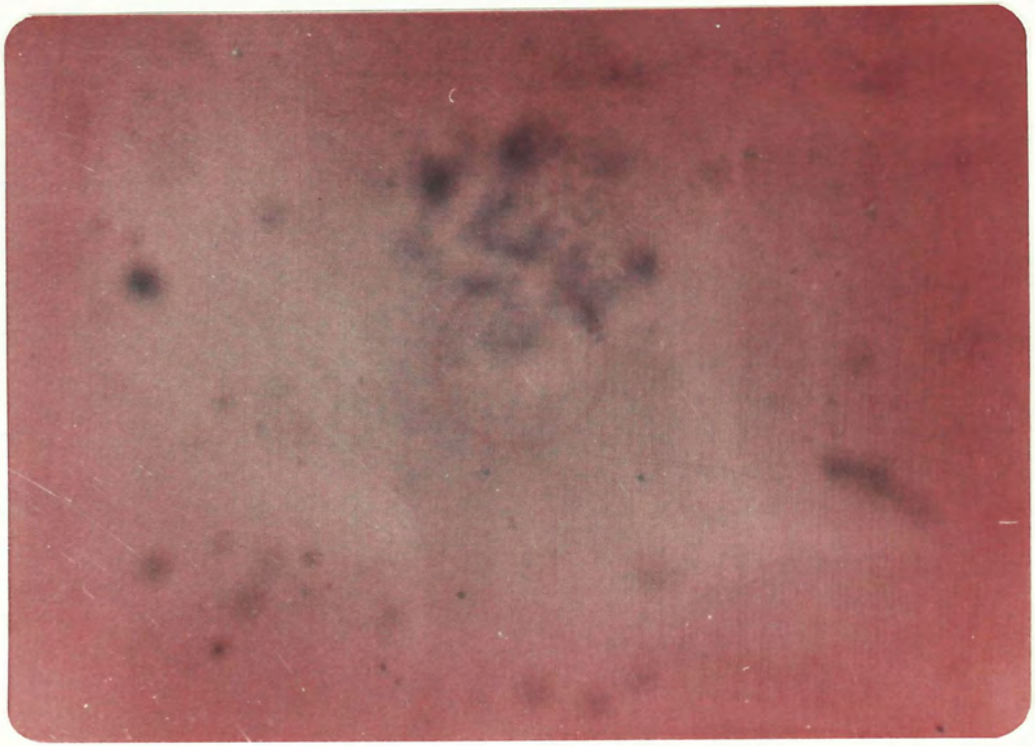

FIG. 5.6 (b)

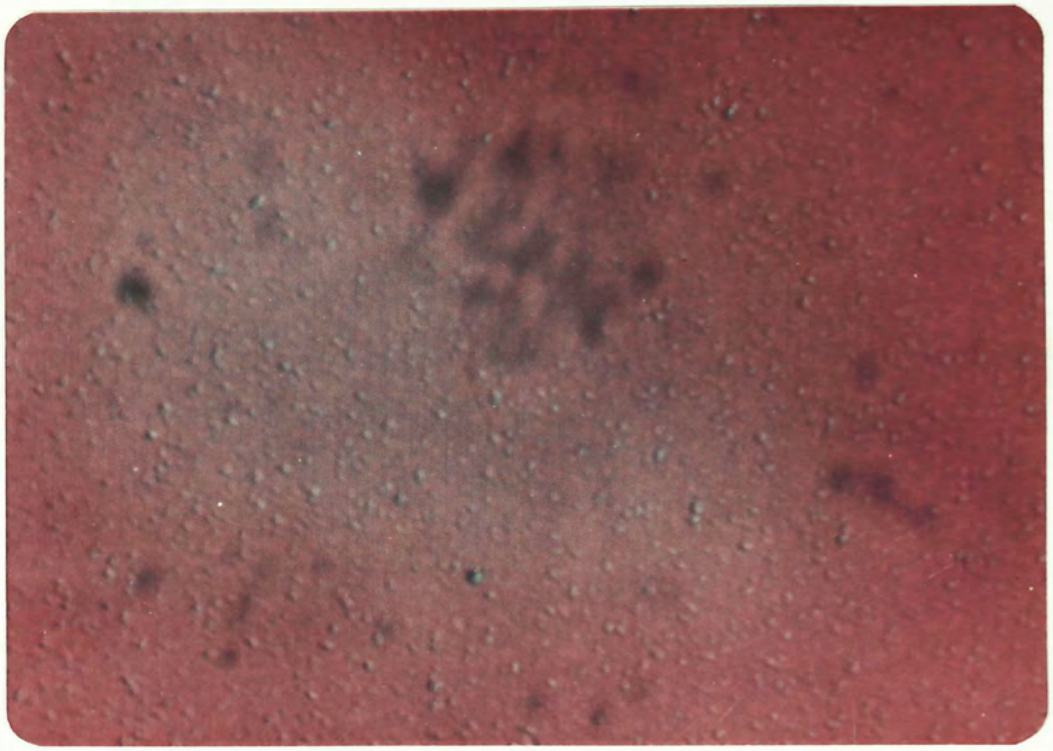

10 μm

FIG. 5.8 (a)

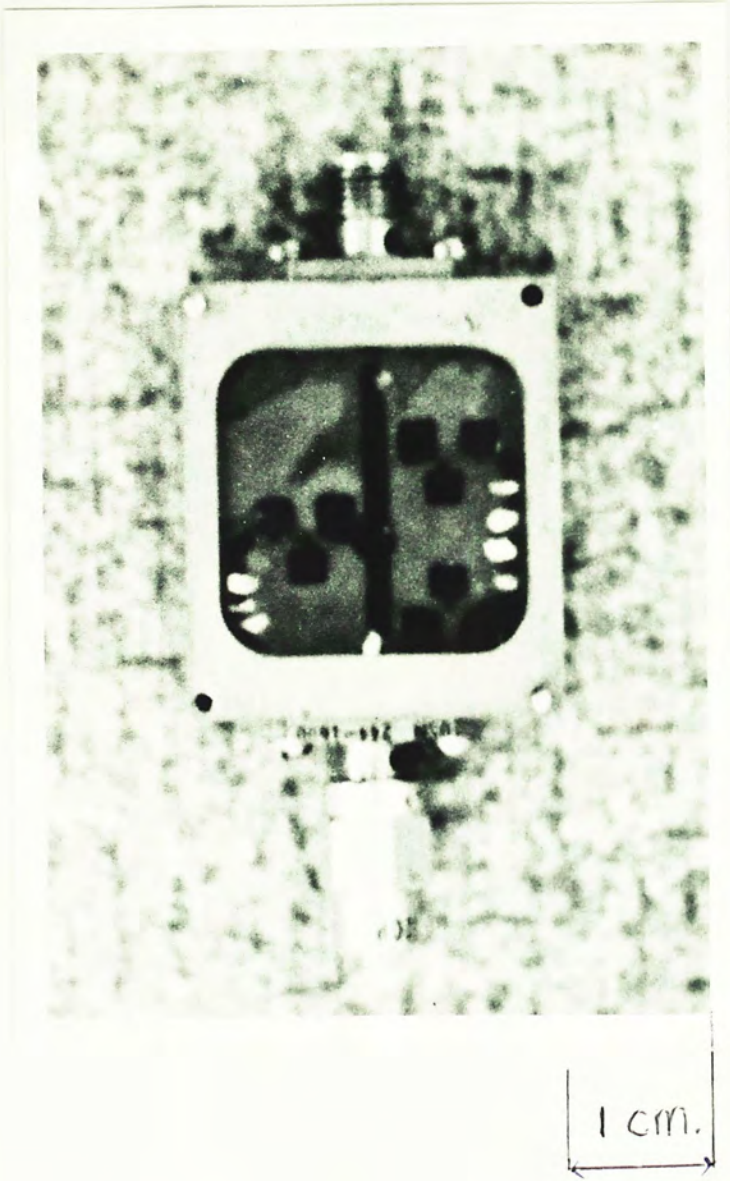

FIG. 5.8 (b)

Fig. 5.9

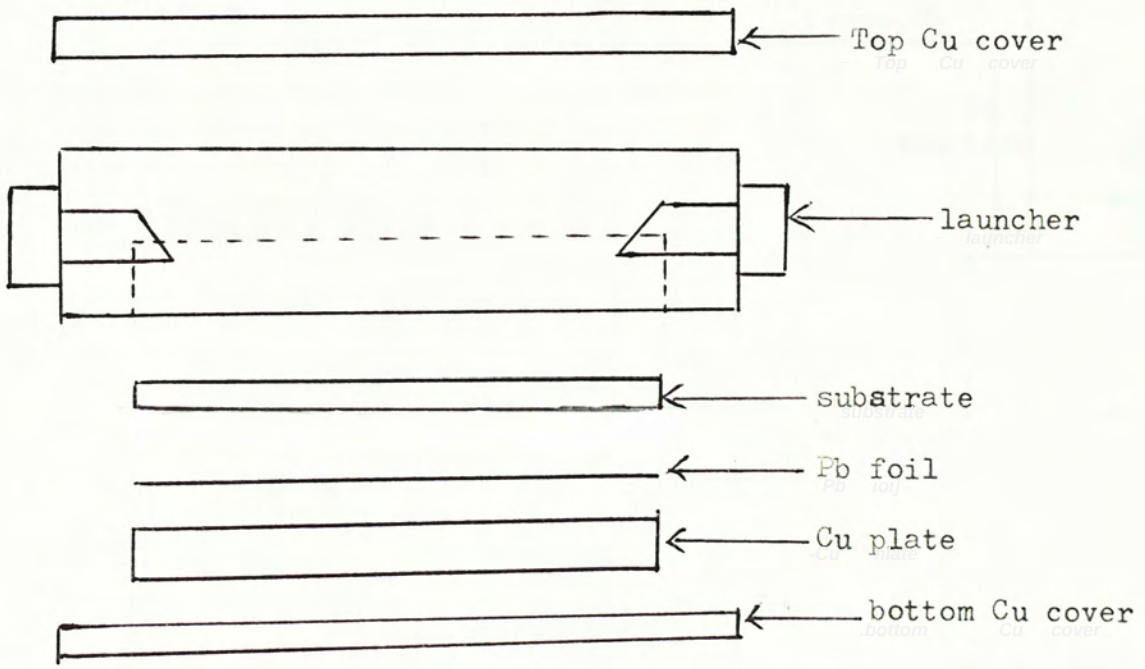
Top Cu cover
launcher
substrate
Pb foil
Cu plate
bottom Cu cover

Fig. 5.7

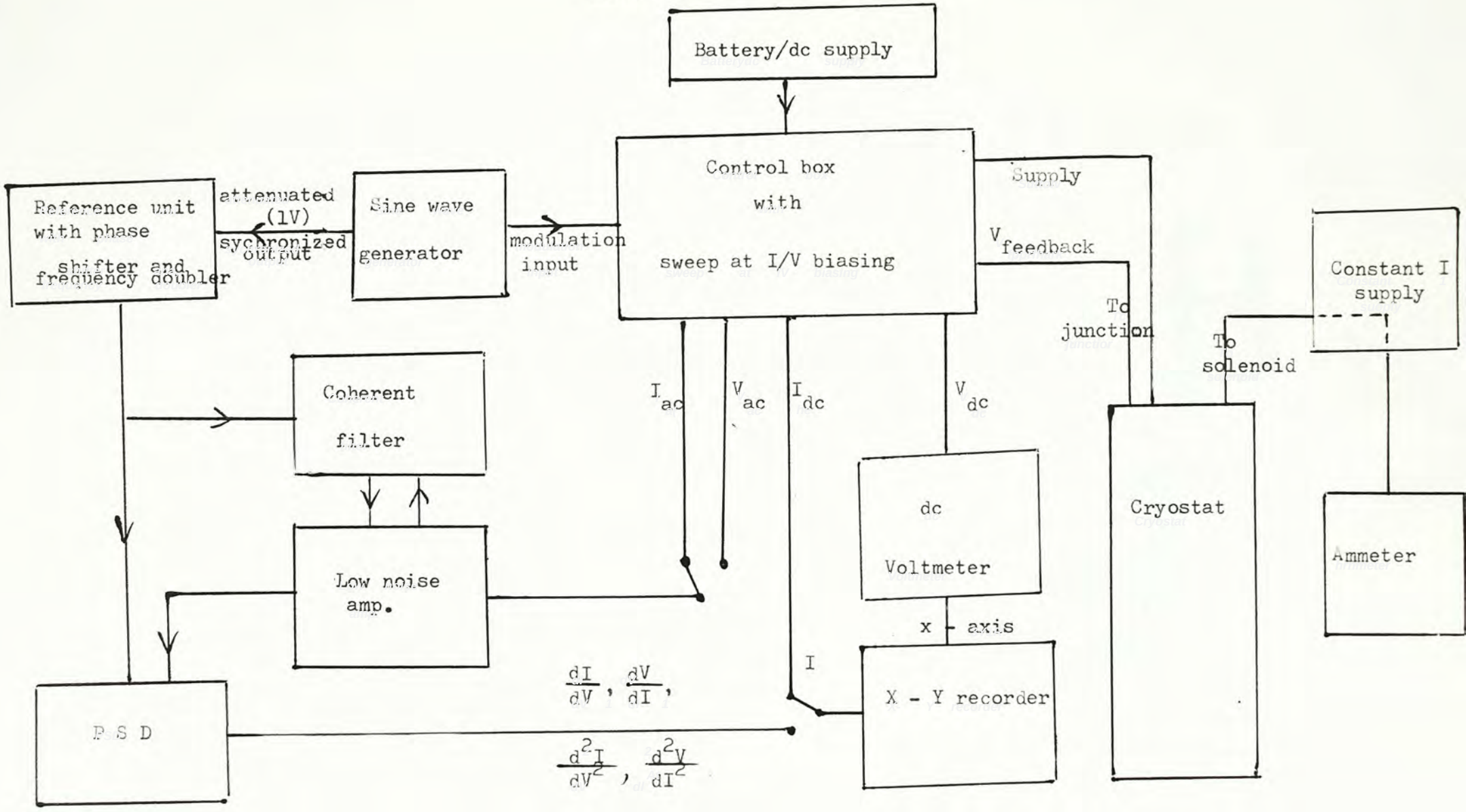
Battery/dc supply
Control box with sweep at I/V biasing
Supply
V feedback
To junction
To solenoid
Constant I supply
Reference unit with phase shifter and frequency doubler
attenuated (1V) sychronized output
Sine wave generator
modulation input
Coherent filter
Low noise amp.
I ac
V ac
I dc
V dc
dc Voltmeter
x - axis
Cryostat
Ammeter
X - Y recorder
I
dI/dV , dV/dI ,
d²I/dV² , d²V/dI²
P S D

FIG. 5.10 (a)

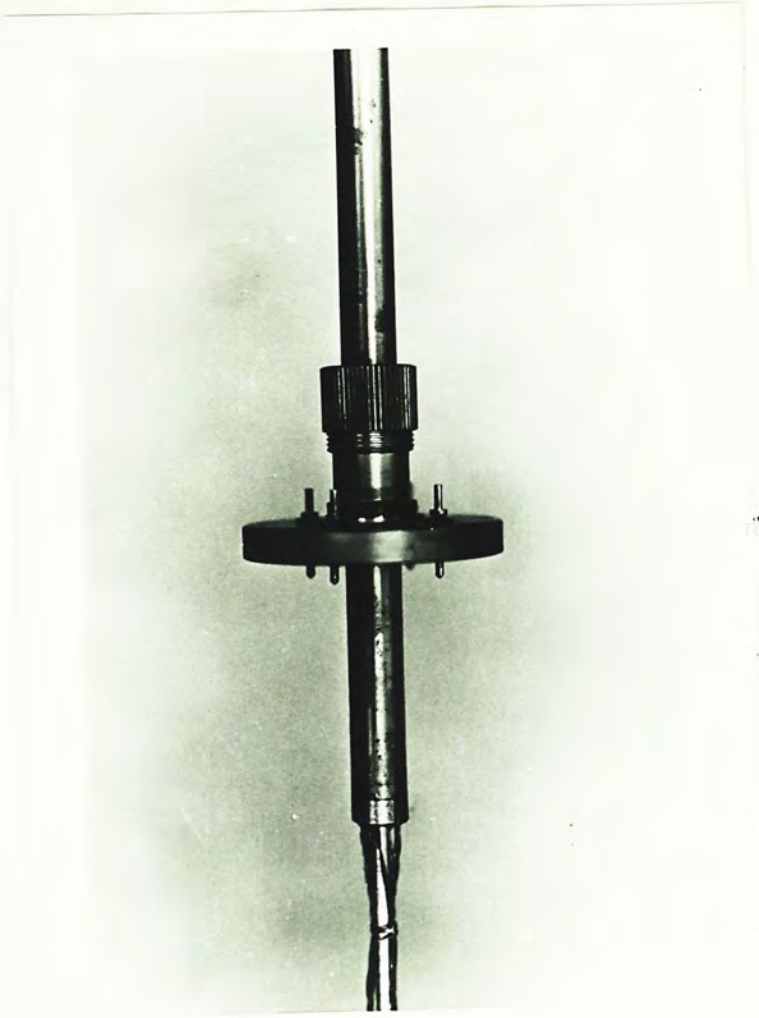

FIG. 5.10 (b)

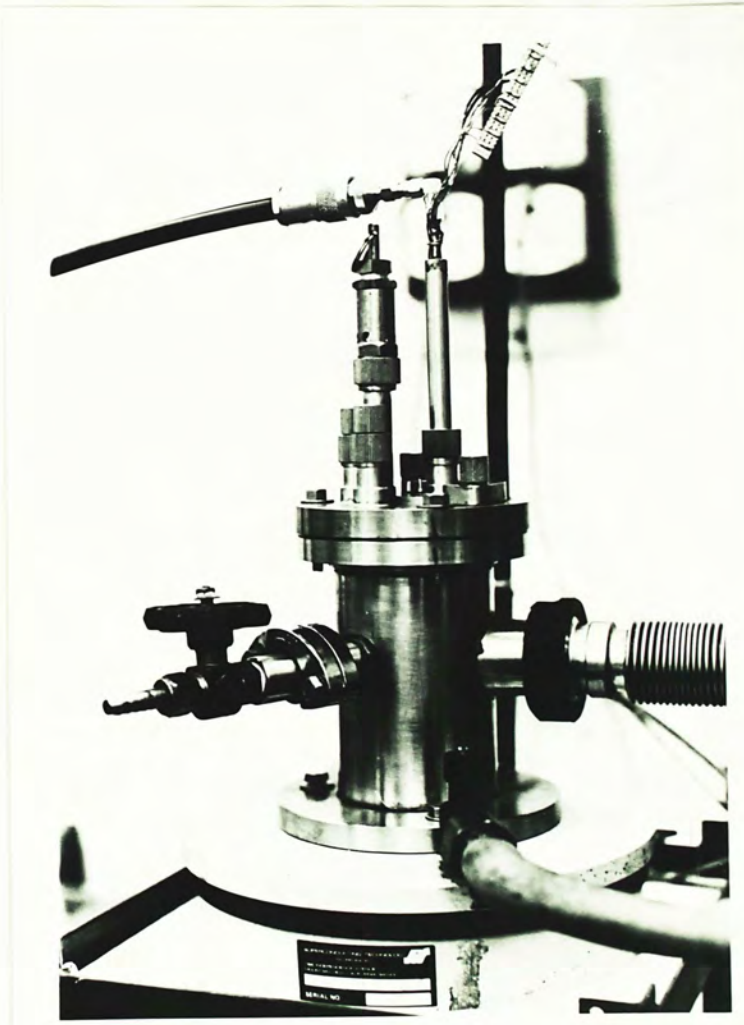

FIG. 5.11 LOW-PASS FILTER

(a)

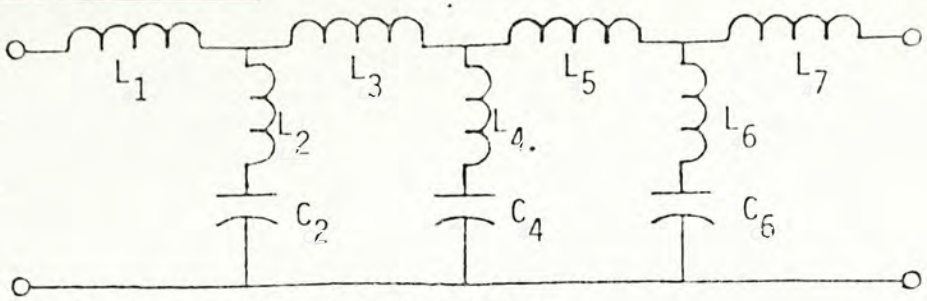

ELIPTICAL FILTER, LUMPED-ELEMENT PROTOTYPE

(b)

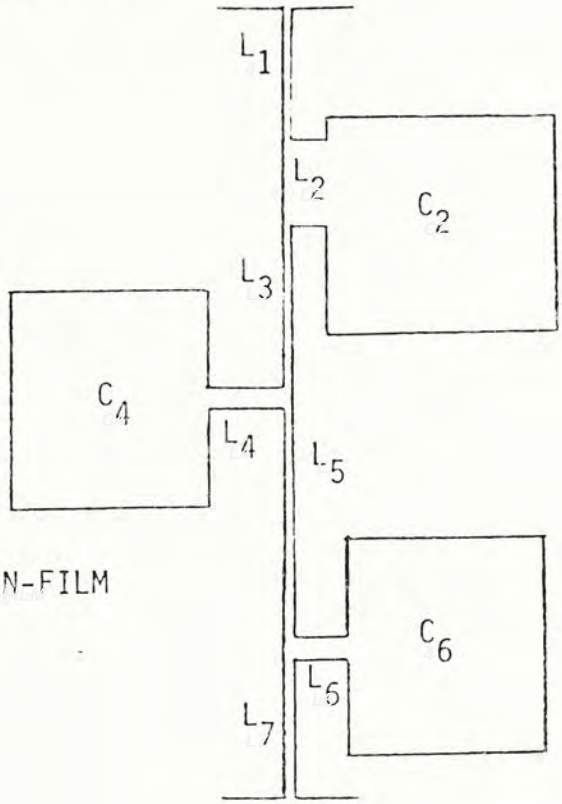

ELIPTICAL FILTER, THIN-FILM (MICROSTRIP) VERSION

(c)

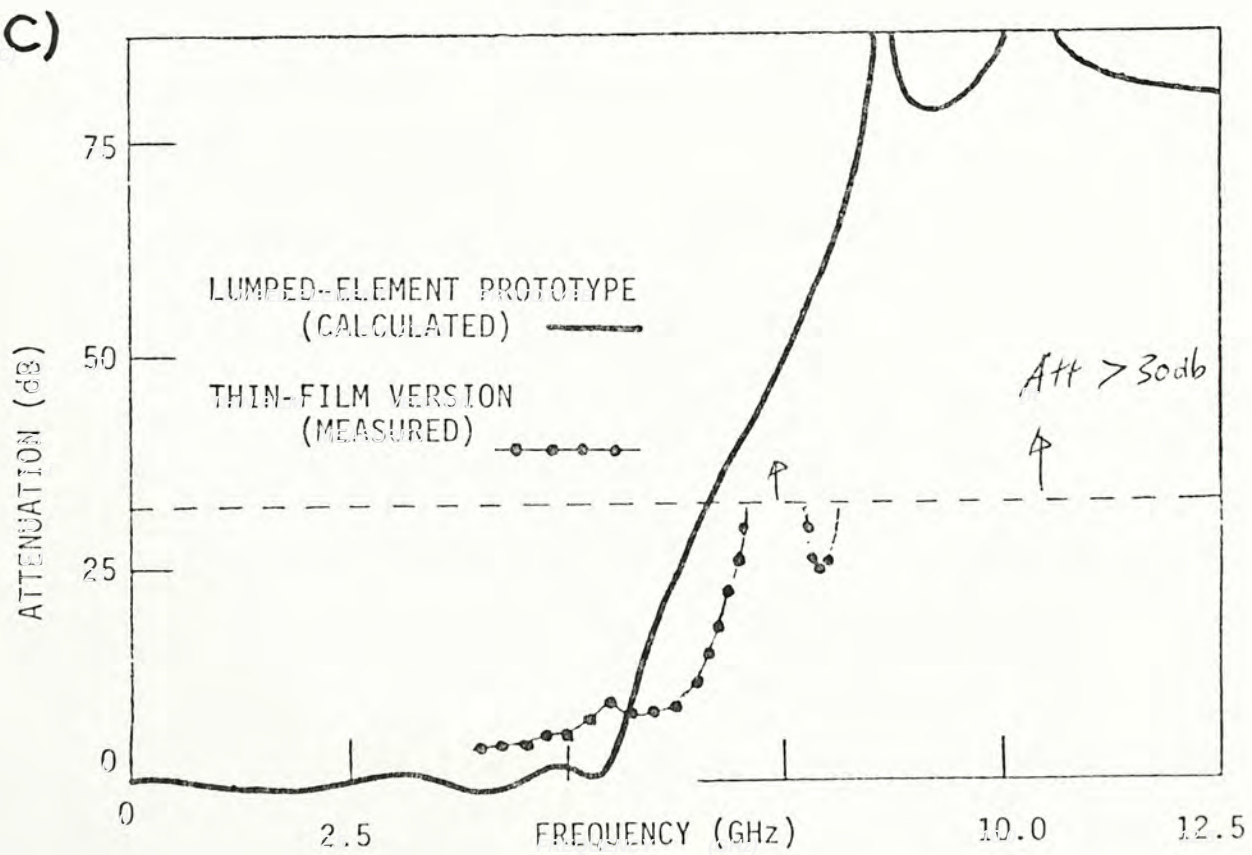

FIG. 6.1

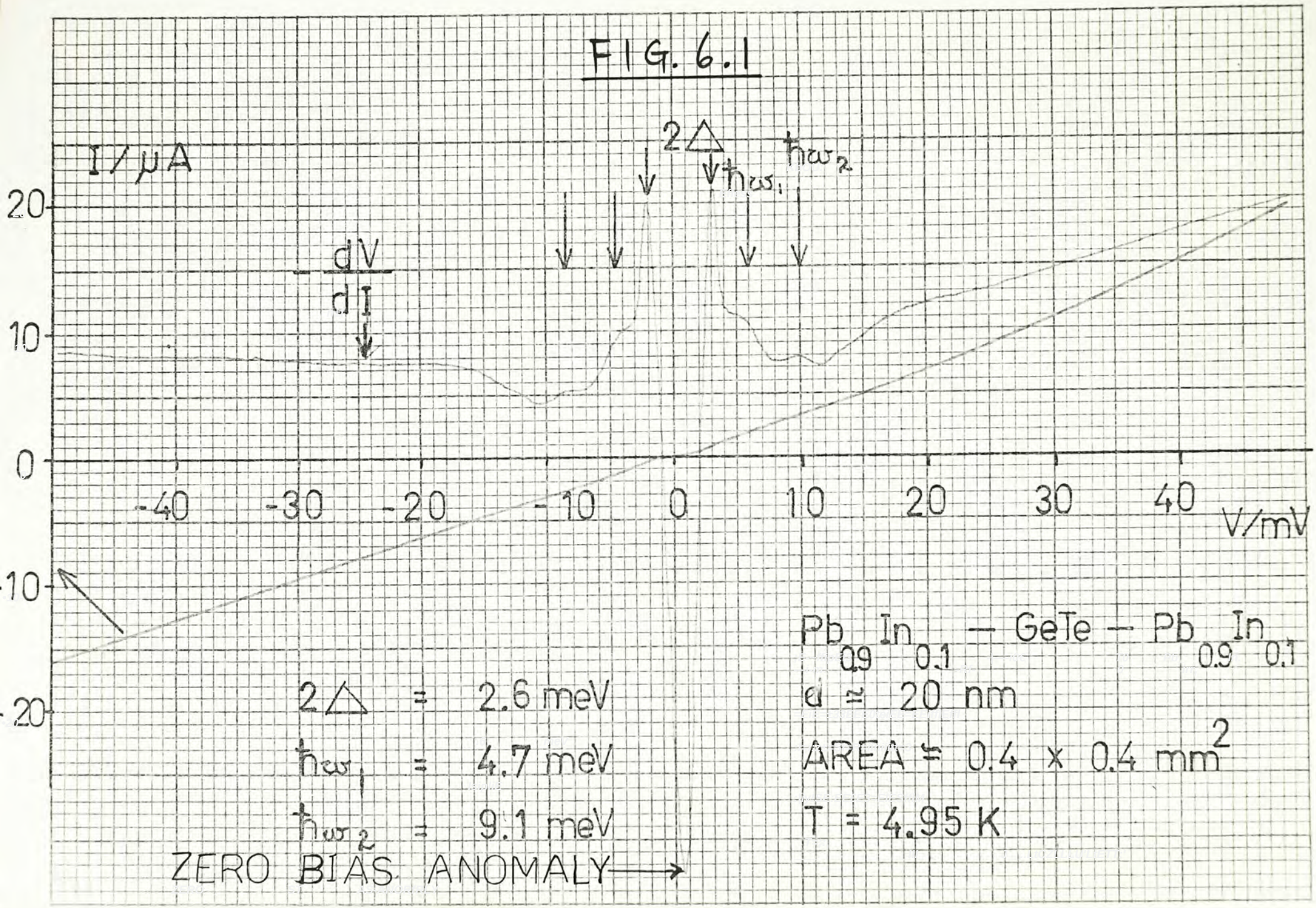
I / μA
20
10
0
-10
-20
-40
-30
-20
-10
0
10
20
30
40
V/mV
dV/dI
2Δ
ħω1
ħω2
Pb0.9In0.1 — GeTe — Pb0.9In0.1
d ≈ 20 nm
AREA ≈ 0.4 x 0.4 mm2
T = 4.95 K
2Δ = 2.6 meV
ħω1 = 4.7 meV
ħω2 = 9.1 meV
ZERO BIAS ANOMALY

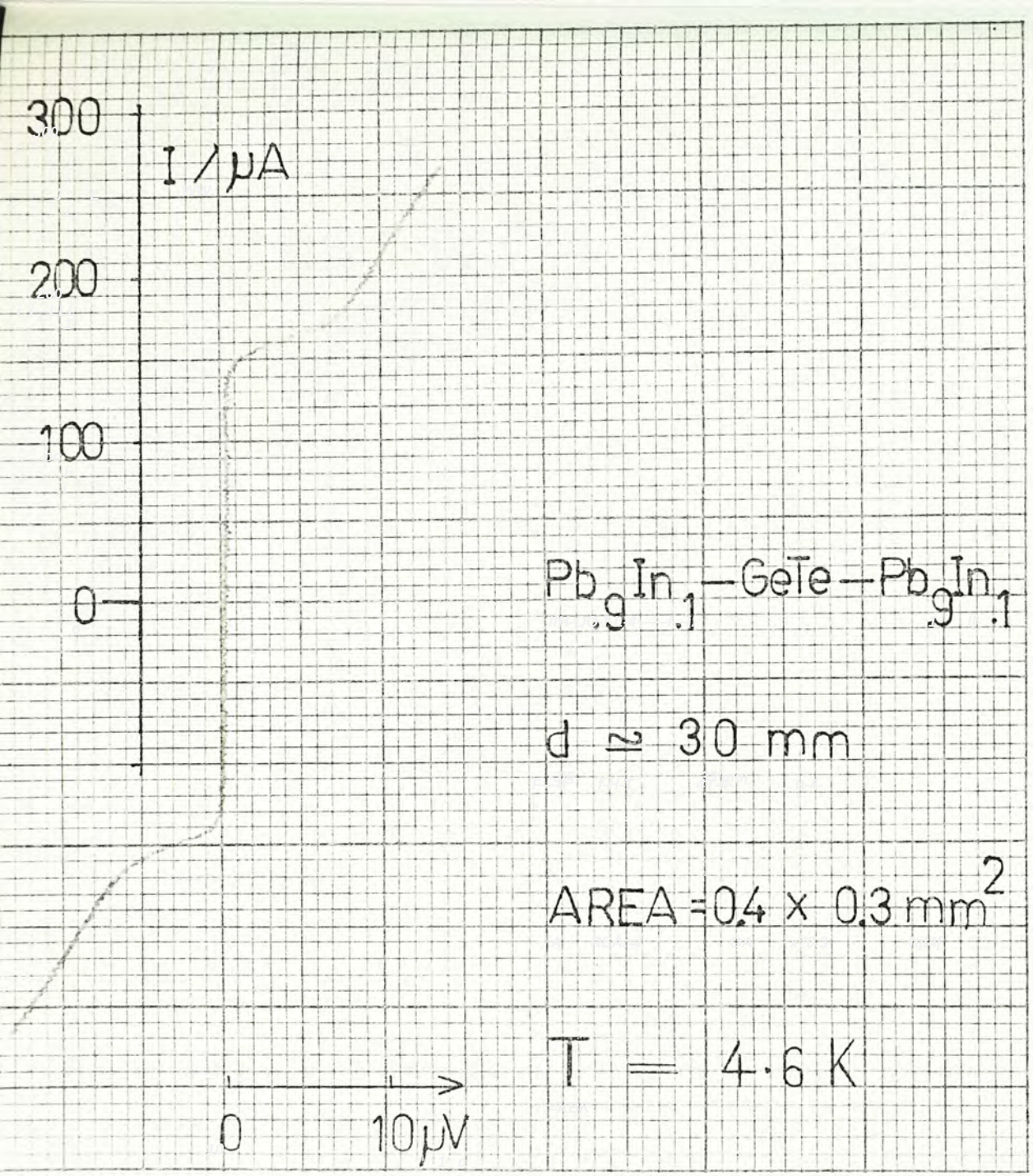

FIG 6.2a

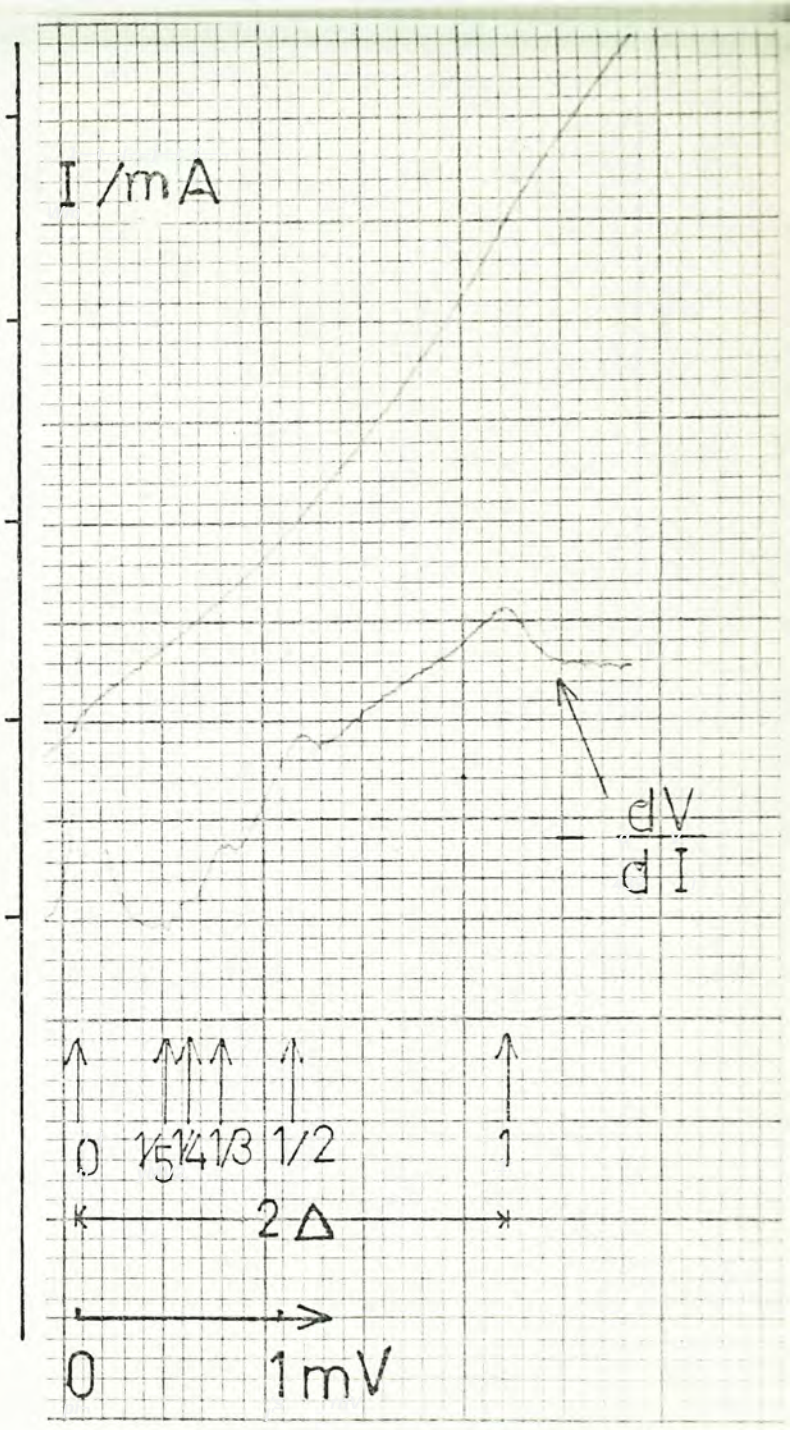

FIG. 6.2b

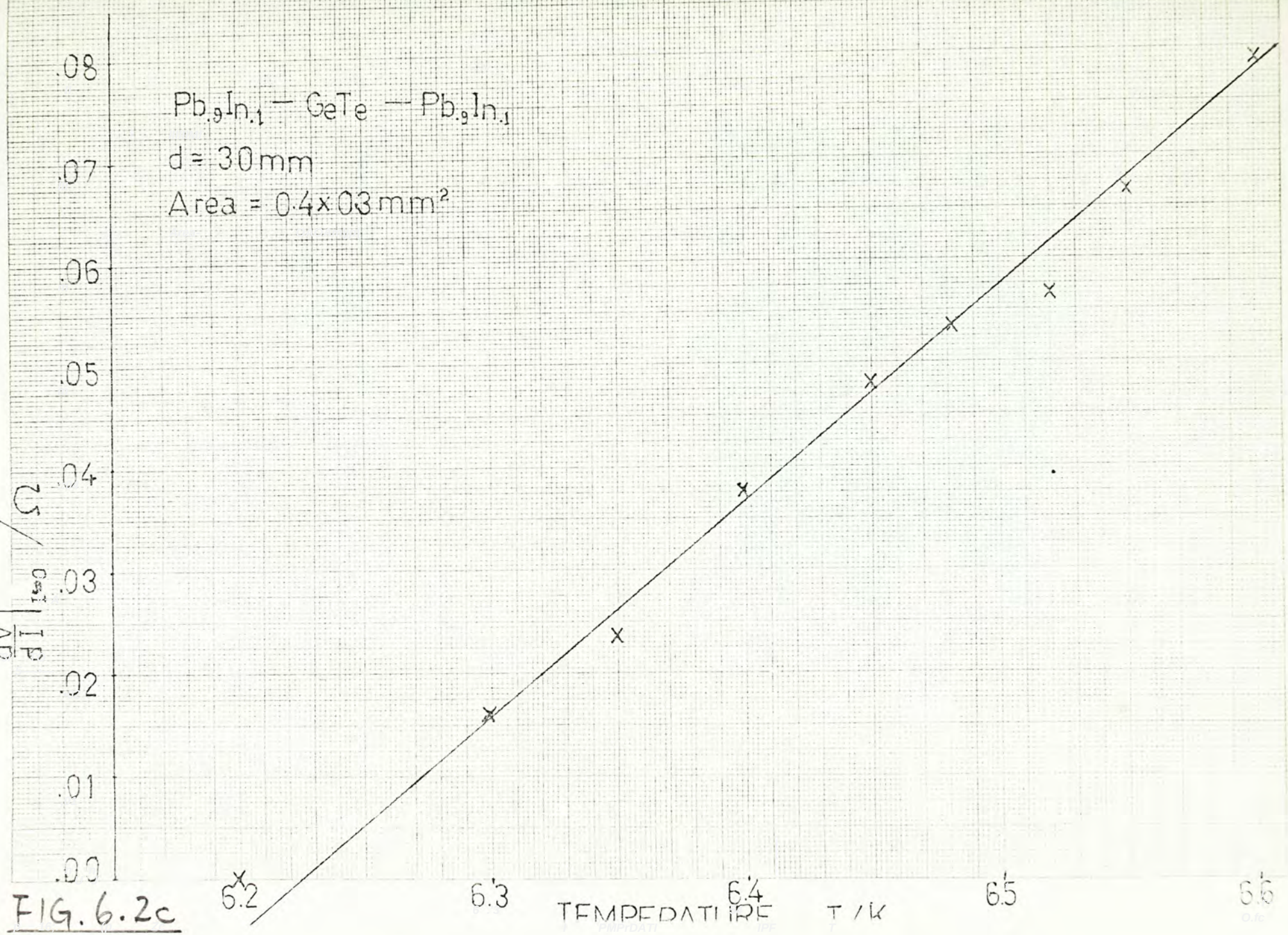
$Pb_{.9}In_{.1}$ — GeTe — $Pb_{.9}In_{.1}$
d = 3.0 mm
Area = 0.4 × 0.3 mm²
.08
.07
.06
.05
.04
.03
.02
.01
.00
$\frac{dV}{dI}\Big|_{I=0}$ / Ω
6.2
6.3
6.4
6.5
6.6
TEMPERATURE T / K

FIG. 6.2c

FIG. 6·3a

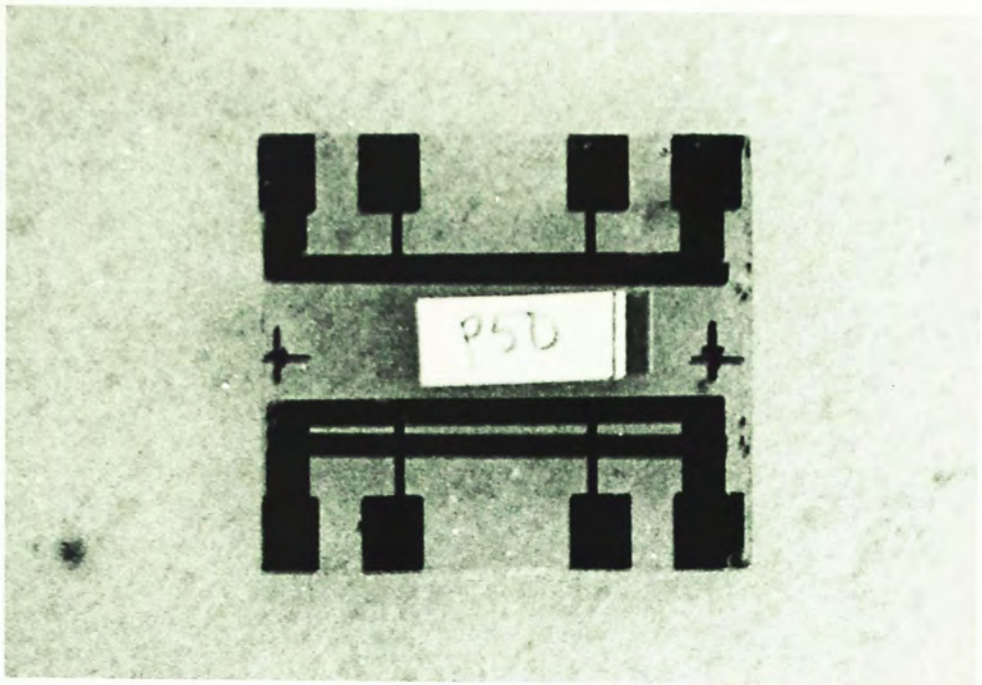

← GeTe on Pb

GeTe on glass in // with Pb

1 cm.

FIG. 6·3b

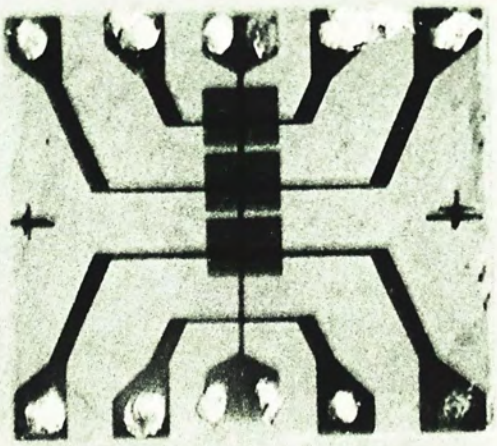

oxide junction

3 GeTe junctions

1 cm.

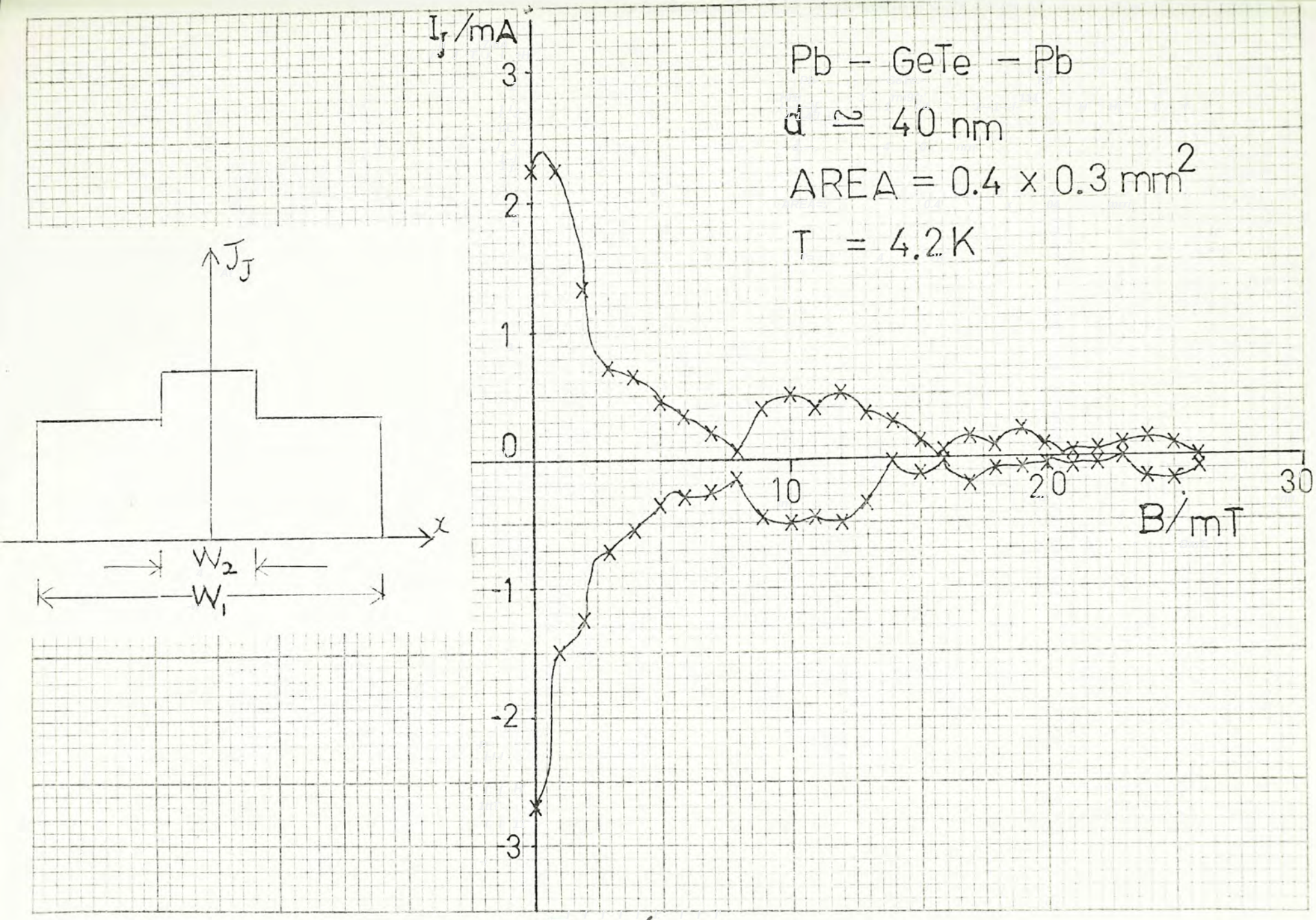
I_J/mA
3
2
1
0
-1
-2
-3
10
20
30
B/mT
Pb – GeTe – Pb
d ≃ 40 nm
AREA = 0.4 x 0.3 mm^2
T = 4.2K
J_J
x
W_2
W_1

FIG. 6.4a

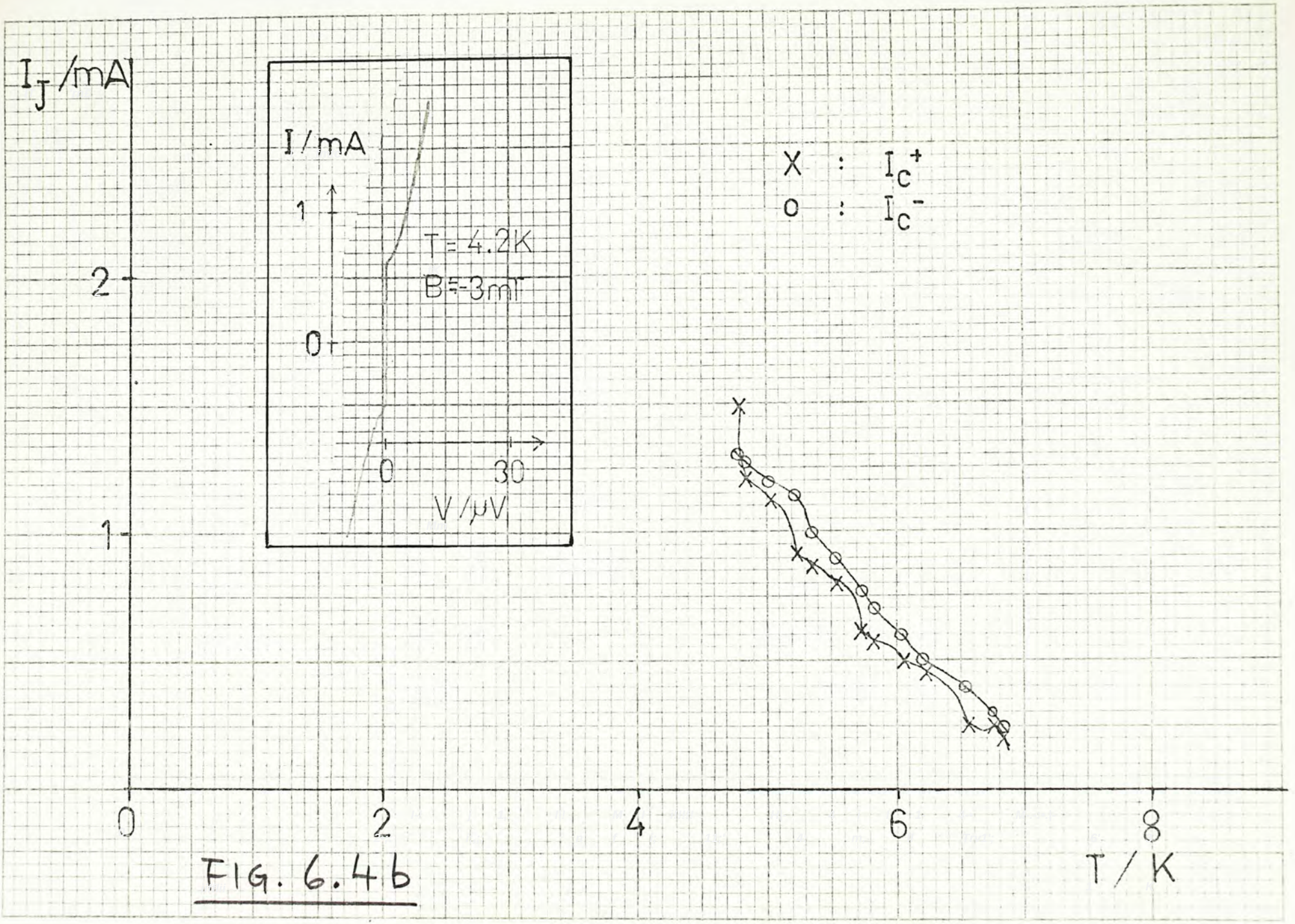

FIG. 6.4b

FIG. 6.5

FIG. 6.5 a

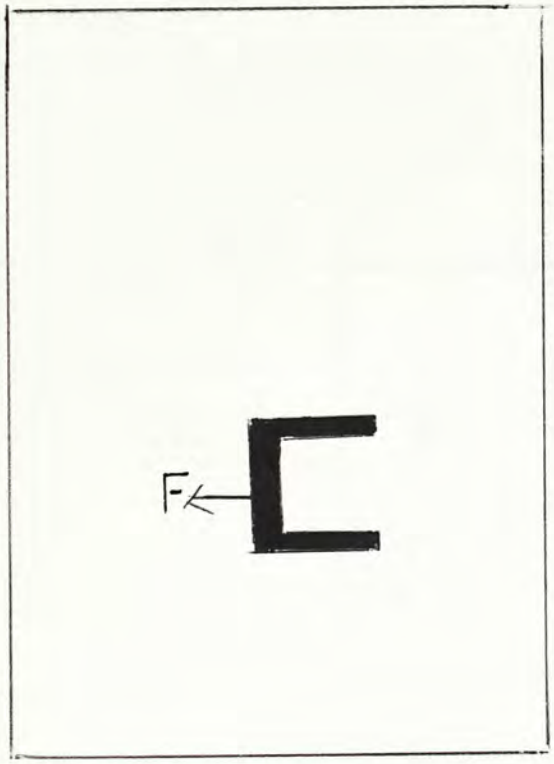

FIG. 6.5 b

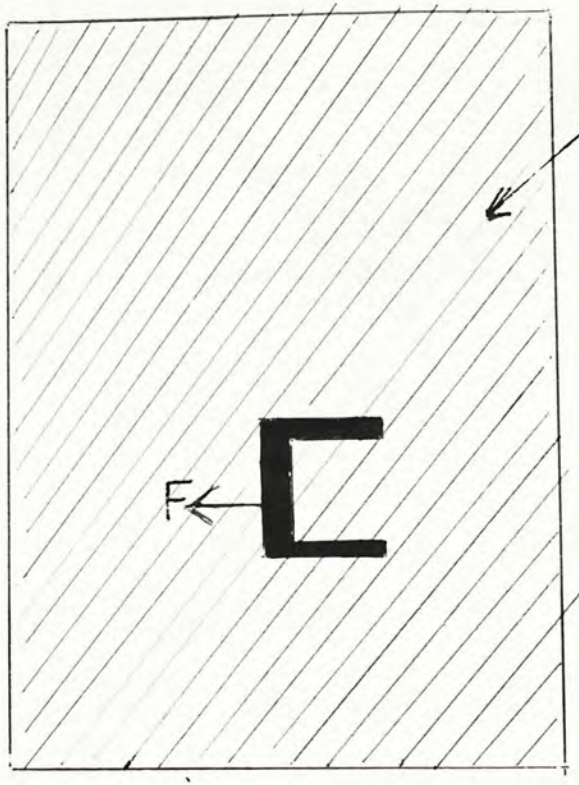

FIG. 6.5 c

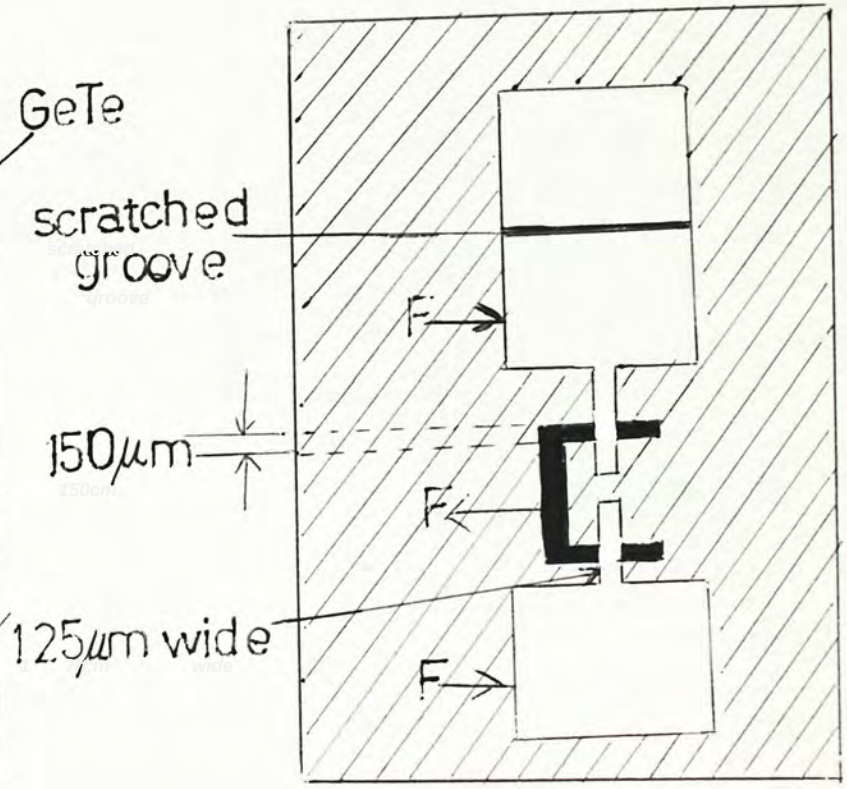

F : filter and connection pads

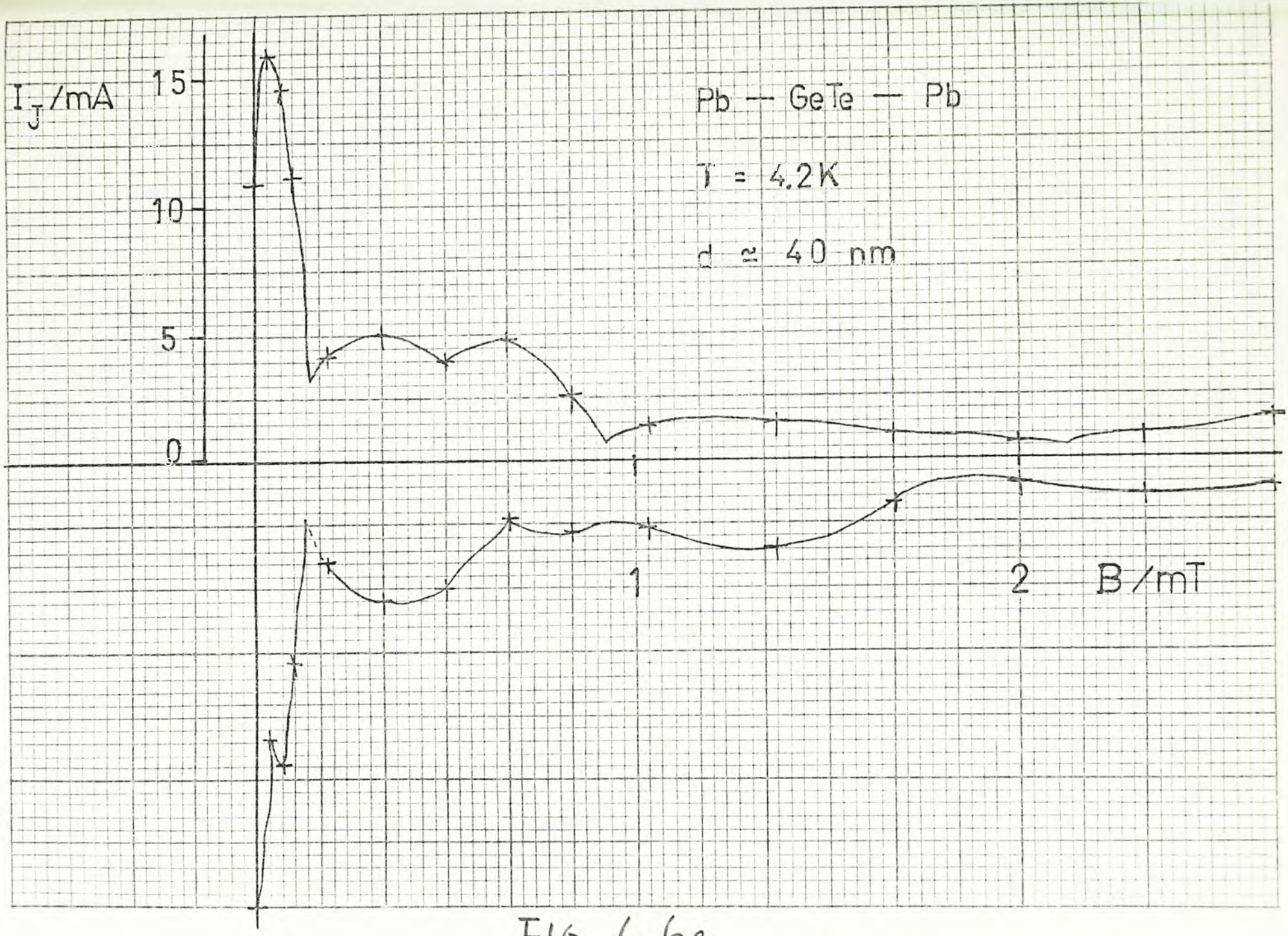

FIG. 6.6a

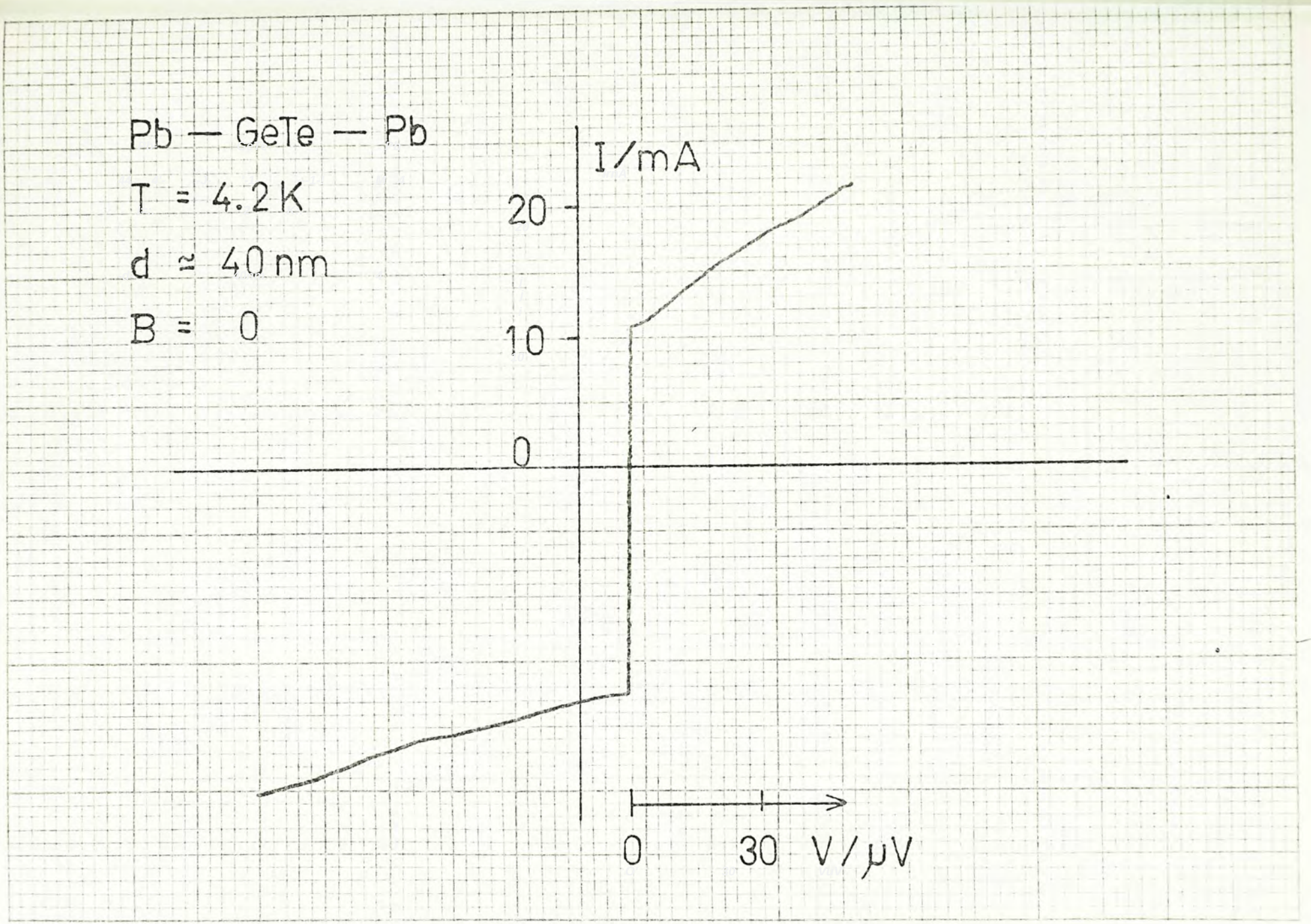

FIG. 6.6 b

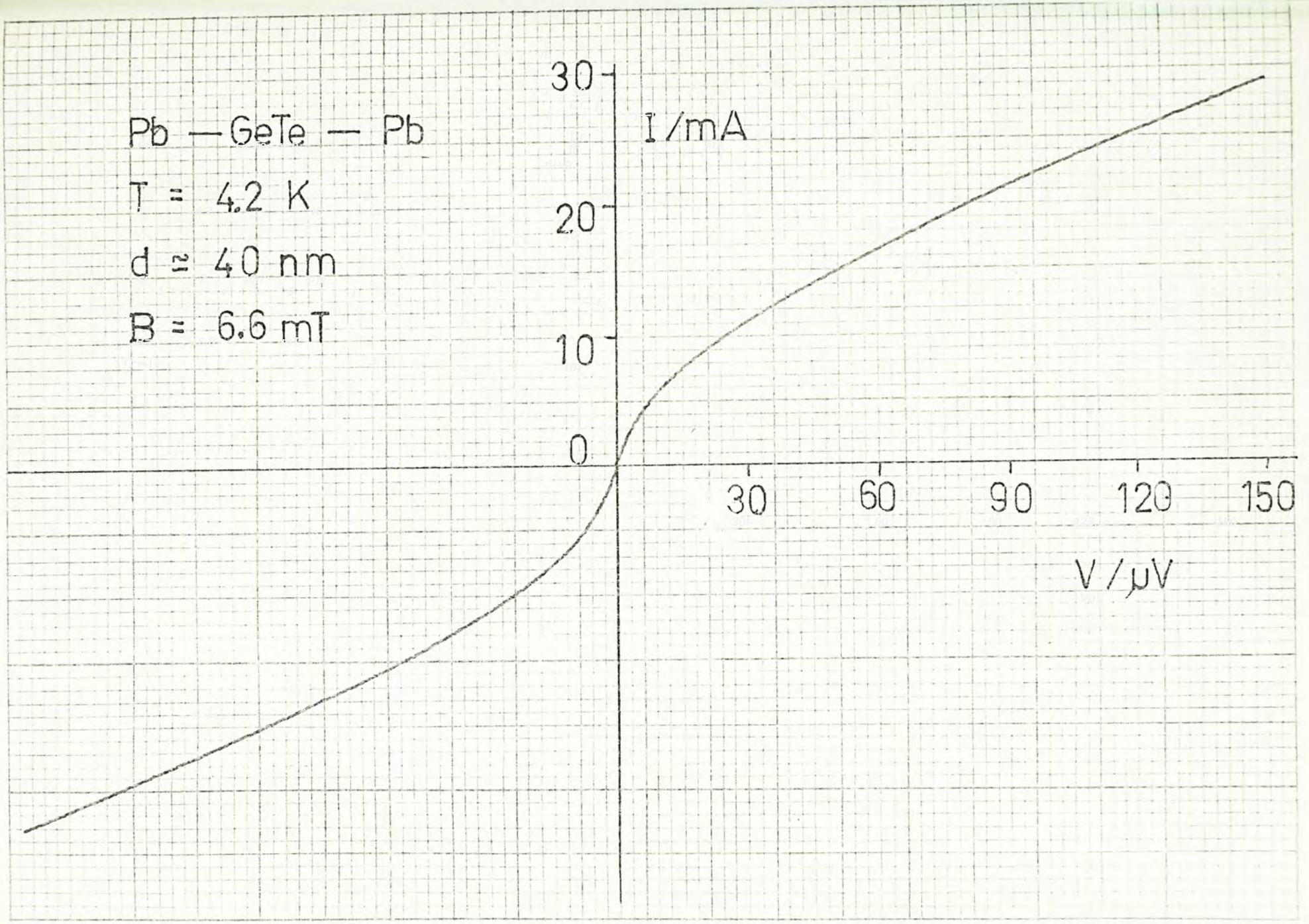

FIG. 6.6c

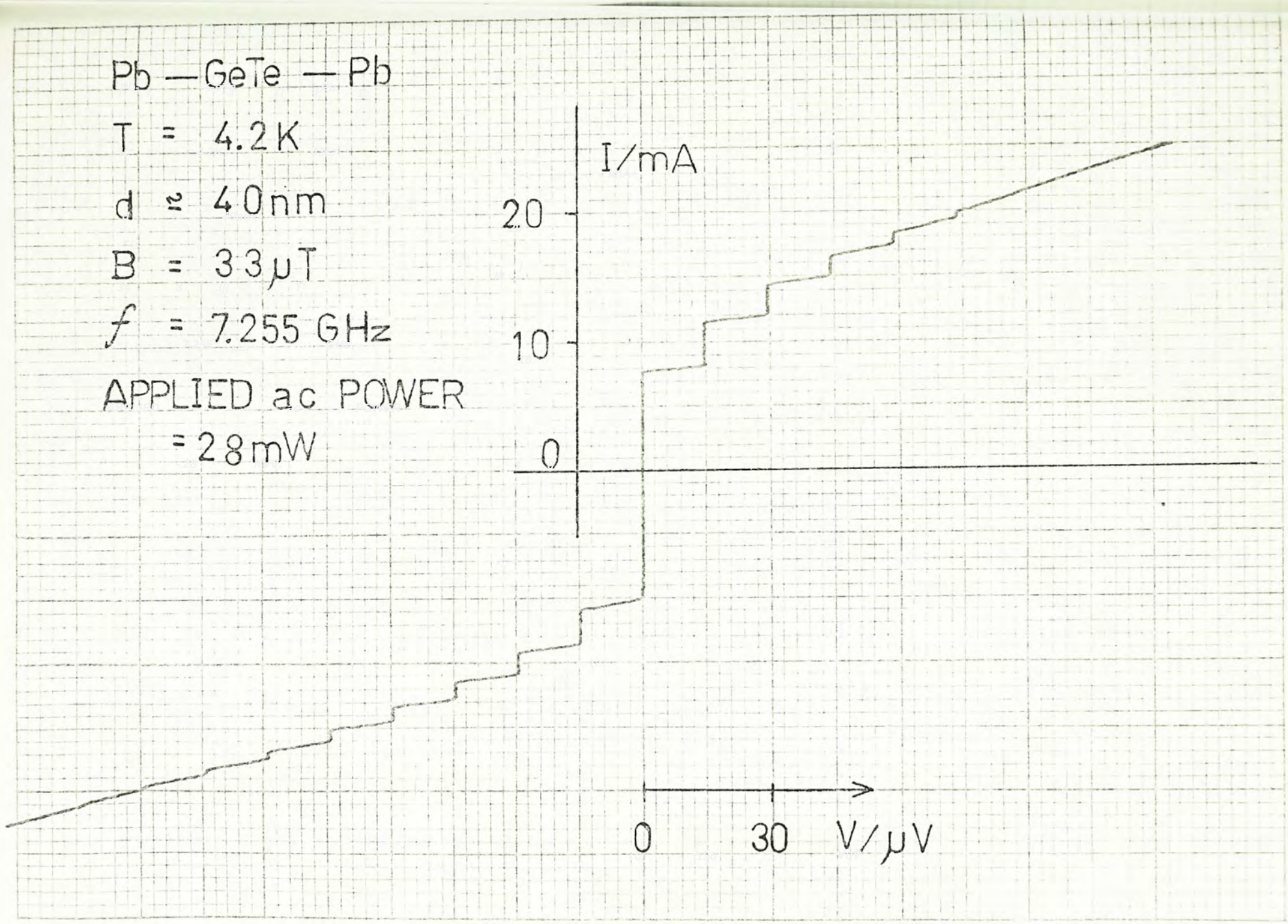
Pb — GeTe — Pb
T = 4.2K
d ≃ 40nm
B = 33μT
f = 7.255 GHz
APPLIED ac POWER
= 28mW
I/mA
20
10
0
0
30
V/μV

FIG. 6.7a

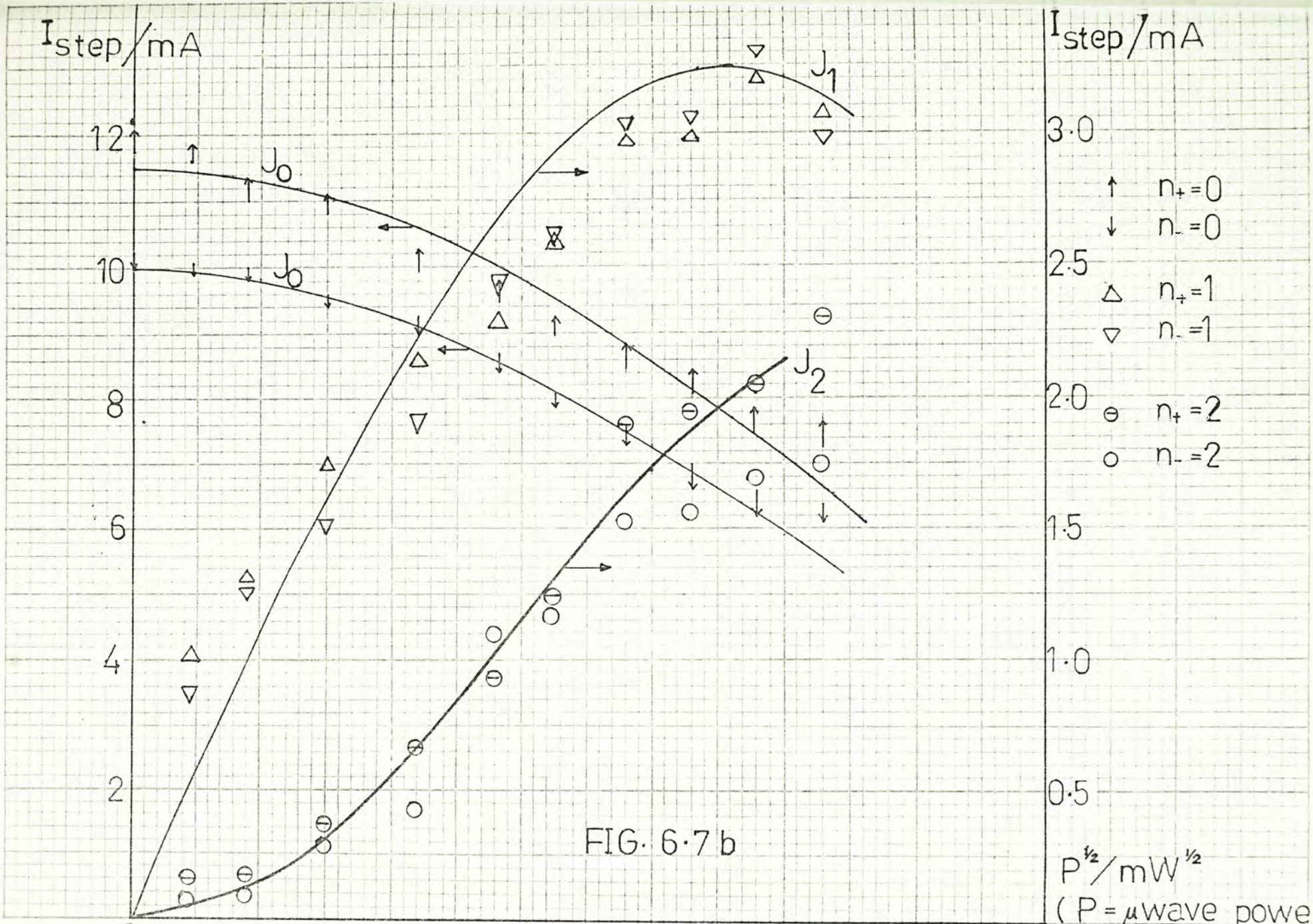

FIG. 6·7b

FIG 6·7b

APPENDIX I (A 1)

COMMENT ON SUBHARMONIC STRUCTURE IN SUPERCONDUCTIVE TUNNELING

ABSTRACT

We propose to explain the initial apparent deviation of the dependence of subharmonic structure on the square of tunneling matrix element, M, reported by Giaever et al. in photosensitive Sn-CdS-Sn Josephson junctions.

1. INTRODUCTION

The theory and experiment each had an inconvincing point to conclude that both odd and even subharmonic structures are caused by Josephson effect rather than the multiparticle tunneling mechanism suggested by Rowell and Feldmann [1] for the even subharmonic series.

The theory's query was solved by McDonold et al [2]. For experimental evidence, Giaever et al [3] had earlier measured the dependence of the subharmonic structures on the tunneling matrix element M. M^2, which is proportional to I_J, is increased by decreasing the CdS barrier height with optical illuminations. The measured dependence with Sn-CdS-Sn tunnel junctions changed from a much faster increase to the anticipated M^2 dependence as the length of illumination is increased.

Giaever's results, as well as the latter numerical computations of McDonald et al [2], support the Werthamer's tunneling theory [4] that the subharmonic structures are caused by self-detection of Josephson radiation.

Giaever distinguished the 2 types of observed dependences on M as weak-coupling and strong-coupling cases, so that the M^2 dependence is only valid for a strongly coupled junction. However, this has not yet been well explained.

2. Qualitative interpretation

We interpret the apparent deviation from M^2 dependence in terms of a Josephson junction model of McDonald et al.

In this model, a load element, known as Mattis-Bardeen [5] superconducting load, is used to include the effects of the superconducting electrodes, which are resistive to ac field.

The I-V curve of the junction depends, among others, on a product of 2 ratioes γ_M and σ_{MB}

where $\gamma_M \equiv \frac{R_E}{R_{NN}}$ is the ratio of the normal resistances of the M-B load to the junction,

and $\sigma_{MB} \equiv \frac{\sigma_E}{\sigma_N}$ is the corresponding ratio of the conductivities at the frequency corresponding to the gap voltage.

The computations are in terms of the first parameter γ_M.

As γ_M increases from 0.1 to 5, the midgap structure does increase rapidly at first. Then it changes slowly and finally decreases smoothly at higher γ_M.

We suggest that roughly the same trend is followed in Giaever's results, e.g. Fig.4 of [3]. But they do not need to change at the same rate due to the other parameter σ_{MB} not being considered. Here, the corresponding increase in γ_M is simply due to photosensitivity and conductivity storage [6, 7] of the CdS barrier. I_J, or M^2, is increased successively in powers of 2 over a range of $\sim 10^2$. Hence γ_M also increases in a similar manner and a normalization factor of $1/I_J$ is required. This is straightforward in the semilog scale used in the IV characteristics. The curves are simply shifted along the logI

axis, but the appearance also suggests $I_J R_{NN} \simeq$ constant. This latter observation will be discussed latter.

To make the comparison, it is essential to make allowances for the following limitations.

1. The Sn-CdS-Sn junction is a 1 mm^2 wide junction whereas Wherthamer's tunneling theory is for small junction.
2. Spurious conduction for CdS barrier junction, which are absent in the theory for S-I-S junction.
3. Thermal smearing at $t \equiv \frac{T}{T_c} \sim 0.54$ for Giaever's measurement temperature. Werthamer's theory is for t = 0.
4. Change from voltage biasing to current biasing as γ_M is increased. It appears from the I-V and $\frac{dV}{dI}$ vs. V curves that the CdS junctions were measured with I biasing.

It is a qualitative comparison between S-S'-S and S-I-S junctions under different conditions. Thus, one of the spurious conduction current component suggest by N-S'-N junctions for tunneling across low potential barrier gives rise to a nearly exponential dependence of I on V for low V. This, together with the other factors, will explain why the higher order subharmonic structures are less obvious.

McDonald et al. suggest the Sn - CdS - Sn results resemble the

Y_M = 5 —20 cases in which the higher order subharmonics are also smaller. This restriction is not necessary in view of so much differences between the 2 cases. Moreover, that would not account for the observed trend of the subharmonics for increasing M^2.

The next remark concerns the appearances of the structures. Rowell and Feldmann classified the old and even subharmonic series to have cusplike and steplike appearances respectively. This is indeed observed from the computational results of McDonald et al, except that the so called steplike structure can also exhibit negative resistance behaviour although in a smooth manner. Based on the appearances of the curves of McDonald et al, a mathematical classification of the appearances of the structures is that $\frac{dI}{dV}$ vs. V has a discontinuity for odd harmonics but is continuous for even harmonics. This is consistent with the Reidel peaks at $\frac{V_g}{2n + 1}$.

Under current bias, even a smooth negative resistance region will also appear as a voltage jump and be indistinguishable from cusplike structure.

Giaever et al.classified their observations according to whether tunneling path is dominated by thin-spot oxide barrier or CdS barrier which has a weaker M_s. The thin-spot is due to the CdS not forming a continuous layer. Their results were interpreted as changing from cusplike to steplike structure with increasing illumination dosage. We suggest these results can also be interpreted as a transition from S-I-S to S-S'-S

behaviour. A Sn-CdS-Sn junction with thin spots can be viewed as a combination of a fixed oxide junction and a variable CdS junction. The relative importance of the S-S'-S junction increases with the length of optical treatment.

For an S-I-S junction at I biasing, leakage current is small and the model of McDonald et al. is applicable. But both the odd and even subharmonic structures may all have voltage jump and appear as cusplike structure in the previous classification which can be confusing. For S-S'-S junctions with rapidly and monotonically increasing spurious conduction current, all structures would appear as smoothed steplike structure.

3. Physical interpretation

The effects of the decrease in R_{NN} shall not be confused with that of a solely corresponding increase in I_J, which, in the theoretical relation of Ambegaokar and Baratoff [8], is inversely proportional to R_{NN}.

To put it more physically, the decrease in R_{NN} has 2 distinguishable effects, in addition to the increasing dominance of the CdS barrier in the case of less perfect junctions. The first effect, an increase in M^2 and hence I_J, have been taken into account in the normalization procedure.

The results of Giaever et al. show that $I_J R_{NN}$ is roughly constant, but is only $\sim 10^{-2}$ times the S-I-S theoretical limit. The critical current density of $\sim 10^{-4}$ A mm^{-2} is again low. It becomes vague as how and when to classify the junction as a strongly coupled junction at any stage of increasing illumination dosage.

The fact that the electrode material, Sn, is a strongly coupled superconductor does not imply the two separate electrodes of the junction are strongly coupled to each other. These are two different things. It simply suggest an immaterial reduction factor ~ 0.911 of the theoretical $I_J R_{NN}$ value [9]. This much reduced value of $I_J R_{NN}$ is due to the barrier itself. It is more related to the low critical current density rather than the low resistivity of the barrier.

The second effect is an increase of γ_M, assuming R_E remains unchanged. In reality, the effective electrodes can be affected by proximity effect. The dependence of the subharmonic structures on γ_M is actually a physical one.

Both the junction and the electrode interact with the Josephson radiation. γ_M accounts for their different contributions in the interactions. It determines their respective impedance matching to detect the radiation. A change in γ_M changes the importance of both interactions as well as their relative weighinhd. In the limit $\gamma_M \rightarrow 0$, the interaction between the electrode and the radiation is effectively excluded, resulting in no even subharmonies. This corresponds to Giaever's results before the junction is exposed to light, when R_N is obviously large and the midgap subharmonic is obscure. As γ_M is increased and the effect of the electrode becomes significant, the even subharmonics appear. This is superimposed upon the M^2 dependence and will account for the apparently much faster dependence on M^2 when R_N is higher. This impedance matching should also be taken into account to interpret the results.

With a crude comparison of Giaever's results with McDonald's model that includes the electrodes quantitatively, we have found better qualitative agreement to Werthamer's tunneling theory and we believe these previous works are sufficient evidence to confirm the Josephson effect origin of subharmonic structures.

References:

[1] Rowell J.M. and Feldmann W.L.

Excess currents in superconducting tunnel junctions

Phys. Rev. 172, 393 (1968)

[2] McDonald D.G., Johnson E.G. and Harris R.E.

Modeling Josephson junctions

Phys. Rev. B 13, 1028 February 1976

[3] Giaever I, and Zeller H.R.

Subharmonic structure in superconducting tunneling

Phys. Rev. B 4278, June 1970

[4] Werthamer N.R.

Nonlinear self-coupling of Josephson radiation in superconducting tunnel junctions

Phys. Rev. 147, 255 (1966)

[5] Mattis D.C. and Bardeen J.

Theory of the anomalous skin effect in normal and superconducting metals.

Phys. Rev. 111, 412(1958)

[6] Wright H.C., Downey R.J. and Canning J.R.

Conductivity storage in CdS

J. Phys. D 2, 1593 (1968)

[7] Giaever I. and Zeller H.R.

Tunneling into and through evaporated semiconducting films

J. Vac. Sc. Technol. 6, 502 (1969)

[8] Ambegaokar V. and Baratoff A.

Tunneling between superconductors

Phys. Rev. Lett. 10, 486 (1963), Phys. Rev. Lett. 11, 104(E) (1963)

[9] Fulton T.A. and McCumber D.E.

dc Josephson effect for strong-coupling superconductors

Phys. Rev. 175, 585 November 1968

APPENDIX II (A 2)

MODEL OF VOLTAGE-SWITCHING EFFECTS OF THERMAL ORIGIN IN SUPER-CONDUCTIVE WEAK-LINK JUNCTIONS

ABSTRACT

We have generalised the voltage-switching heating model of Iwanyshyn et al. to include all conduction processes and current paths.

INTRODUCTION

Heating effects are trivial but the recognition of them is essential. There has been lots of confusion in the past and these effects are only better explained in recent years.

In particular, Iwanyshyn et al, accounted for the nonlinearity and voltage snapback in the finite resistance regions of d.c. characteristics of various weak links as due to local heating [1]. This model was reported by Kao et al. to be inapplicable to their junctions [2], but we found it is applicable to our imperfect Pb-GeTe-Pb weak links as we had reported before [3].

Here, we try to extend Iwanyshyn's model and compare it with Giaever's model developed for a different situation.

Generalized model for voltage snapback and voltage increase

For weak links of the conventional cross configuration with current biasing, voltage switching sometimes occurs at a current I_s .

Iwanyshyn's model for 2 shorts can be generalized as follows:

Divide the current components through the barrier into 2 parts and represent them by 2 equivalent paths S_1, S_2 through the barrier, with resistances R_1, R_2 respectively. They are divided such that there is a net current flow ΔI along the electrode film from S_1 to S_2 at $I > I_s$.

Here, the current can be due to shorts, tunneling and/or junction resistance.

The configuration and the equivalent circuit for I biasing is shown in fig. A2.1a and b.

In general, the actual current between S_1 and S_2 is not equal to I_2, but the parameter ΔR is chosen such that a current of I_2 through it would give the same potential difference as that between S_1 and S_2 along the electrode film.

$$\text{Now, } R_{eq} = \frac{I_2(R_2 + \Delta R_2)}{I}$$

$$= \frac{R_2 + \Delta R_2}{R_2 + \Delta R}\left[R_1 // (R_2 + \Delta R)\right]$$

$$\text{since } I_2(R_2 + \Delta R) = I\left[R_1 // (R_2 // \Delta R)\right]$$

$$\text{therefore, } Req = \frac{R_1 (R_2 + \Delta R_2)}{R_1 + R_2 + \Delta R}$$

$$= \frac{R_1 R_2}{R_1 + R_2} + R_1\left[\frac{\Delta R_2 - \frac{R_2}{R_1 + R_2}(\Delta R_1 + \Delta R_2)}{(R_1 + R_2) + \Delta R}\right]$$

$$= R_1 // R_2 + \frac{R_1 \frac{R_1 \Delta R_2 - R_2 \Delta R_1}{R_1 + R_2}}{R_1 + R_2 + \Delta R}$$

$$= R_1 // R_2 \left[1 + \frac{R_1}{R_1 + R_2 + \Delta R} \delta \right]$$

where $\delta = \frac{\Delta R_2}{R_2} - \frac{\Delta R_1}{R_1}$

There is voltage switching in the form of voltage increase or voltage snapback at $I = I_s$ according to whether $\delta > 0$ or $\delta < 0$ respectively.

Iwanyshyn et al considered the simplified case with current due to only 2 shorts of equal resistances and with $\Delta R_2 = 0$, so that $\delta < 0$ and voltage snapback is anticipated. In fact, Giaever [4] had earlier anticipated various effects due to heating, but he considered tunneling current only.

In an attempt to illustrate the failure of normal films in four probe measurement of tunneling characteristics, he considered a simplified case with the electrode films in the overlapping configuration as shown in Fig. A2.2.

His equation, expressed in the following modified version

$$R_{eq} = R_T \left[1 - y(x) \right]$$

where $y(x) = 1 + x^2 - x \coth x$

$$x = \frac{R_F}{2R_T}$$

R_T = tunneling resistance

and R_F = normal film resistance

can be seen to result in

$$R_{eq} < R_T \quad \text{for } x \neq 0$$

The cross cinfiguration is qualitatively comparable to the overlapping configuration as shown in Fig. A2.3.

The equivalent circuit shown here obviously reduces to that of our present model when one of the normal films is replaced by a superconducting film. The present modified model, which is essentially an extension of Iwanyshyn's model for 2 shorts, takes all current components into consideration.

References:

1 Iwanyshyn O., Leslie J.D. and Smith H.J.T.
A study of evaporated superconducting weak-link junctions
Can. J. Phys. 48, 470 (1970)

2 Jahn M.T. and Kao Y.H.
Voltage switching effect and microheating in Josephaon weak superconductors
J. Phys. Soc., Japan, 40, 377, Feb. 1976

3 Chan H.H.A. and Chang C.C.
Voltage-switching effect in evaporated weak-link junctions
J. Phys. D: Appl. Phys. 10, L33 (1977)

4 Giaever I.
Metal-insulator-metal tunneling
in "Tunneling phenomena in solids", Plenum Press, N.Y. (1969), Chapter 3, edited by Burstein E. and Lundquist

FIGURE CAPTIONS:

Fig. A2.1 Model to represent heating of a weak link junction

(a) configuration

(b) equivalent circuit

Fig. A2.2 Representation of tunneling junction in the overlapping configuration

Fig. A2.3 Cross configuration vs. overlapping configration for normal electrodes

FIG.A.2.1a

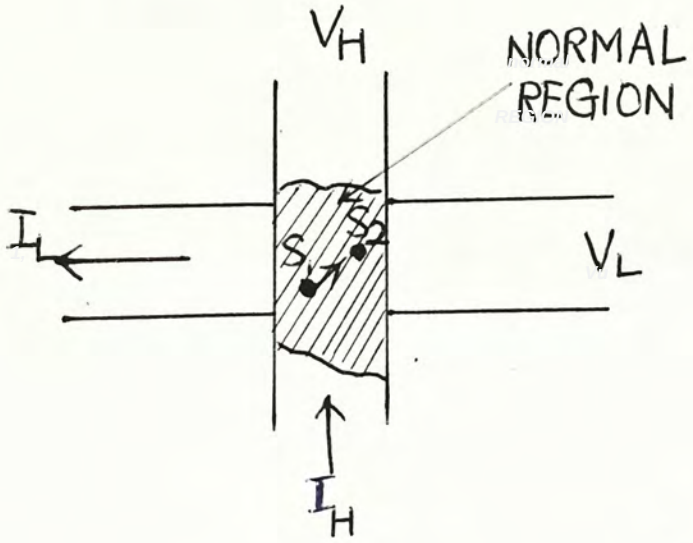

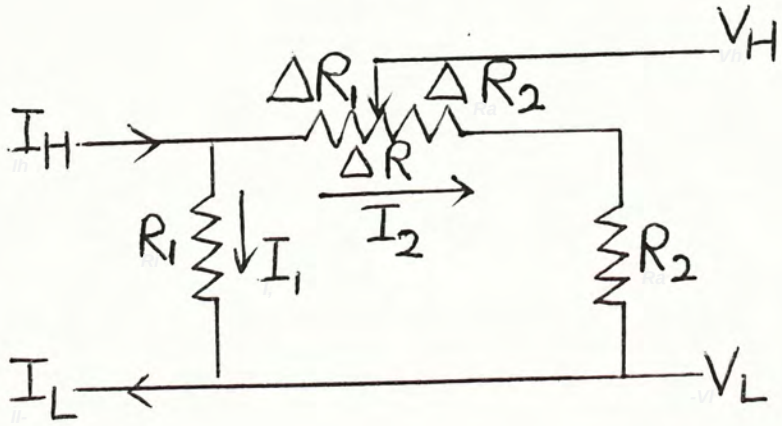

FIG. A 2.1b

I : current
V : voltage

Subscripts meaning,
H : High terminal
L : low terminal

FIG.A.2.2

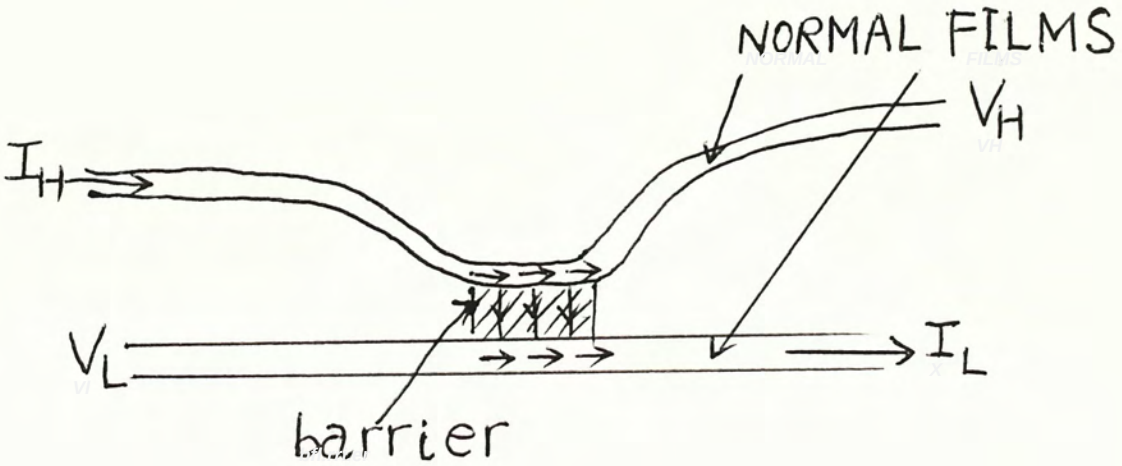

FIG. A 2·3

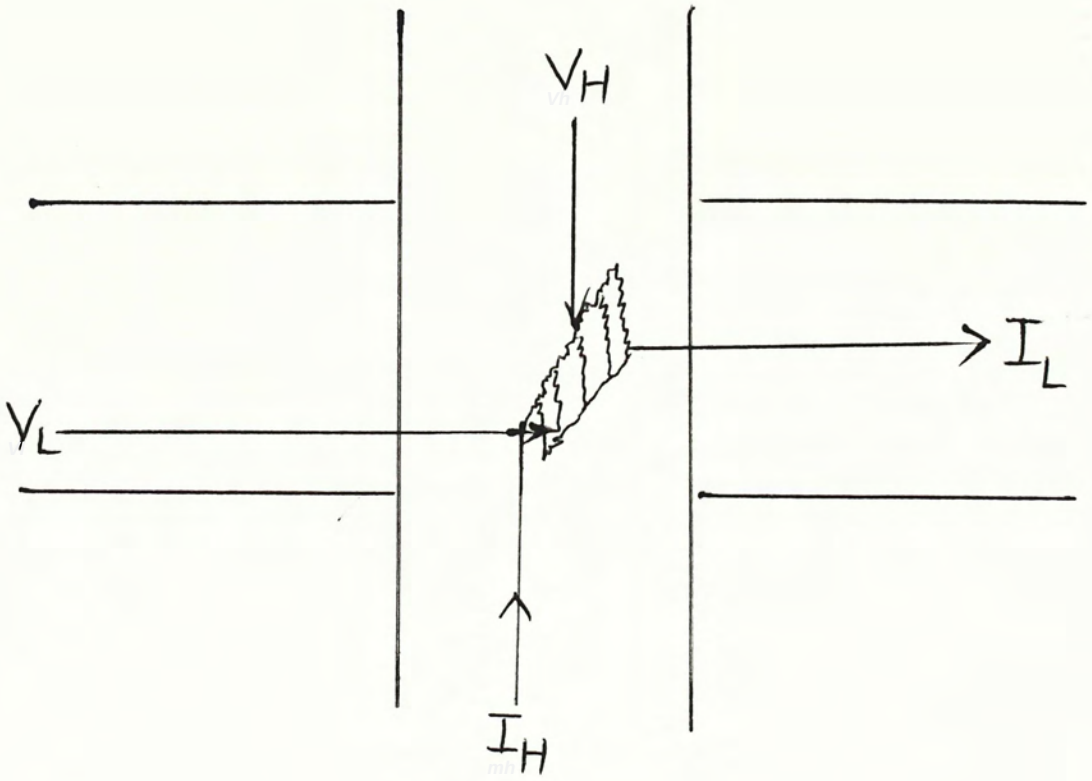

APPENDIX III (A 3)

METAL CONTACT INDUCED LASER WRITING OF GeTe ON Pb

ABSTRACT

We have observed metal contact induced crystallisation of GeTe on Pb, at lower threshold energy and with enhanced refectivity contrast between the amorphous and recrystallised phases of GeTe due to the metal backing.

Metal contact induced crystallisation had been reported for Si and Ge[1-3]. As the semiconductor film is gradually heated up, the amorphous semiconductor film crystallizes at a lower temperature when there is a metal film backing. This reduced crystallisation temperature depends on the metal and is emphirically related to the eutectic temperature between the semiconductor and the metal. The mechanism is not yet well established. But for some metal-semiconductor system, there is experimental evidence of compound formation or grain growth of the metal. This may indicate the crystallisation temperature depends on interdiffusion or kinetics of mass transport at the metal-semiconductor interface.

Evaporated GeTe film is amorphous and, on ordinary substrate, a sharp transition to the crystalline form occurs at $T \simeq 150^{\circ}C$ for film thickness $d > 35$ nm, the crystallisation temperature increasing as d is reduced [4].

Ge_xTe_{1-x} compound, a member of the Te based chalcogenide, is also of interest for data processing applications due to the change of dielectric constant ϵ_r as the film is crystallised or reamorphised. Previous reports use the conventional substrates[5]. We have investigated whether the metal contact induced crystallisation will also apply for GeTe.

We use evaporate amorphous GeTe on a previously evaporated Pb film on glass substrate, and He-Ne laser (Laser Associates 211) at 1 ms pulse time. The recrystallisation under these conditions is sharp and complete at macroscopic local regions. We have checked this

with GeTe of d ≃100 nm. The substrate is blocked with a Cu wire during evaporation of the Pb backing film. This gap serves for resistivity measurement of GeTe on glass. The resistivity of the base GeTe on glass changes from ~4 x 10^{4} to ~2x 10^{-3} Ω mm on recrystallisation. This corresponds to increase reflectivity observable with the bare eye and the boundary between the two phases is sharp. There is also practically no difference between GeTe on glass and GeTe on lead (Fig. A 3.1) for this GeTe thickness. This is expected since the GeTe film is already nearly reflecting, implying $d > \lambda_{op}$, where λ_{op} is the penetration depth of optical radiation.

For thin GeTe with d ≃20 nm, thecrystallisation requires higher laser power, in qualitative areement with the thermally induced transformation [4]. The GeTe on glass requires nearly damaging laser power and the reflectivity contrast is small, whereas the GeTe on Pb recrystallises at a comparatively lower power and gives better contrast (Fig. A3.2a).

For transparent substract backing, the light reflected from surface is to be contrasted so that ϵ'' ($\vec{\epsilon} = \epsilon' + i\,\epsilon''$) is important. With the metal backing, there is an additional interfering light component reflected from the metal surface with absorption in GeTe for the double journey. Hence ϵ'also plays a role to contribute to the contrast.

We have not yet made quantitative investigations. The required laser power is inferred by the distance of the phases boundary from the center of the laser gaussian beam. By using lower power with no damage of the film, the GeTe on glass has not recrystallised from both visual observation and resistivity measurement, whereas GeTe on Pb has already grown to macroscopic grains (Fig. A3. 2b).

We are planning to investigate for possible re-amorphisation with shorter laser pulse time, in order to establish whether the enhanced contrast with the metal backing can be potentially, applicable to laser writing, reading and erasing on chalcogenide films.

REFERENCES

[1] Herd, Chaudhari and Brodsky
Metal contact induced crystallisation in films of amorphous Si and Ge
J. non-crystalline sol. 7, 309 (1972)

[2] Ohi F., Ogawa Y. and Fujki Y.
Effect of deposited metals on the crystallization temperature of amorphous germanium film
Japan. J. Appl. Phys. 8, 1056 (1969)

[3] Brodsky and turnbull

Bull, Am. Phys, Soc, 2, 304 (1971)

[4] Chopra K. L. and Bahl S.K.
Amorphous versus crystalline GeTe films. I. Growth and structural behavious
J. Appl. Phys. 40, 4171 (1969)

[5] Levinson G. R. and Smilga
Laser processing of thin films (review)
Sov. J. Quantum Electron. 6, 885 (1976)

FIGURE CAPTIONS:

Fig. A3.1. Recrystallisation of GeTe film on Pb and on glass with GeTe thickness d ~100 nm. The crystalline phase is more reflecting.

Fig. A3.2. Recrystallisation ofGeTe film on Pb and on glass with d~20 nm.

(a) The phases boundary is at a larger distance from center of laser beam when there is Pb metal film backing. Enhanced reflectivity contrast is also shown.

(b) With lower laser power

The GeTe on glass has not recrystallised. The scratched grooves are for resistivity measurement.

FIG.A3.1

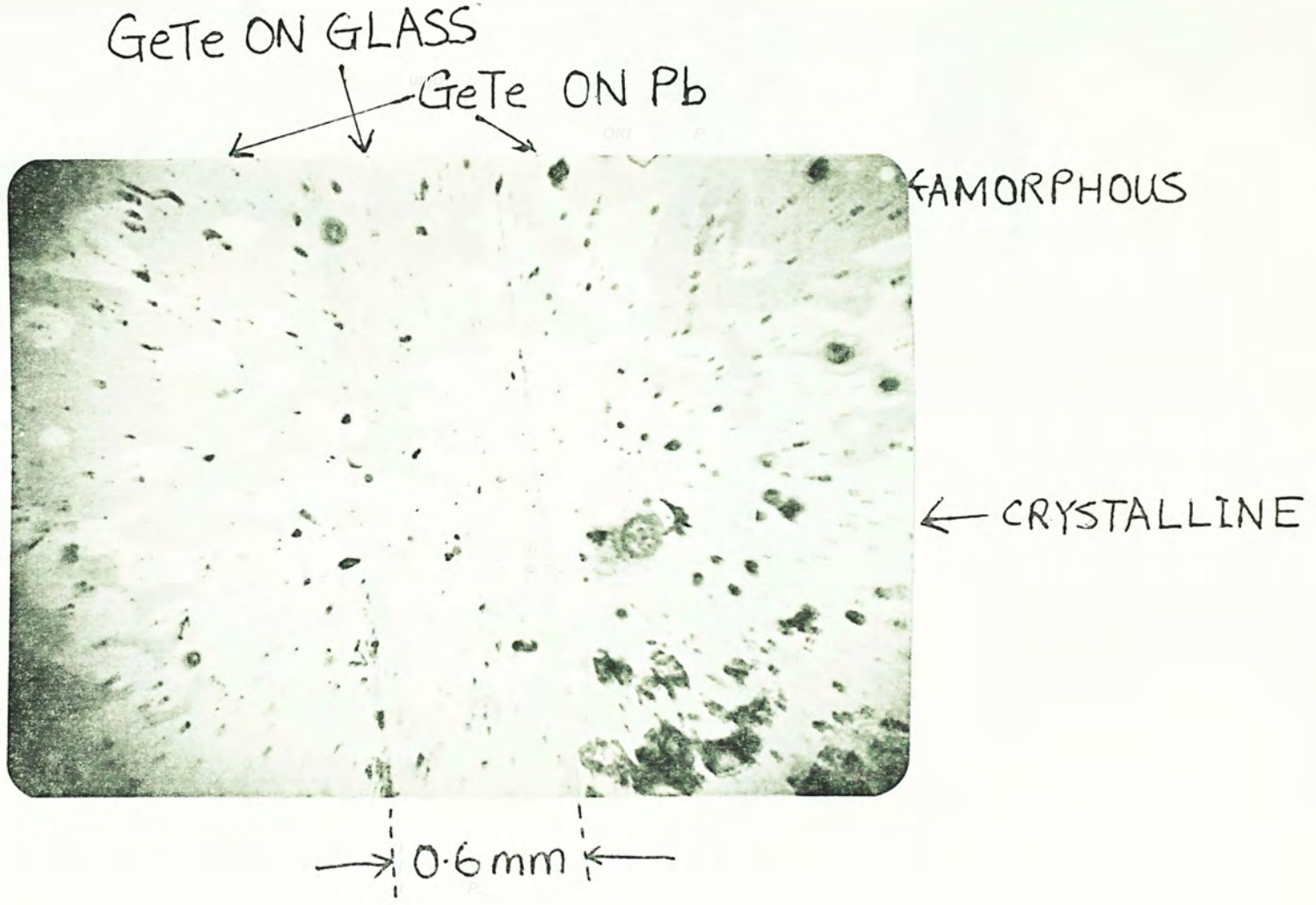

FIG. A 3. 2

FIG. A3.2a

FIG. A3.2b

APPENDIX IV (AIV)

IMPERFECT WEAK-LINK JUNCTIONS WITH GE BARRIER

ABSTRACT

We have investigated the possibility of using Ge as a thick barrier for Josephson tunneling and we propose to explain the differences among the previous results.

1. INTRODUCTION

Very thin Ge behaves as an insulating barrier and Josephson tunneling is possible for barrier thickness $d \lesssim 5$ nm [1] with essentially oxide junction characteristics. With thick Ge, different results of quasi-particle tunneling [2] and anomalously high zero voltage current [3] have been reported.

We have investigated junction with thick Ge barrier thickness of d= 20 - 200 nm . We have taken into account the thickness, doping level and crystallization of the semiconductor, as well as electrode considerations against the occurrence of microshorting.

2. RESULTS

Our junctions are of the conventional cross configuration. The well behaved junctions give quasi-particle tunneling with large excess current. If the base electrode is not well prepared [4, 5], the junctions are sensitive to electrical transients and and microshorting can occur even with sufficient pinhole oxidation.

Fig. A4.1 shows the quasi-particle with $Pb_{.9}$ $In_{.1}$ as base

electrode. Hillock formation [5] of Pb causing shorts is suppressed with the dilute Pb-In alloy. If pure Pb is used as base electrode and with air for pinhole oxidation, the junctions are mostly shorted (Fig. A4.2) due to hillock formation and N_2 adsorption which inhibits oxidation. Ge highly doped with Al to 10^{16} mm^{-3} is used as the starting evaporant for the barrier. Ge is recrystallised by metal contact induced recrystallisation [6] at the high oxidation temperature but diffusion of Pb can compensate the Al doping resulting in a high resistance junction.

With Sn electrode well evaporated by reducing with Ta [4], and with moderately doped Ge as barrier, normal tunneling is again obtained showing also the Ge barrier at higher voltage. This is shown in (Fig. A4.3a). An oxide junction simultaneously prepared on the same substrate to check the oxidation condition for this junction shows quasi-particle tunneling only (Fig. A4.3b). Another parallel oxide junction on a different substrate oxidised less heavily shows dc Josephson effect (Fig. A4.3c). The oxide junctions show that the $T \simeq 80^{\circ}C$ for oxidation is not too high against grain motion for Sn to cause microshorts. This temperature is used so that Ge is recrystallised on Sn [6]. The above Ge junction has high resistance probably due to the large vapour pressure difference between Ge and Al during thermal evaporation. Another such junction incidently has a degenerate Ge barrier as shown by $\frac{R(T)}{R}$ measurement (Fig. A4.4a). The $R_{NN}(T)$ measurement for T= 300 K to 77 K is also used to check against significant

electrode. Hillock formation is observed for Cu annealing above 200°C in vacuum while hillock formation and N_2 adsorption which inhibits oxidation, the Josephson junctions are mostly shorted (Fig. 4.4.5) due to hillock height comparable with Al thickness (~ 1000 Å). Cu is used as base electrode and will be protected by a thin layer of Al which is subsequently oxidized in glow discharge oxygen plasma to form the tunnel barrier. The oxidation condition is optimized by monitoring the I-V characteristics of Al/Al-O/Cu junctions. The oxide thickness is estimated to be ~ 15 Å (Fig. 4.4.6). An oxide junction with thinner oxide barrier is also prepared on the same substrate to check the oxidation condition for thick junction shows sharp-basin tunneling only (Fig. 4.4.7). Another parallel oxide junction on a different substrate oxidized less heavily shows Josephson effect (Fig. 4.4.8). The oxide junctions show that the T_c of 8.0°K for oxidation is not too high because microshorts. This temperature may be used as first Cu is recrystallized on Si at 500°C. The above Cu is used to check against significant pressure difference between Cu and Al during thermal evaporation. Another such junction incidentally has a degenerate Cu pattern as shown by measurement (Fig. 4.4.8). The $R_{NN}(T)$ measurement for $T = 300$ K to 77 K is also used to check against significant

with Si electrode evaporated by regular Al-Al oxide tunnel junction. Cu is selected as base electrode because it is relatively inert to Al oxidation. Cu is also used as the first layer to be evaporated on Si substrate. Cu is recrystallized at 500°C in vacuum to improve the film quality. Cu is protected by Al during

metallic microshorts, but this method is only meaningful for junction resistance larger than the normal resistance of the electrode at the junction. There should be no large Sn microshort for this junction, otherwise $R_{NN}(T)$ would decrease from T= 300 K to 77 K. The junction has $T_c \simeq 3.3$ K but I_c increases roughly exponentially for $T \lesssim T_c$ and does not correspond to the $I_c(T)$ dependence of any type of Josephson junction. The $I_J(H)$ for this junction shows little periodicity up to the critical field of S_n. We believe this is due to inhomogeniety of the barrier composition. For Al-Ge film evaporated on 77 K substrate, T_c = 5.5 K decreasing to 2.44 K after annealing [7] whereas T_c for possible Al particles can be higher than the T_c = 1.18K of bulk Al. Thus, there can be an inhomogeneous composition of Al rich aggregates with an increasing number to become superconducting as T is lowered. If the supercurrent is actually through Ge, it can only be due to the inhomogeneous crystallisation of Ge. Germanium does not crystallize homogeneously. Thus Ge evaporated at room temperature does contain a little polycrystalline phase composition [8] and the crystallisation growth rate from the nucleation centres is slow [9]. The present junction has $\rho \simeq 40\ \Omega$mm.

Another low resistance Sn-Ge-Sn junction of d $\simeq$ 75 nm has $I_c \simeq I_c$ of Sn. $I_c(T)$ is almost linear (Fig. A4.5a) but $I_c(H)$ has the SLUG type characteristics (Fig. A4.5b). Ge is crystallized and has $\rho \sim 2\ \Omega$ mm.

Both $I_c(H)$ and the known crystallization kinetics of Ge

shows that this semiconductor is not a suitable barrier for Josephson tunneling. The results of junctions with Ge barrier of $d \simeq 20 - 200$ nm and $\rho \sim 10^2 - 10^4$ Ω mm shows no dc Josephson effect. With thick barrier, Josephson effect is possible by proximity effect for a degenerate semiconductor [10], but this resistance range is too large for proximity effect. Konig [2] has also found only quasi particle tunneling for Ge barrier of $d \simeq 25 - 80$ nm.

3. WEAK LINK CHARACTERISTICS

We have also investigated the heating effect in a shorted junction of $Pb_{.1}In_{.9}$-Ge-$Pb_{.1}In_{.9}$. The short is indicated by $I_c(H)$. It is hysteretic (Fig. A4.6a) with another current step at high power level (Fig. A4.6b) The linear I-V region extrapolated backward cut the voltage axis at a non-zero current and is characteristic of long-bridge solution [11]. It has $I_c \propto (1-t)$ for $T \lesssim T_c$ and $I_{min} \sim (1-t)^{0.34}$ where I_{min} is the back switching current to zero voltage. The junction resistance is $R_{NN} \simeq 8.7\,\Omega$ and $I_c R_{NN} \simeq 10^2$ mV, far exceeding the theoretical value of Ambegaokar and Baratoff [12]. This seemingly high $I_c R_{NN}$ can be explained by heating effects in microshorting. As I is increased, the metallic microbridges turns normal at local restrictions. As I_c is reached, a hot spot [11]

at the restrictions spread out along the wider parts of the microbridge and causes R_{NN} to decrease. Thus I_c is determined by a smaller value of R at a restriction along a long microbridge. The same applies to evaporated weak-links junctions of Iwanyshyn et al. [13]. Lipson and Stupel reported anomalously high zero voltage current for d≃29 - 300 nm. Our calculations from their results shows that Ge has high resistivity $\rho \sim 10^{3-4}$ therefore corresponds to the highly amorphous phase. From both theory and experimental results discussed above, Josephson effect should not be observable for such thickness. Their junctions have large hysteresis and bridge type I-V. Our estimate from their results also shows $I_c R_{NN} \sim 10^2$ mV. We note that the $I_c(T)$ is more close to $I_c \propto (1-t)$ rather than $I_c \propto \frac{\pi\Delta}{2eR} \tanh \frac{\Delta T}{2kT}$ as claimed. All these results resemble those of our shorted junction. These features also resemble the microbridge junctions of Smith et al. [14].

From the hot spot model of Skocpol et al. [11], $\frac{I_{min}}{I_c} \propto I_c^{-\gamma}$ for $T \lesssim T_c$ and $\gamma \simeq 0.5$ for $I_c \propto (1-t)$. We have fitted the results of Lipson et al. to the above power law for hot spot model against the capacitive shunted Josephson model [15]. $\gamma \simeq 0.47$ is obtained (Fig. A4.7).

4. CONCLUSION

Josephson tunneling by proximity effect through thick Ge barrier of $d \simeq 20 - 200$ nm and relatively high $\rho \simeq 10^{2-4}$ Ω mm is not observable. Previously reported results for anomalously high zero voltage current in Sn-Ge-Sn junction resemble the characteristics of our shorted junction and of microbridge junction. Those junctions can possibly be interpreted as due to microshorts.

REFERENCES

1 Keller W.H. and Nordman J.E.
Niobium thin-film Josephson junctions using a semiconductor barrier
J. App. Phys. 44, 4732, Oct. 1973.

2 Konig B.
Tunneling with Ge-barriers
Phys. Lett. 39A, 493 (1970)

3 Lipson S.G. and Stupel M.M.
Induced superconductivity in Germanium films
Phys. Lett. 33A, 493 (1970)

4 Kahan G.J., Delano R.D. Jr., Brennemann A.E. and Tsui R.T.C.
Superconducting tin films of low residual resistivity
IBM J. Res. Dev. 4, 173 (1960)

5 Emmanuel A., Donaldson G.B., Band W.T. and Dew-Hughes
Barrier formation in lead-based tunnel junctions studied by surface techniques
IEEE Trans. Mag. MAG-11, 763 (1975)

6 Oki F. and Ogawa Y.
Effect of deposited metals on the crystallization temperature of amorphous germanium film
Japan J. Appl. Phys. 8, 1056 (1969)

7 Deutscher G., Farges J.P., Meunier F. and Nedellec P.
Phys. Lett. A35, 265 (1971)

8 Halder N.C., Montante J.M. and Swartz W.E. Jr.
Evidence of a polycrystalline phase in amorphous Ge films evaporated at room temperature
Phys. Stat. Sol. (a) 39, 213 (1977)

9 Germsin P., Squelard S., and Bourgoin J.
Crystallization kinetics of amorphous germanium
J. Appl. Phys. 48, 1909, May 1977

10 Seto J. and Van Duzer T.
Theory and measurements on lead-tallurium-lead supercurrent junctions
"Low Temperature Physics" LT-13 3, 328 (1972)

11 Skocpol W.J., Beasley M.R. and Tinkham M.
Self-heating hotspots in superconducting thin film microbridges
J. Appl. Phys. 45, 4054 (1974)

12 Ambegaokar V., and Baratoff A.
Tunneling between superconductors
Phys. Rev. Lett 10, 486 (1963)
Phys. Rev. Lett. 11, 104(E) (1963)

13 Iwanyshyn O., Leslie J.D., and Smith H.J.T.
A study of evaporated superconducting weak-link junctions
Can. J. Phys. 48, 470 (1970)

14 Smith C.W. and Bohner J.J.
Current-voltage characteristics of a new type of superconducting thin film bridge
Phys. Lett. 51A, 453 (1975)

15 McCumber D.E.
Effect of ac impedance on dc voltage - current characteristics of superconductor weak-link junctions
J. Appl. Phys. 39, 3113 (1968)

FIGURE CAPTIONS

Fig. A4.1 $Pb_{.9}In_{.1}$-Ge-$Pb_{.9}In_{.1}$ junction (p7.3) with Ge doped to $n_p \sim 10^{16}$ mm^{-3} of Al as starting evaporant. Pinhole oxidation condition: 180°C in air for 10 hours.

$R_{NN}(300\,K) = 5.5\,\Omega$

$R_{NN}(4.2\,K) \simeq R_{NN}(77\,K) \simeq 278\,\Omega$

A4.2 Imperfect Pb-Ge-Pb junction (14B.4) with pinhole oxidation conditions of 85°C in air for 1 hour.

(a) I-V with self induced steps

(b) SLUG type $I_J(H)$ begaviour characteristics of multiple microshorts.

A4.3 (a) I-V characteristics for normal tunneling across Ge barrier for Sn-Ge-Sn junction (13A.5). The pinhole oxidations are: 80°C in O_2 for 1 hour.

(b) Quasi-particle tunneling characteristics for Sn-SnOx-Sn junction (13A.1). Under same oxidation conditions as the junction in (a).

(c) $I_J(H)$ for a Sn-SnOx-Sn Josephson junction (13B.1). The oxidation is in air and hence less severe but with same temperature and duration as in (a).

A.4.4 Imperfect Sn-Ge-Sn junction (12B.1) with thick recrystallised barrier. (a) Low power resistance of junction against temp. $R_{NN}(T)$ is inexact due to intrinsic problem with normal metal electrodes in 4 probe measurement. (b) $I_J(T)$ for $T \leq T_c$

A4.5 Imperfect Sn-Ge-Sn junction (12B.1) oxidation conditions: 80°C in O_2 for ½ hour. (a) $I_c(T)$ is almost linear (b) SLUG type $I_c(H)$

A4.6 Shorted $Pb_{.1}In_{.9}$-Ge-$Pb_{.1}In_{.9}$ junction (7A.1) with microbridge characteristics (a) I-V with large hysteresis (b) I-V at higher power with another step due to heating (c) $I_c/3$ and I_{min} vs (1-t) where $t=T/T_c$.

A4.7 I_c vs the hysteresis parameter I_{min}/I_c .

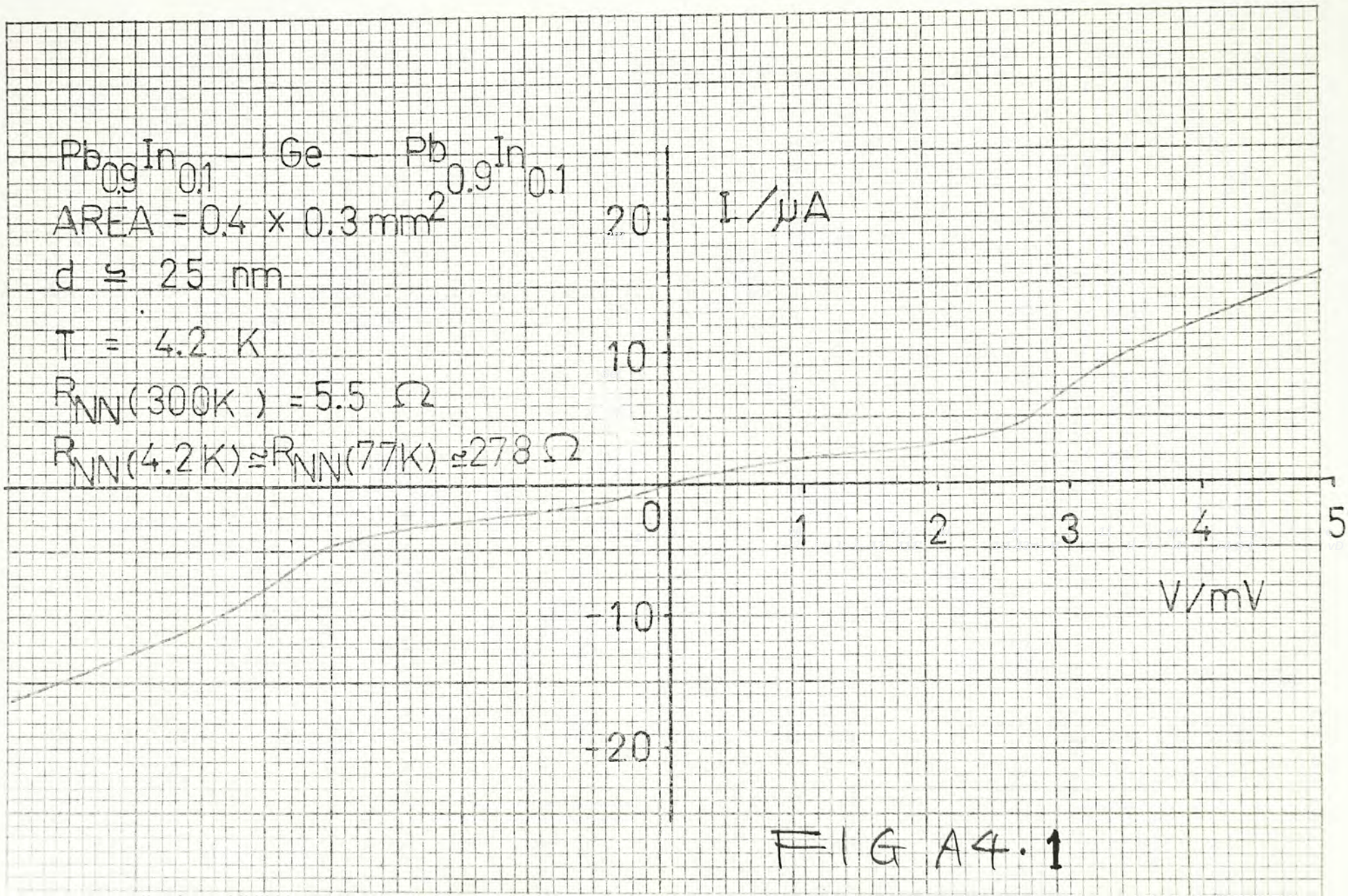
$Pb_{0.9}In_{0.1}$ — Ge — $Pb_{0.9}In_{0.1}$
AREA = 0.4 × 0.3 mm²
d ≒ 25 nm
T = 4.2 K
R_{NN}(300K) = 5.5 Ω
R_{NN}(4.2K) ≃ R_{NN}(77K) ≃ 278 Ω
I/μA
20
10
0
-10
-20
1
2
3
4
5
V/mV

FIG A4.1

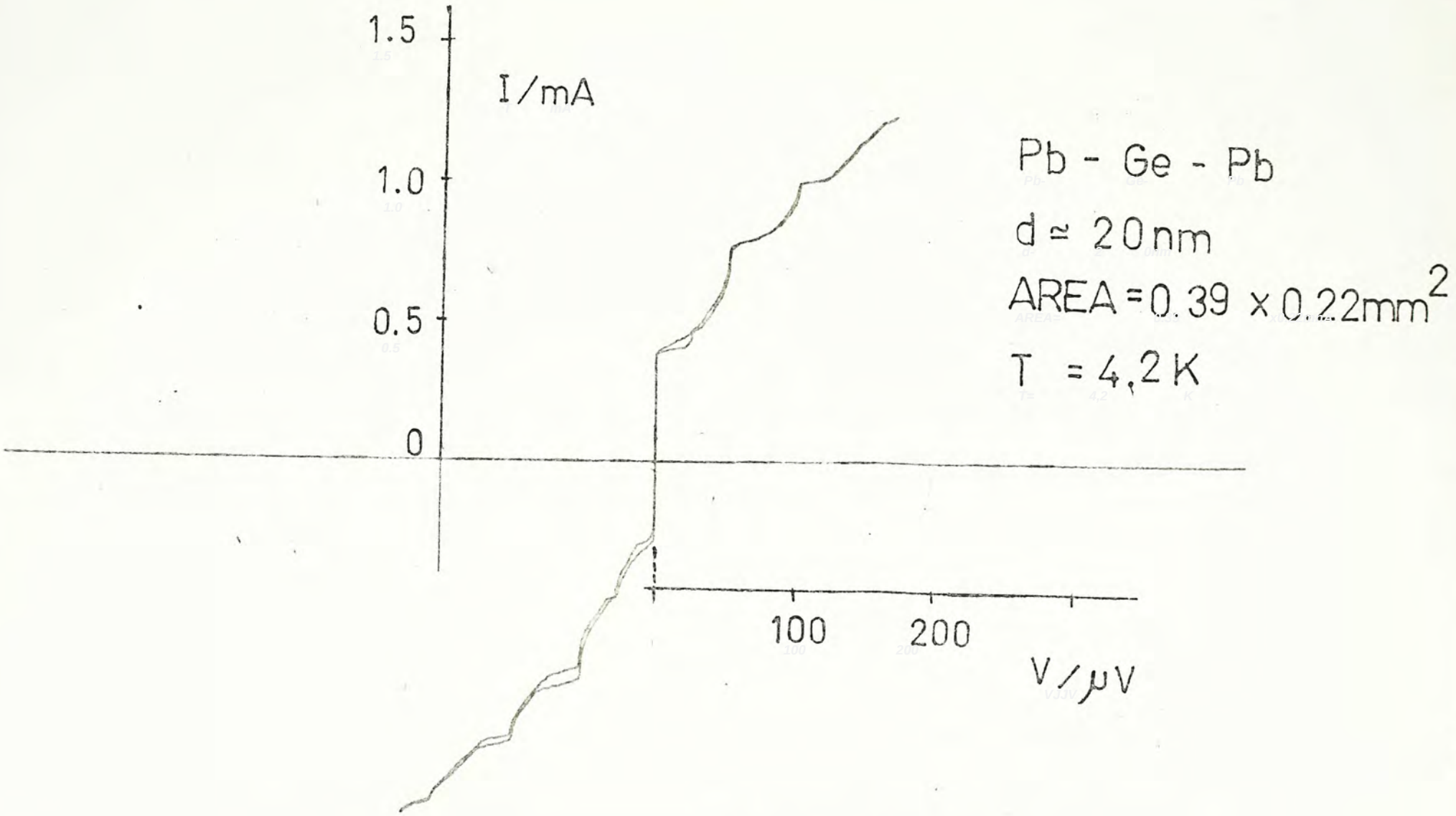

FIG A4.2a

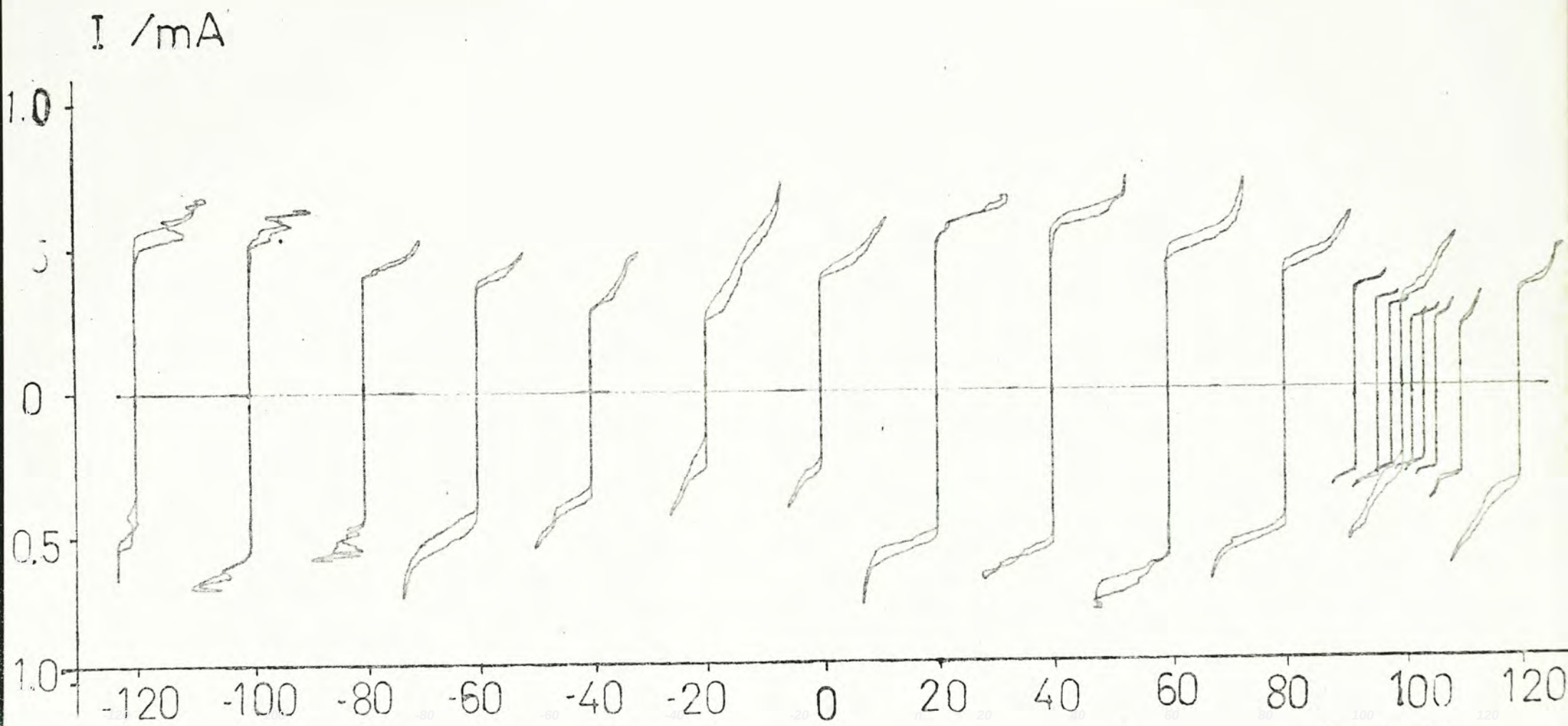

FIG A4 · 2b

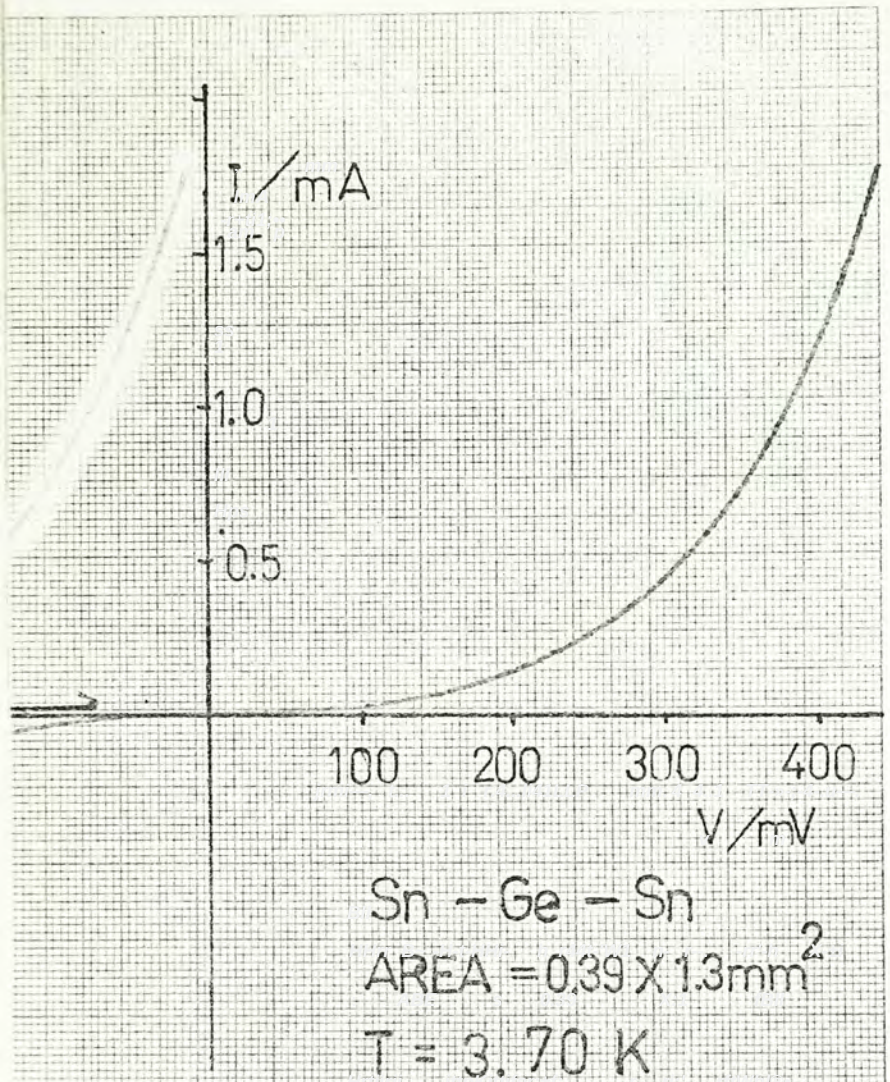

FIG A4. 3a

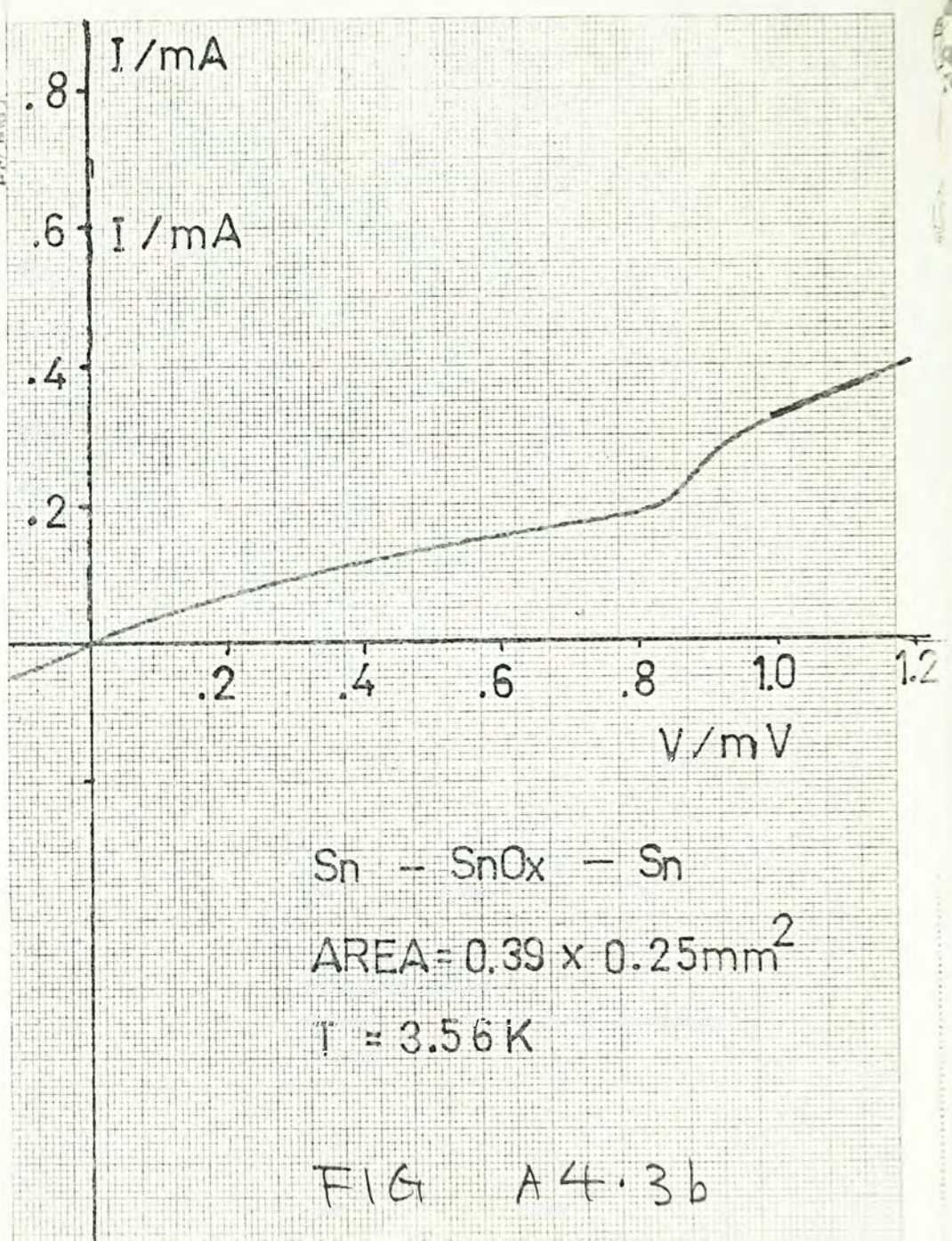

FIG A4.3b

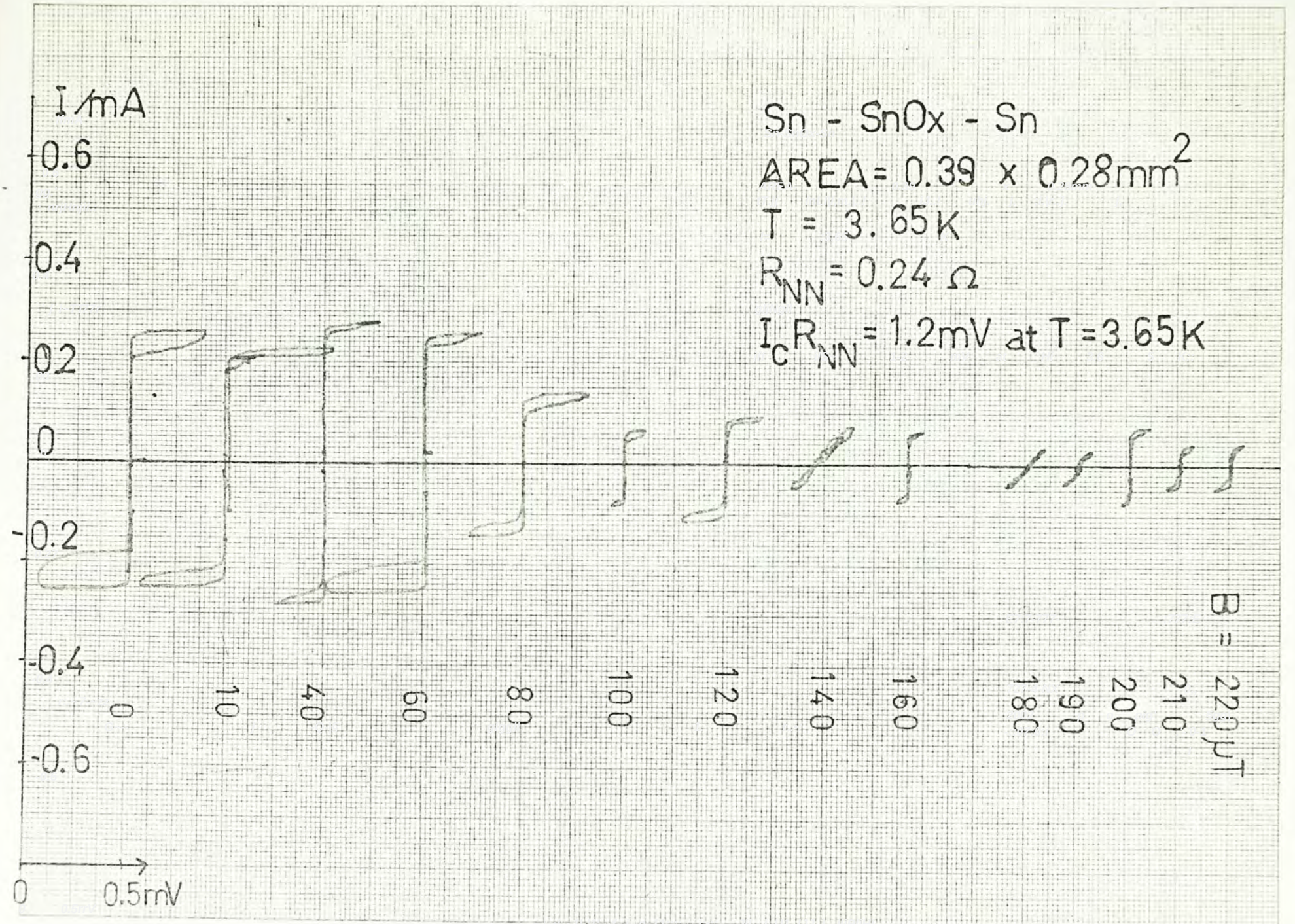
I/mA
0.6
0.4
0.2
0
-0.2
-0.4
-0.6
Sn - SnOx - Sn
AREA = 0.39 x 0.28mm²
T = 3.65K
R_NN = 0.24 Ω
I_C R_NN = 1.2mV at T = 3.65K
B = 220 μT
0
10
40
60
80
100
120
140
160
180
190
200
210
0
0.5mV

FIG A4 · 3c

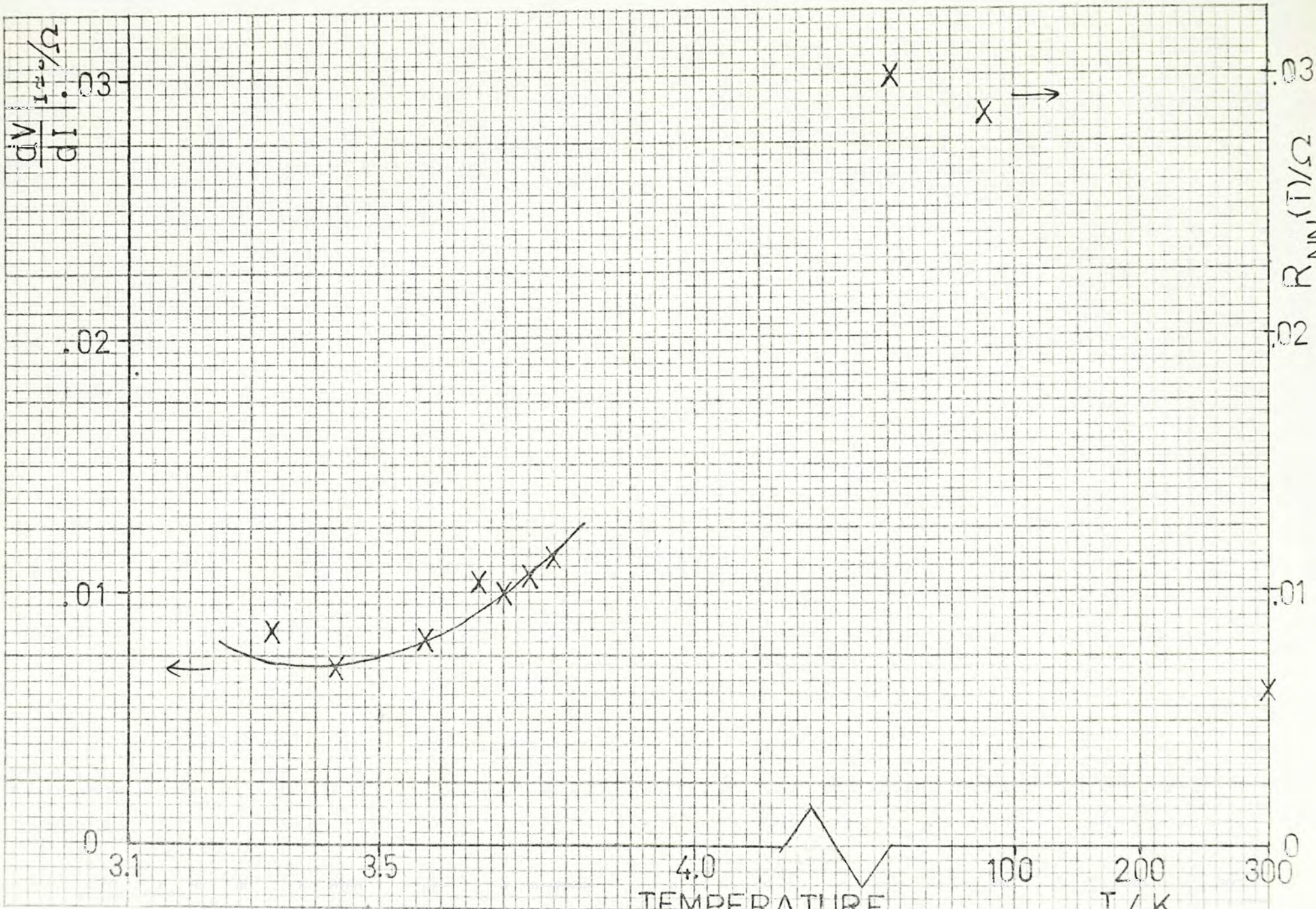
dV/dI / Ω
.03
.02
.01
0
3.1
3.5
4.0
100
200
300
T / K
TEMPERATURE
R_NN(T)/Ω
.03
.02
.01
0

FIG A4.4a

FIG A4.4b

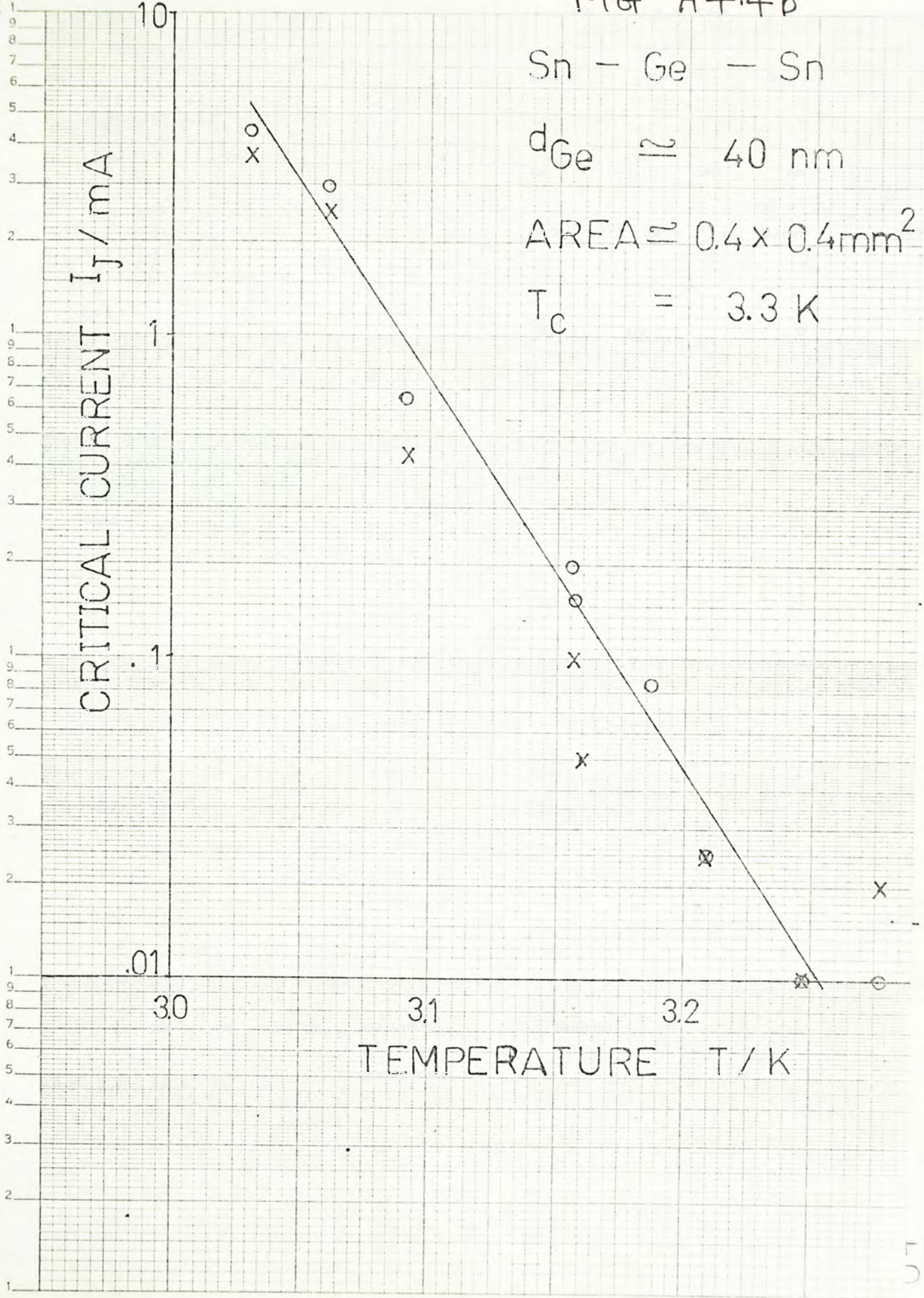
Sn – Ge – Sn
$d_{Ge} \simeq 40$ nm
AREA $\simeq 0.4 \times 0.4 mm^2$
$T_c = 3.3$ K
CRITICAL CURRENT I_J / mA
10
1
.1
.01
3.0
3.1
3.2
TEMPERATURE T / K

FIG A4.5a

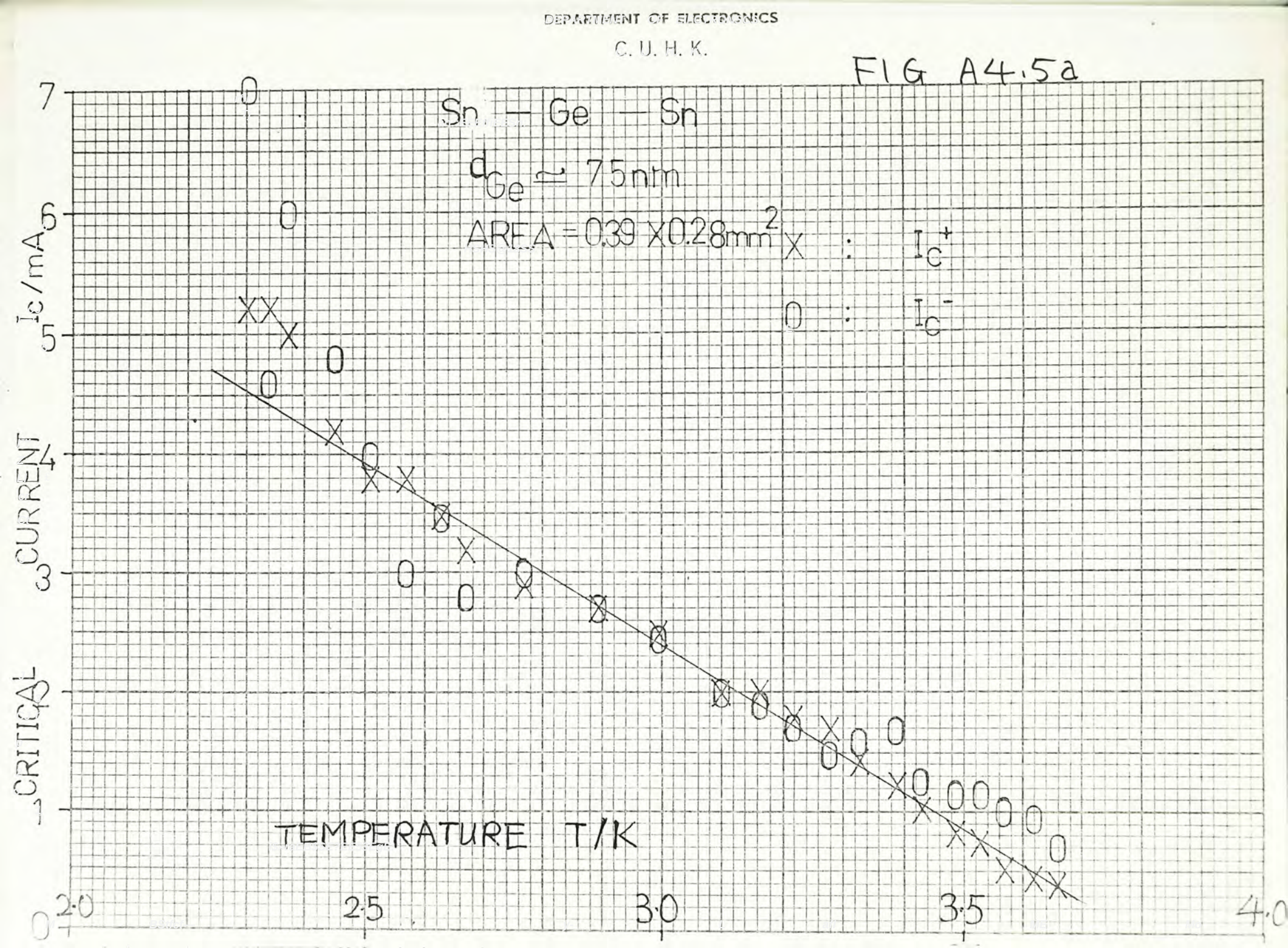
Sn — Ge — Sn
$d_{Ge} \simeq 75nm$
AREA = 0.39 X 0.28 mm^2
X : I_C^+
O : I_C^-
CRITICAL CURRENT I_C/mA
TEMPERATURE T/K
0
1
2
3
4
5
6
7
2.0
2.5
3.0
3.5
4.0

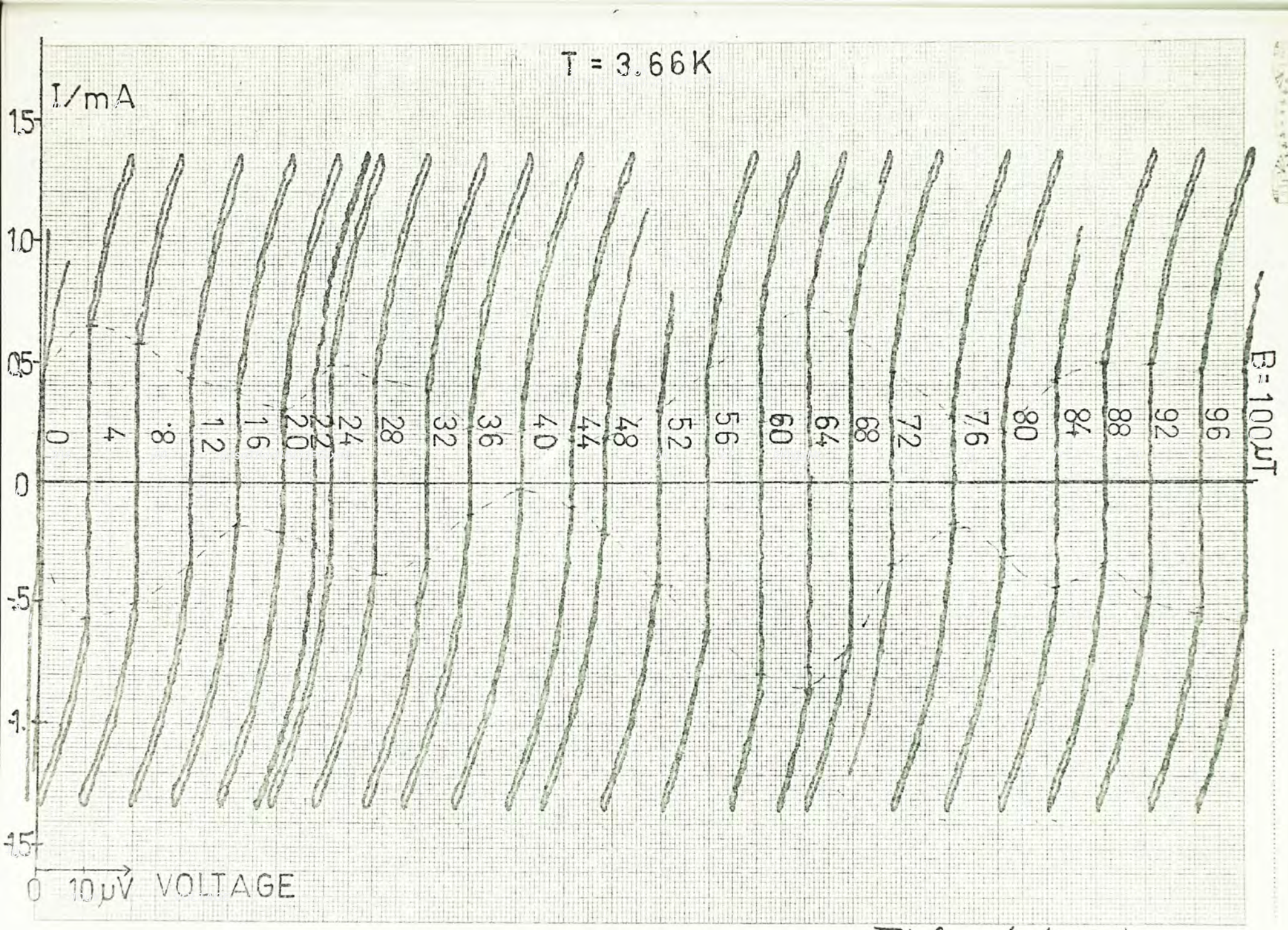
T = 3.66K
I/mA
15
10
5
0
-5
-10
-15
0
4
8
12
16
20
22
24
28
32
36
40
44
48
52
56
60
64
68
72
76
80
84
88
92
96
B = 100μT
0 10μV VOLTAGE

FIG A 4.5b

FIG A4.6b

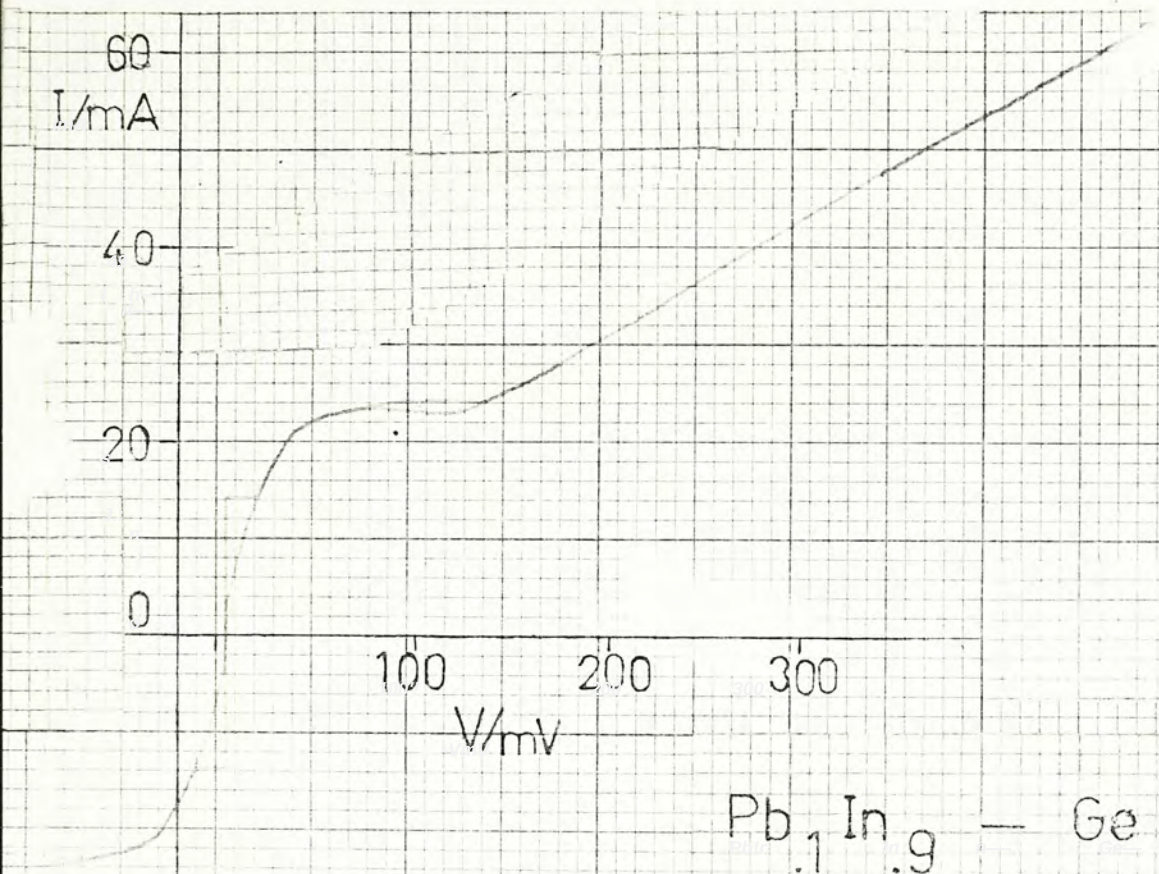

FIG A4.6a

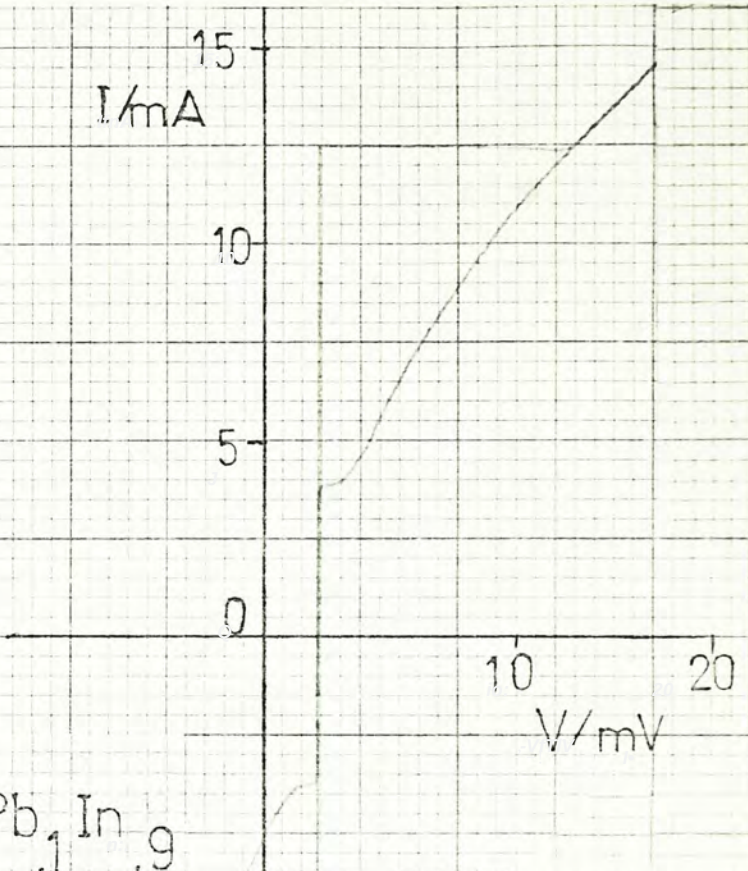

$Pb_{.1}In_{.9}$ — Ge — $Pb_{.1}In_{.9}$

AREA $= 0.5 \times 0.5\,mm^2$

T = 3.39 K

FIG. A4.6c

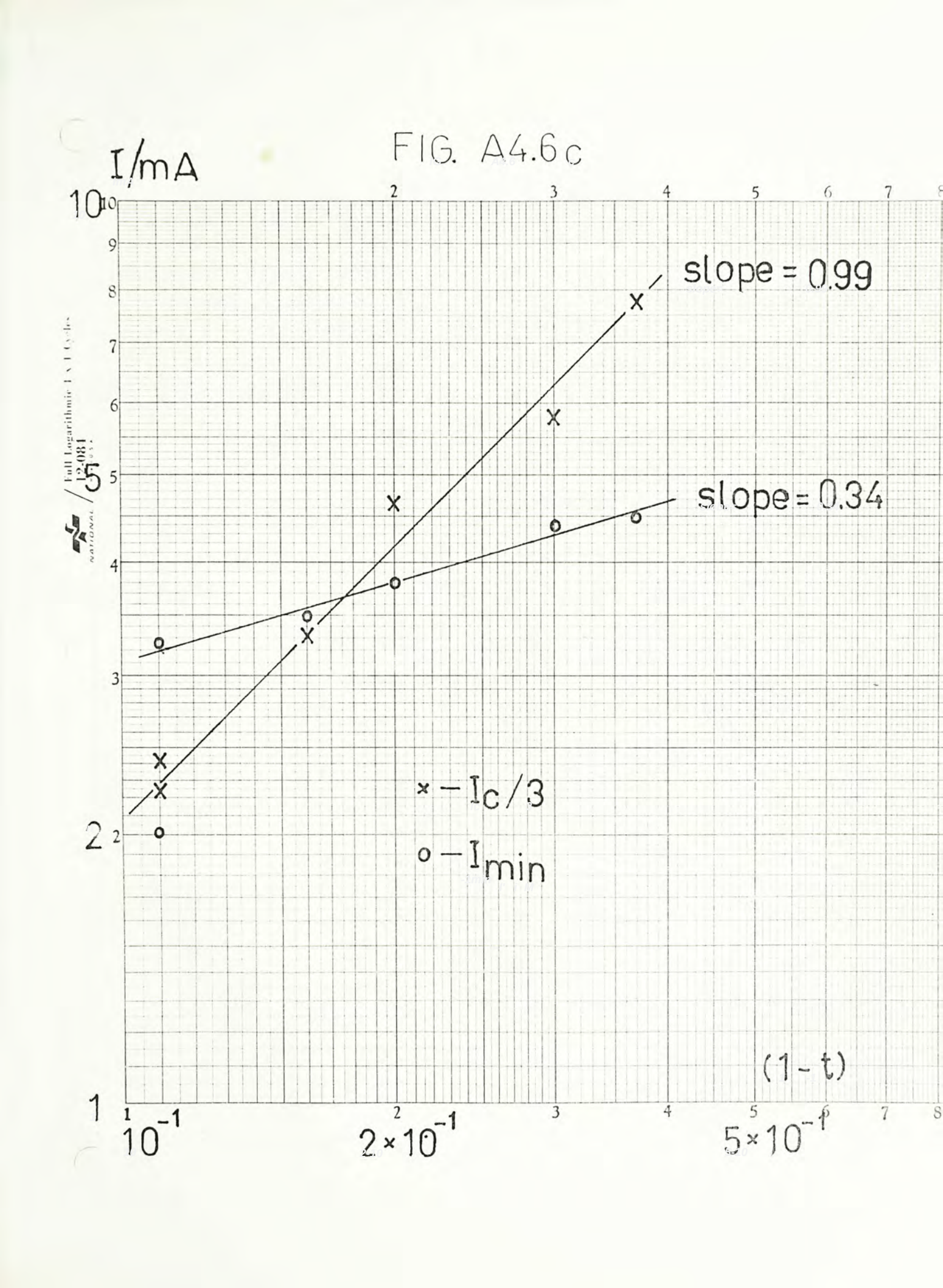

FIG. A4.7

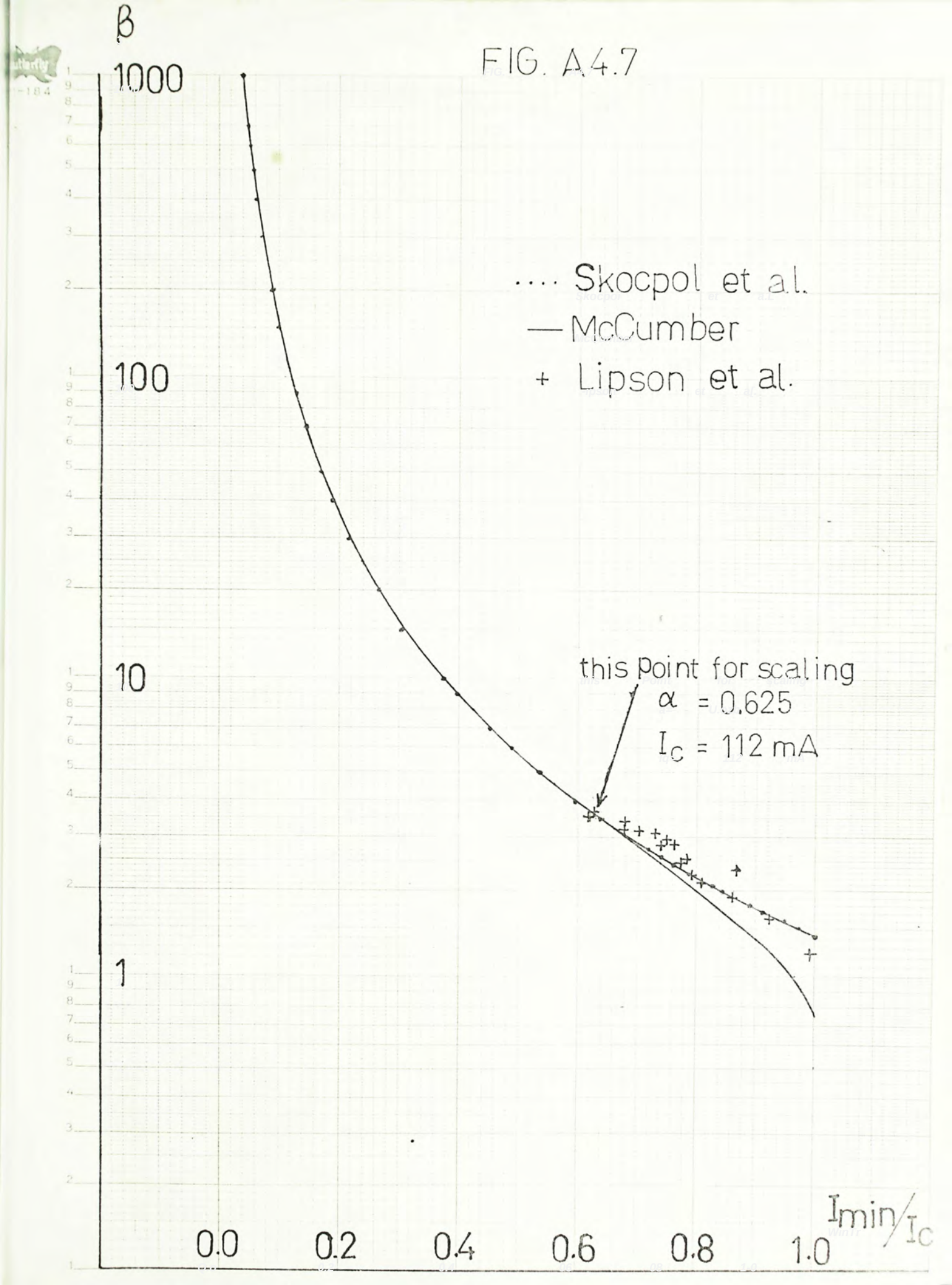
β
1000
100
10
1
0.0
0.2
0.4
0.6
0.8
1.0
Imin/Ic
···· Skocpol et al.
— McCumber
+ Lipson et al.
this point for scaling
α = 0.625
Ic = 112 mA